

ABSTRACT

MA, XIAOLONG. Microstructures and Mechanical Properties of Cu and Cu-Zn Alloys.
(Under the direction of Professor Yuntian Zhu and Professor Jagdish Narayan)

Strength and ductility are two crucial mechanical properties of structural materials, which, unfortunately, are often mutually exclusive based on the conventional design of microstructures and their deformation physics. This is also true in most nanostructured (NS) metals and alloys although they exhibit record-high strength. However, the disappointingly inadequate ductility becomes the major roadblock to their practical utilities due to the threat of catastrophic failure in load-bearing applications. Therefore, simultaneous improvement of strength and ductility or a well-defined trade-off between these two properties, i.e. increasing either of them without significant loss of the other, in NS materials has garnered extensive efforts from the research community. A few strategies have been explored to handle this long-standing challenge with promise. In this dissertation work, two of those strategies, deformation twins and laminate/gradient structures are specified with particular interests in NS Cu and Cu-Zn alloys. The author believes the observation and the revealed underlying mechanism are fundamental and therefore shed lights on their universal application to other metallic material systems.

Deformation twins have been frequently observed in ultra-fined grained (UFG) and NS face-centered cubic (FCC) metals and alloys, which is closely related to the better strengthening and strain hardening in mechanical performance. Previous findings even show that there exist an optimum grain size range within nano scale, where the deformation twins are of most frequency, i.e. most stable in pure FCC metals. However, such grain-size dependent twinning phenomenon is still unclear in FCC alloys. We report, for the first time in systematic experiments, the observed optimum grain sizes for deformation twins in NS

Cu–Zn alloys slightly increase with increasing Zn content. Our results indicate that alloying changes the relationship between the stacking-fault and twin-fault energy and therefore affects the optimum grain size for deformation twinning. Another interesting finding in contrast to the conventional thoughts is the macroscopic strain status of the deformation twins. These two issues are of both scientific and practical importance in microstructure design and fabrication in NS alloys.

Laminate/gradient is another recently developed strategy, which may hold the promise to improve mechanical properties of metallic materials. We produced a laminate structure with a NS Cu-10Zn layer sandwiched between two coarse-grained (CG) Cu layers, where the collective tensile ductility and strain hardening are observed higher than prediction by the rule-of-mixture. The primary results from this sandwich also inspired the next idea of multi-layered NS Cu-10Zn and CG Cu, which is anticipated to have superior strength and ductility since it has more heterogeneous interfaces. Simultaneous improvement of strength and ductility in samples with decreasing interface spacing is found in these laminates. More importantly, it's also observed that each interface generates extra geometrically necessary dislocations in the vicinity of itself with a most affected zone spanning a few micrometers. This is not affected by the interface spacing and implies an optimum laminate design for best back stress hardening capacity and ductility. Our results shed lights into the architectural design and fundamental deformation studies of materials with laminate/gradient structures.

© Copyright 2016 by Xiaolong Ma

All Rights Reserved

Microstructures and Mechanical Properties of Cu and Cu-Zn Alloys

by
Xiaolong Ma

A dissertation submitted to the Graduate Faculty of
North Carolina State University
in partial fulfillment of the
requirements for the degree of
Doctor of Philosophy

Materials Science and Engineering

Raleigh, North Carolina
2016

APPROVED BY:

Dr. Yuntian Zhu

Co-Chair of the Advisory Committee

Dr. Jagdish Narayan

Co-Chair of the Advisory Committee

Dr. Carl C. Koch

Dr. Ronald O. Scattergood

Dr. Suveen N. Mathaudhu

DEDICATION

To my beloved parents Jielin & Meilan

I appreciate to have you in my lif

BIOGRAPHY

Xiaolong Ma was born on May 19th, 1988 to Mr. Jieli Ma and Mrs. Meilan Yao in Nantong, a charming coastal city in China. Inspired by his primary and middle school teachers, Xiaolong was gradually absorbed into studying science and discovering the unknown in nature. In Aug. 2007, He was enrolled into Zhejiang University, a beautiful and high-ranking university in Hangzhou, China. During the undergraduate period, Xiaolong enjoyed the immense knowledge and the profound friendship, which would be both lifelong. Eventually in Jun. 2011, he achieved the Chu Kochen honors bachelor degree, majoring in Materials Science and Engineering. Later on, Xiaolong continued his journey in materials science at North Carolina State University. Under the direction of Professor Yuntian Zhu, he was dedicated to investigating the advanced microstructures in metallic materials and their relationship with mechanical properties. He received his Ph.D degree in Materials Science and Engineering in March 2016. On the route to his Ph.D, Xiaolong also pursued a master degree in Statistics, which broadened his perspectives of understanding science and the world.

ACKNOWLEDGMENTS

First, I would like to express my deepest gratitude to my advisor Professor Yuntian Zhu and Professor Jagdish Narayan for their patient guidance and continuous encourage whenever I met with difficulties or setbacks during the journey to my Ph.D. Their undiminished passion for science and meticulous scholarship set an example to me of doing good research during past five year and will, definitely, benefit me for the whole life. Many thanks go to Professor Suveen Mathaudhu for his insightful ideas, enlightening discussions and friendly encouragements throughout my graduate study. I'm also grateful to Professor Ronald O. Scattergood and Professor Carl C. Koch for their serving on my committee as well as their tremendous facilitation of instrument use and constructive comments on my work all along the way.

I wish to appreciate Dr. Weiwei Jian and Dr. Weizong Xu for their patient guidance and unending help in sample preparation, electron microscopy and image analysis during my research. I'm also grateful to Professor Chongxiang Huang for his kind supervision, informative discussions and delightful collaboration during his one-year visit to Raleigh. I'd like to thank Dr. Heinz Werner Höppel and his group members in Germany for their kind collaboration in fabricating laminate samples for our researches.

I'd like also express my thanks to Professor Douglas Irving and Professor Thom LaBean. Working as a teaching assistant with them during my first year was a treasurable experience for me. Teaching and learning could promote each other and I did learn much from that teaching process.

I also would like to acknowledge the use of the Analytical Instrumental Facility (AIF) in North Carolina State University. Many thanks should be delivered to Dale Bachelor, Roberto Garcia, Dr. Yi Liu, Dr. Yang Liu and Dr. Xiahan Sang for offering the strongest maintenance service and excellent training programs, which made numerous research projects, including mine, possible and full of technical support. A special thank-you goes to Roger Russell, Joe Matthews and Toby Tune for their generous assistance in all needs now and then. I also appreciate Edna Deas for her enduring assistance whenever needed.

I wish to thank all the members of my research group who made my life in Raleigh more enjoyable: Dr. Guangming Cheng, Dr. Xin Wang, Dr. Orm Piyawit, Dr. Fan Wu, Dr. Hao Zhou, Professor Xinkun Zhu, Dr. Dan Song, Jordan Moering, Liwen Zhang, Haotian Deng, Hao Yuan, Xiaotian Fang, Duo Xu, Silu Liu, George Crego, David Ho, Yingying Yu. I wish to thank all my friends inside and outside campus for bringing me so rich memories during my graduate life.

Last but not least, I dedicate this thesis to my beloved parents: Mr. Jielin Ma and Mrs. Meilan Yao, for their unconditional understanding, long-lasting support and forever love.

TABLE OF CONTENTS

LIST OF TABLES	IX
LIST OF FIGURES	X
CHAPTER 1	1
CHAPTER 2	5
2.1 Bulk Nanostructured Materials	5
2.1.1 Mechanical properties of nanostructured materials	7
2.1.2 Deformation mechanism of nanostructured materials	10
2.1.3 New strategies for better tensile ductility of nanostructured materials.....	18
2.2. Deformation twinning in nanostructured materials	22
2.2.1 Basics of deformation twinning in FCC materials.....	22
2.2.2 Grain size effect on twinning and mechanisms	25
2.2.3 Macroscopic strain of deformation twins and mechanisms in FCC materials.....	38
2.3 Laminate/gradient structures	45
2.3.1 Fabrication of laminate/gradient structures	46
2.3.2 Mechanical properties of laminate/gradient structures	52
2.3.3 Current perspectives of deformation mechanisms in laminate/gradient structures ...	56
CHAPTER 3	60
3.1 Sample Preparation	60
3.1.1 Nanocrystalline Cu-Zn alloys	60
3.1.2 Nanostructured Cu-10Zn sandwiched by coarse-grained Cu	61
3.1.3 Multilayered Cu/Cu10Zn laminates.....	62
3.2 Mechanical Tests.....	63
3.2.1 Uniaxial tension tests	63
3.2.2 Micro-hardness tests	63
3.3 Transmission Electron Microscopy (TEM)	64
3.3.1 TEM foil preparation	64
3.3.2 TEM observation	67
3.4 Electron Back-Scattering Diffraction (EBSD) Microscopy	67

3.4.1 EBSD sample preparation.....	67
3.4.2 EBSD observation.....	69
CHAPTER 4.....	70
4.1 Introduction.....	70
4.2 Experimental Method.....	72
4.3 Results and Discussions.....	73
4.4 Chapter Conclusion.....	82
CHAPTER 5.....	83
5.1 Introduction.....	83
5.2 Experimental Method.....	85
5.3 Results and Discussions.....	85
5.4 Chapter Conclusion.....	93
CHAPTER 6.....	94
6.1 Introduction.....	94
6.2 Experimental Methods.....	96
6.3 Results and Discussions.....	97
6.4 Chapter Conclusion.....	105
CHAPTER 7.....	106
7.1 Introduction.....	107
7.2 Experimental Methods.....	110
7.3 Results.....	112
7.3.1 Overview of microstructures.....	112
7.3.2 Heterogeneity across interfaces.....	113
7.3.3 Uniaxial tensile tests.....	117
7.3.4 Semi in-situ EBSD mapping and GND characterization.....	118
7.4 Discussions.....	123
7.4.1 Dislocation pile-up model for the GND density close to interfaces.....	123
7.4.2 Role of interface in deformation of nearby bronze grains.....	125
7.4.3 Back stress strengthening via heterogeneous interfaces.....	128

7.4.4 Interface spacing vs. mechanical performance	129
7.5 Chapter Conclusion	131
CHAPTER 8	133
REFERENCES	136
APPENDICES	163
A1. Matlab codes to determine uniform elongation	163
A2. Matlab codes to determine local misorientation	163

LIST OF TABLES

Table 2.1 The Hall-Petch slopes for fcc, bcc and hcp metals and alloys	27
Table 2.2 The critical stress and optimum grain size for the formation of deformation twinning in some nanocrystalline fcc metals	35
Table 2.3 Comparison of conditions of air blast shot peening and ultrasonic shot peening..	50
Table 3.1 Composition standards for the selected commercial Cu and Cu-Zn alloys	60
Table 4.1 Parameters and results in calculations of the model.....	76
Table 5.1 Experimental applied shear stress, stacking-fault energy, observed average twin thickness in NC Cu-Zn alloys	92
Table 7.1 Chemical compositions and general material properties of raw materials	110

LIST OF FIGURES

- Figure 2.1** (a) a schematic illustration of two-dimensional NS material. The atoms in the centers of the “crystals” are indicated in black while the atoms at boundary regions are represented by open circles. (b) A real high-resolution TEM micrograph shows atomic planes of NS platinum. An array of dislocations at boundaries is marked with red ‘T’. 6
- Figure 2.2** Summarized yield stress of NS Cu combined with the conventional Hall-Petch plot 8
- Figure 2.3** Summarized ductility for NS materials: (a) for two-step processing methods (like inert gas condensation and mechanical milling); (b) for one-step processing (like electro-deposition, severe plastic deformation and in-situ mechanical milling)... 9
- Figure 2.4** (a) Schematic illustration of a pile-up formed in grain 1 under external shear stress τ , which promote the activation of dislocation source S_2 in grain 2. Dashed line represents the preferred slip plane in each grain. (b) TEM bright field image of a pure Al sample after high-pressure torsion deformation under 1 GPa for 1 revolution..... 11
- Figure 2.5** Continuous bright-field TEM observations of deformation processes in nanocrystalline Ni₃Al during in-situ tensile test. Arrows in (d) mark the apparent grain boundary sliding features during tension.. 13
- Figure 2.6** A snapshot of nanocrystalline Al at 11.9% plastic strain, showing vast dislocation activity generated from grain boundaries. 15
- Figure 2.7** Grain boundary dislocations facilitate the grain rotation during tension. Red “T” represents the grain boundary dislocations and red number marks grain orientation difference. 16
- Figure 2.8** Schematic sequence of the deformation evolution of nanocrystalline Pd under shear stress of 0.6GPa, showing the relative grain rotation followed by mutual coalescence..... 17
- Figure 2.9** (a) Engineering stress-strain curves for pure Cu Curve A, annealed, CG Cu; B, room temperature rolling to 95% cold work; C, liquid-nitrogen temperature rolling to 93% cold work; D, 93% cold work+180oC, 3 min.; and E, 93% cold work+200oC, 3 min. Note the best performance of strength and uniform plastic strain to failure in Curve E. (b) Typical bimodal grain size microstructure in Curve E of (a). (c) Tensile engineering stress-strain curves of the CG, NS and NS+Precipitation samples of 7075 Al alloy. Open circles and squares mark the 0.2% yield strength and the uniform elongation, respectively. (d) HRTEM image

along a $\langle 011 \rangle$ matrix zone axis of a NS+Precipitation sample showing spherical G-P zones, plate-shaped η' phase and equiaxed η phase. 20

- Figure 2.10** (a) Tensile stress-strain curve for an electrodeposited Cu sample with nanotwins in comparison with that for a CG and a nanocrystalline Cu. (b) HRTEM of the nano-twin structures, showing partial dislocation disassociation, dislocation pile-up and at twin boundaries. 21
- Figure 2.11** (a) Conventional deformation twinning by the gliding of partials on successive slip planes above the twin boundary changes the shape of the spherical grain above the twin boundary. (b) Three equivalent Burgers vectors b_1 , b_2 and b_3 on the (111) slip plane for Shockley partials..... 23
- Figure 2.12** The process of forming a three-layer deformation twin by the slip of three partials with (Route A) the same Burgers vector on successive slip planes and (Route B) the slip of three partials with a mixture Burgers vector on successive slip planes. Two sides are schematic illustration of the final twin morphology caused by each route..... 23
- Figure 2.13** Schematic description of grain size on the critical stress needed to activate deformation twinning. The grain size effect for nanocrystalline bcc and hcp metals is uncertain. The schematic of Hall-Petch relationship for twinning and full dislocation slip in CG metals and alloys, σ is the stress and d is the grain size..... 26
- Figure 2.14** Statistical grain size effect on the formations of stacking faults and deformation twins in nanocrystalline Ni deformed under tension at liquid nitrogen temperature. (a) The size distribution of all grains examined under HRTEM. (b) The fraction distribution of grains containing stacking faults and twins. 30
- Figure 2.15** The size distribution of all grains (light yellow bars) and grains that contain twins (dark blue bars) with increasing HPT turns in a nanocrystalline Ni–20wt.% Fe alloy. The statistical data are measured using HRTEM, with sample in a location close to the edge of each HPT disk. 32
- Figure 2.16** A schematic illustration of a dislocation model for the nucleation of a deformation twin via the emission of a twinning partial on a (111) plane adjacent to the stacking fault plane..... 35
- Figure 2.17** Schematic illustration of the grain size effect on the twinning and detwinning tendency..... 38
- Figure 2.18** (a) HRTEM micrographs of twins in nanocrystalline Cu synthesized by high-pressure torsion. The arrow indicates the twin boundary. (a) A grain boundary has a 141° kink at its intersection with the twin boundary. (b) A zero-strain

- deformation twin with smooth intersection with the grain boundary (indicated by the broken curve)..... 39
- Figure 2.19** A Shockley partial dislocation loop with Burgers vector b_1 emitted from a grain boundary triple junction at E, grows, and deposits on other grain boundaries of a hexagonal grain. Part of the dislocation line segments parallel to grain edges AB and DE has pure screw character and can move along the grain boundary to the next slip plane..... 41
- Figure 2.20** (a) HRTEM micrograph of a $\Sigma 3\{112\}$ ITB showing periodic contrast on every three (111) atomic planes. (b-d) Schematic description of CSTP operation, “move-drag” propagation, to generate a zero-strain deformation twin: (b) the initial stable structure of $\Sigma 3\{112\}$ ITB, (c) part of triple partial(s) move ahead under external stress, (d) the rest partial(s) catch up and reach the stress balance again. 44
- Figure 2.21** (a) Schematically representation of a typical accumulative roll bonding (ARB) process. (b) A series of Cu-Nb laminate composites with controllable layer thickness produced by the method in (a)..... 48
- Figure 2.22** Schematic illustration of the surface mechanical grinding treatment set-up and the plastic deformation layer induced by the tool tip. 51
- Figure 2.23** (a) Relationship between strength and ductility in (a) Al/Cu samples and (b) Al/Al-12%Si samples: showing two different ductility trends versus number of ARB cycles..... 53
- Figure 2.24** Tensile curves of gradient structures of pure (a) Cu and (b) interstitial free steel. Both contain a NS surface 55
- Figure 2.25** Conceptually illustration the strength/ductility relationship in traditional homogeneous microstructure and gradient structure: the strength of a metal is increase at an expense of ductility and follows a typical inward “banana-shaped” curve (blue). However, strength-ductility synergy is achieved with gradient nanograined (referred as GNG) structures (red)..... 55
- Figure 2.26** (a) A bright-field TEM image showing the grain size distribution of topmost surface of the gradient Cu. (b) The grain size distribution of the topmost layer of the sample after tensile deformation with true strain of 33%. (c) Average grain size measurements in different sample locations with various deformation strains 57
- Figure 2.27** (a) Strain hardening rate ($\Theta=d\sigma/d\varepsilon$) vs. true strain curves for gradient interstitial free steel sample and its homogeneous counterparts. (b) Measured distribution of lateral strain (ε_x) and strain gradient ($d\varepsilon_x/dy$) across the thickness along one

- transverse line across the sample after tension. (c) TEM image showing the dislocation accumulation in a CG grain surrounded by finer grains at tensile strain of 2% of a lamella Ti sample..... 58
- Figure 3.1** (a) Overview of high-pressure torsion (constrained type) facility in lab. (b) The magnification of the central part to hold the sample. (c) Typical sample geometries before and after HPT processing 61
- Figure 3.2** (a) Overview of mini rolling machine in lab for sample processing. (b) Overview of vacuum tube furnace to perform necessary annealing. 62
- Figure 3.3** Overview of (a) Shimadzu AGS-20kNG uniaxial tension tester. (b) Sherline CNC mill system (8600) to machine the dog-bone shaped tensile specimen. (c) Micro-hardness tester with loading variation from 10g to 200g. 64
- Figure 3.4** Overview of (a) MultiPrep™ system from Allied High Tech. (b) Precision Ion Polishing System (PIPS) from Gatan Inc. 65
- Figure 3.5** Overview of a FEI Quanta 3D FEG dual-beam system for both FIB lift-out technique and EBSD observations 66
- Figure 3.6** Overview of (a) JEM-2010F transmission electron microscope and (b) aberration-corrected FEI Titan G2 microscope..... 68
- Figure 3.7** Overview of (a) house-built simple electrochemical polishing system (b) Fischione Ion Mill instrument (Model 1060) 69
- Figure 4.1** Bright-field TEM images of (a) Cu-10Zn, (b) Cu-15Zn and (c) Cu-30Zn show HPT-ed microstructures containing nano-size grains and deformation twins. Insets are corresponding selected area diffraction patterns. Statistical grain size distributions of (d) Cu-10Zn, (e) Cu-15Zn and (f) Cu-30Zn show considerable proportions of nano-grains for statistical analysis..... 74
- Figure 4.2** Typical twinning morphologies in deformed NC Cu-Zn alloys: (a) Deformation twins across the whole grain. (b) Deformation twin terminated in the grain interior. (c) Deformation twin highly interacted with other defects. Specific locations in corresponding nano-grains are shown in (d)-(f). Note all twins are bounded by GBs, as shown by asterisks..... 76
- Figure 4.3** Statistical analysis of randomly observed nano-grains and their twinning propensities. Grain-size distributions of all observed grains (blue bar) and those with twins (red bar) in (a) Cu-10Zn, (c) Cu-15Zn, (e) Cu-30Zn. Corresponding fractions of grains with twins in (b) Cu-10Zn, (d) Cu-15Zn, (f) Cu-30Zn, including total fraction (number at top right) and those of each size region (blue bar)..... 77

- Figure 4.4** Summary of experimental results and model predictions of optimum grain sizes (d_{op}) for deformation twinning in different nanocrystalline Cu-Zn alloys vs. their Zn compositions 80
- Figure 4.5** Model-based stress calculation (solid lines) of twinning partial (τ_{twin}) and trailing partial (τ_{trail}) and resulted optimum grain sizes (d_{op}) for deformation twinning in Cu-Zn alloys. Dash-dot curves schematically represent the modifications due to the inequality of $\gamma_{SF} \neq 2\gamma_{twin}$ in alloy systems and therefore modified optimum grain sizes d_{op} 81
- Figure 5.1** Typical high-resolution TEM images of deformation twins with macroscopic strains in NC (a) Cu-10Zn, (b) Cu-15Zn, (c) Cu-30Zn and zero-strain twins in (d) Cu-10Zn, (e) Cu-15Zn, (f) Cu-30Zn. Solid lines mark the matrix-twin relationships. The twin-GB interceptions are highlighted to indicate the macroscopic strain or the lack of it. 87
- Figure 5.2** (a) Fraction of zero-strain deformation twins in each Cu-Zn alloy. Red bars stands for fraction of zero-strain twins and blue bars stands for twins with macroscopic strain. (b) Fractions of zero-strain deformation twins and stacking-fault energy (blue) in Cu-Zn alloys. 88
- Figure 5.3** Typical atomic morphology of ITBs of zero-strain twins in the Cu-10Zn alloy: (a) with periodicity: $\Sigma 3\{112\}$ ITB, (b) without periodicity. Split of $\Sigma 3\{112\}$ ITBs under (a) near zero stress to (b, c) lower residual stress under equilibrium states in as-deformed nano-grains. Inset in (c) is FFT pattern for the extended ITB, confirming the existence of periodic structure by extra spots. 89
- Figure 5.4** (a-c) Schematic illustration of breakdown process of $\Sigma 3\{112\}$ ITB in nano-grain FCC materials with low SFE. (d) HRTEM observation of periodic structure at GB in the Cu-10Zn alloy. Inset is the low magnified GB image to show the macroscopic strain. (e) FFT result of the selected region in (d), showing the same pattern in Figure 5.3e. 93
- Figure 6.1** (a) Schematic illustration of major procedures to fabricate CG/NS/CG sandwich materials. Deformation history of thickness reduction is also provided below the corresponding step. (b) Optical microscopy observation of as-processed sandwiches with NS Cu-10Zn volume fraction 0.47. (c) Vickers Micro-hardness indentation (with loading 25g) on cross-sectional sample in (b). 98
- Figure 6.2** (a) ICCM of a typical NS/CG interface in sandwich (70 tilt of sample while imaging). (b) TEM observation of as-processed interface. (c) HAADF imaging of an enlarged area around Cu/Cu-10Zn interface by STEM. EDS mapping of (d) Cu and (e) Zn in corresponding regions in (c). 99

- Figure 6.3** (a) Uniaxial tensile engineering strain-stress curves for pure CG Cu and NS Cu-10Zn and sandwiches with various compositions. Inset shows the dimension of tensile test samples $0.6 \times 2 \times 8.4$ mm³. (b) Yield strength versus volume fraction of NS Cu-10Zn from tensile tests and prediction from ROM. (c) Strain hardening curves from corresponding tensile tests and calculation based on ROM. Inset is the magnified tensile curve at low strains where outperformance of strain hardening (yellow shadow) occurs compared to ROM. Black crossover stands for the necking strain level in pure Cu-10Zn. (d) Uniform elongation versus volume fraction of NS Cu-10Zn from tensile tests and prediction from ROM. 101
- Figure 6.4** (a) Overview of the sandwich piece after tensile fracture. (b) Typical morphology at lateral fracture interface in (a). (c) Schematic illustration of stress status of the laminates around the strain level where the middle NS layer tends to shrink while outer CG layers stabilize it. 105
- Figure 7.1** Optical microscopy of (a) N2, (b) N3 and (c) N5 samples, respectively. It clearly shows the inter-layer contrast and the interface spacing. ICCM observation of (d) N2, (e) N3 and (f) N5 samples, showing the microstructures at Cu/Bronze interfaces samples..... 113
- Figure 7.2** (a) TEM observation of Cu/Bronze interface of ARB N5 sample shows the void-free interface and the discrepant grain size across it. (b) Retained rolling microstructure in Cu10Zn layer. (c) Grain size distribution of the Cu layers based on the ICCM above. (d) Transverse grain size right to rolling direction in Cu10Zn layers based on the TEM results. 114
- Figure 7.3** (a) Micro-hardness measurement of both Cu and Cu10Zn layers in N2, N3, N5 samples after annealing. (b) {100}, {110}, {111} Pole figures in both Cu and Cu10Zn layer in N3 sample after annealing, showing the strong cube texture and a derivation of brass-type texture, respectively. Note that N2 and N5 have similar texture characteristics. 115
- Figure 7.4** (a) Tensile curves of N2, N3 and N5 samples show the simultaneous increase of strength and elongation with increasing number of layers. (b) Summary of tensile results. Error bars represents standard deviation from at least 3 data sets. 117
- Figure 7.5** Inverse pole figure mapping of regions around interfaces in (a-c) N2, (d-f) N3 and (g-i) N5 samples under different tension strain levels: 0%, 3% and maximum uniform Elongation. Left side of N2 and N3 samples are the Cu/Bronze interfaces and both sides in N5 sample are the Cu/Bronze interfaces..... 119
- Figure 7.6** GND density mapping based on local misorientation results in (a-c) N2, (d-f) N3 and (g-i) N5 samples under different tension strain levels: 0%, 3% and maximum

uniform Elongation. Left side of N2 and N3 samples are the Cu/Bronze interfaces and both sides in N5 sample are the Cu/Bronze interfaces..... 121

- Figure 7.7** Global GND density distribution on the corresponding mapping results in Figure 7.6. The mean value and standard deviation of GND density for the mapping are labeled in each histogram. 122
- Figure 7.8** Integrated GND density in Cu layer versus the equivalent distance from the interfaces at different strain levels of (a) N2 sample, (b) N3 sample, (c) N5 sample. Dash lines represent pile-up model fitting results..... 122
- Figure 7.9** Micro-hardness measurement of layer interior at uniformly elongated sample region after tension. Dash lines represent the base level before tension. 126
- Figure 7.10** (a) A TEM observation of Cu/Bronze interface in N5 sample after tension. (b) The high-resolution microscopy of the marked square in (a). Inset diffraction pattern shows the zone axis of Cu side is $\langle 110 \rangle$. The symmetric diffraction spots reveal the annealing twin in the Cu grain, which is also marked in the image. Another thinner deformation twin in Cu₁₀Zn side is highlighted as well. Nucleation site for the deformation twin is marked by arrow..... 127
- Figure 7.11** (a) Cyclic tensile curves of N2, N3, N5 samples. (b) The calculated back stress at corresponding strain levels. The dot lines are superposition of fitted hardening stage. (c) Derived backstress hardening between N3 & N2 samples and N5 & N3 samples, indicating a linear relationship close to mechanism prediction..... 130

Chapter 1

Thesis Introduction

Materials scientists have much in common with detectives: both want to figure out what's going on underneath the world they see. By collecting evidences and building up reasonable theories to fit facts, they attempt to make sense of what they observe and uncover the hidden truth. More than pure detectives, materials scientists would, in turn, take advantages of state-of-art knowledge to design and fabricate the desired microstructures that holds the promised properties. All this iterative process is well defined in the famous Thomas's tetrahedron, where processing, properties, theory and microstructure reside each corner and interrelated with others.

Applying the general principle to researches in nanostructured (NS) metallic materials, the community has spared tons of efforts to develop new microstructure candidates and investigate underlying deformation physics that render their better mechanical properties. One of the most challenging problems for massive structural applications of NS metals and alloys is to overcome their disappointingly low ductility. Up to date, a couple of strategies have been proposed to cope with this issue, including the design of bimodal grain-size microstructures, the advent of dispersed nanometric oxide particles, the introduction of nano-scale growth or deformation twins in lieu of dislocations and general high-angle grain boundaries and the recent development of laminate/gradient structures.

This dissertation focus interests on two of them: deformation twins and laminate/gradient structures. The background knowledge and hitherto relevant researches of

these two realms are detailed introduced in Chapter 2. The general role of twins in enhancing mechanical properties has been well studied thanks to extensive efforts during past decade. However, how to generate prosperous and stable deformation twins in NS materials is not clearly understood, especially in alloys. To be specific, how does alloying alter the so-called optimum grain size for twinning in nanometer scale and affect the macroscopic strain status of twinning microstructures? With respect to laminate/gradient structures, this is a relatively emerging topic in theoretical and experimental studies although their appearance in nature and manufacturing may date back to long time ago. Therefore, there're still a few fundamental issues remaining poor understood. For example, why and how does laminate/gradient structures influence deformation physics and thereby, the strength, ductility and strain hardening. Both of mentioned problems are important to the fundamental understanding and practical design of microstructures in NS alloys.

In this dissertation, Cu and Cu-Zn (no more than 30 wt.%) alloys are selected in all researches for their representativeness in face-centered cubic (FCC) metals and alloys. With well-developed fabrication techniques like high-pressure torsion and accumulative roll bonding, NS materials are readily produced in laboratories. In the analysis of materials defects, advanced characterization tools like transmission electron microscope, focused ion beam and electron backscattering diffraction serve as necessary and excellent assistants to visualize microstructures. The common experimentation details used in all studies here are given in Chapter 3.

Chapter 4 is dedicated to the studies of the alloying effect on grain-size-dependent deformation twinning in NS Cu-Zn alloys, where we use transmission electron microscopy

and statistical analysis to reveal the additional shift of optimum grain size for twinning in NS alloys. An early model based on pure metals is therefore reconsidered to match the effect in NS alloys.

In Chapter 5, we systematically investigate the macroscopic strain status of deformation twins in Cu-Zn alloys and found the relationship between zero-strain deformation twinning and the stacking-fault energies (SFE) by alloying. Underneath reason is further probed by high-resolution electron microscopy and discussed based on the early developed mechanisms for zero-strain twinning in NS materials.

Chapter 6 aims to introduce a successful method to fabricate NS Cu-10Zn layer sandwiched between two coarse-grained (CG) Cu layers by high-pressure torsion, rolling and annealing. Interlayer interface bonding and its heterogeneity are detailed characterized by electron microscopy. Mechanical tests also revealed the strength and ductility in this sandwich laminate design. The origin of resulted higher strain hardening is discussed based on dislocation dynamics.

Inspired by the primary results in the sandwich work, the multi-layered NS Cu-10Zn and CG Cu is systematically investigated in Chapter 7. Successful fabrication of laminates with similar microstructures but with various interface spacing paves the way for the following exploration of the heterogeneous interfaces' role in deformation and mechanical properties. Semi in-situ electron back-scattering diffraction mapping during tension reveals the dislocation dynamics in the vicinity in the interfaces and the layer interior. The effect of heterogeneous interfaces is discussed based on the strain gradient theory, dislocation pile-up model and back stress hardening process.

Finally, Chapter 8 summarizes this work and briefly makes the future remarks based on the current research results.

Chapter 2

Literature Review

2.1 Bulk Nanostructured Materials

Nanostructured (NS) materials are typically featured by their constituent or grain structures modulated on a length scale less than 100nm in at least one dimension [1–4]. Generally, the community classifies NS materials into three categories: i) nanometer-sized particles, thin wires or thin films; ii) solids that the nanometer-sized microstructures is limited to a thin surface region; iii) solids with nanometer-sized microstructures all over the bulk [1,5]. In this dissertation work, our interests fall into the third category here, which simply named as bulk NS materials. In the wake of the significantly refined grain size, NS materials consist of a high density (typically 10^{19} per cm^3) of grain (or interphase) boundaries, which is a sharp contrast to conventional thoughts. Figure 2.1a shows a two-dimension model of a NS material, where the open-circle atoms at boundaries take up an unusual high proportion of the total atoms [4]. Another real transmission electron microscopy (TEM) observation of NS platinum is present in Figure 2.1b, where red “T” marks the array of dislocations at boundary region [6]. Such microstructures have significant implications for their properties and will be addressed later.

Two complementary approaches have been developed to synthesize bulk NS materials [5]. First one is a “bottom-up” approach, where bulk NS materials are assembled from individual atoms or nanoscale building blocks like nanoparticles. Such methods include inert gas condensation [7], high-energy ball milling [8], spray conversion processing [9],

deposition [10], sol-gel process [11], etc. For structural applications, most bottom-up approaches require the consolidation of nanopowders, which is a challenge because the as-produced samples usually contain considerable voids, flaws and crack sources. The second approach for fabricating bulk NS materials is known as a “top-down” one, in which the existing coarse-grained materials are refined into NS materials, typically by severe plastic deformation [12–14]. The most successful “top-down” approaches developed so far are equal-channel angular pressing [15], high-pressure torsion [16], accumulative roll bonding [17], which have been extensively utilized in laboratory works and even commercially scaled up. The advantage of those “top-down” approaches is their strong capabilities to achieve NS materials with full of dense, free of porosity and contaminations, which paves the way to study their intrinsic mechanical properties and deformation mechanisms [5,18].

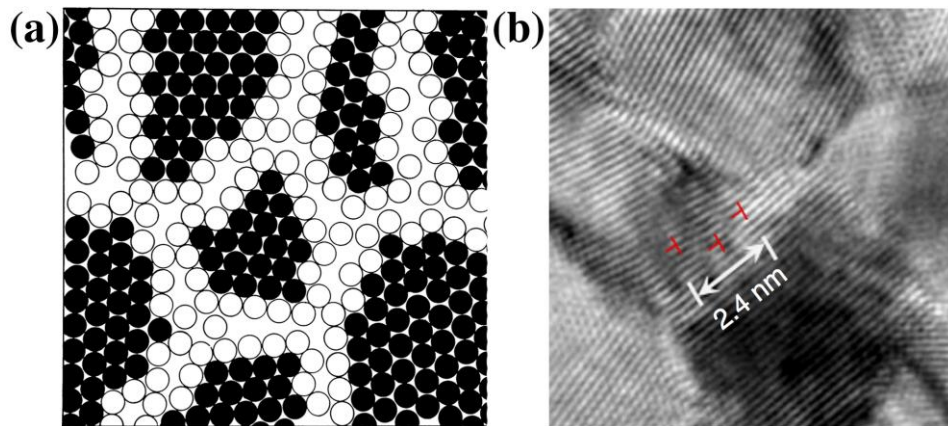


Figure 2.1 (a) a schematic illustration of two-dimensional NS material. The atoms in the centers of the “crystals” are indicated in black while the atoms at boundary regions are represented by open circles. (b) A real high-resolution TEM micrograph shows atomic planes of NS platinum. An array of dislocations at boundaries is marked with red ‘T’. [4,6]

2.1.1 Mechanical properties of nanostructured materials

Before proceeding to real experimental results, it's worth to keep in mind that processing approaches and sample dimensions also influence the observed mechanical properties [19,20]. The early bottom-up approaches often resulted in porosity and incomplete bonding among the grains, which is detrimental and probably masks the real mechanical properties of NS materials. The often-use sample dimension of tensile test for NS materials in lab is micro-size in order to avoid the imperfections [2]. Therefore, we mainly focus on the micro-sample results from the “top-down” methods in the following texts.

2.1.1.1 Strength

Reducing the characteristic size in NS materials has tremendous effect on their properties. This is broadly observed and summarized as size effect. Applying this to NS metallic materials, the refinement of grain size plays a critical role their mechanical properties. For example, the dependence of yield strength, hardness on grain size in metals has been well established in the conventional polycrystalline range (micrometer grains and upper sizes). Yield stress, σ_y , for materials with grain size d , follows the Hall-Petch relation [2,21,22]

$$\sigma_y = \sigma_0 + kd^{-1/2}$$

where σ_0 is the friction stress and k is the constant. For a more general case, the formula is to use a power expression with exponent $-n$, where $0.3 \leq n \leq 0.7$. Accordingly, a significant high yield stress and hardness is expected for the NS materials. A summarized result of yield strength vs. grains size from various sources on NS Cu is shown in Figure 2.2. There're two basic conclusions:

i). Clearly, NS Cu is much more stronger than their CG counterparts, which exhibits yield strength of only ~100 MPa.

ii). The conventional Hall-Petch relationship doesn't always hold true with decreasing grain size, especially when the grain size is less than 25nm ($d^{-1/2}=0.2 \text{ nm}^{-1/2}$). The deviation from Hall-Petch relationship is not exclusive to nanocrystalline Cu, but universal to most nanocrystalline metallic materials. It's worth to note that the deviation in hardness results is not so noticeable [22].

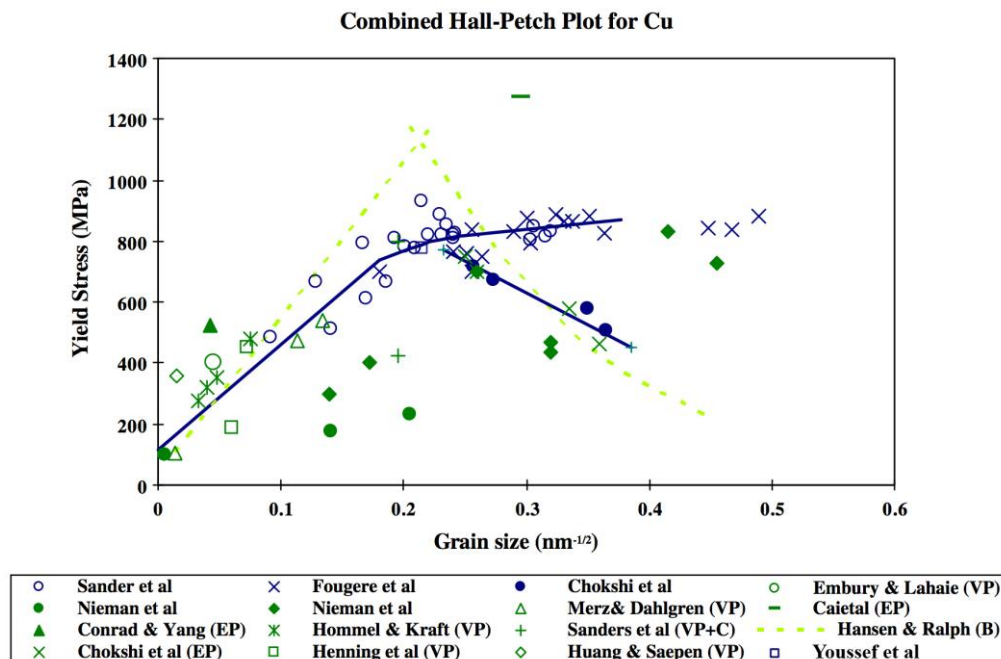


Figure 2.2 Summarized yield stress of NS Cu combined with the conventional Hall-Petch plot [2].

Some researchers have introduced an inverse Hall-Petch relationship (meaning the slope switches to negative) for NS materials with grain size less than 20 nm [23–25]. But this is still a controversial topic [2], which needs more information.

2.1.1.2 Ductility

In conventional understandings, refinement of grain size in the range of micrometer will lead an increase of ductility [2,26,27]. However, this is not promised in NS materials and unfortunately, their ductility at room temperature is often disappointingly low compared to their CG counterparts. For example, the NS Ni with nominal grain size of 28 nm exhibits very high yield strength more than 1 GPa, but with limited tensile elongation of 1% [28]. More generally, literature survey shows the vast majority of NS metals have tensile ductility below 5% [19,27] despite limited exceptions like the 23nm grained Cu with 15.5% tensile elongation in Youssef et al. [29], which poses a most challenge to the wide applications.

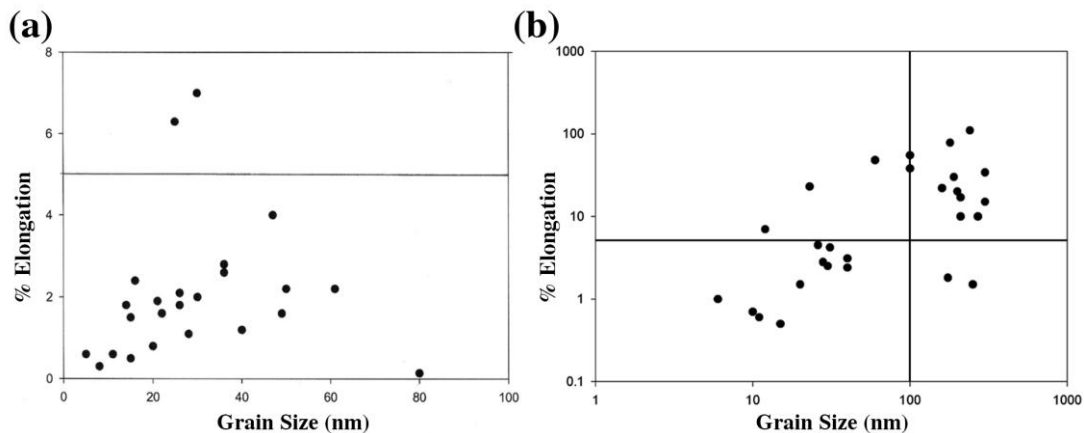


Figure 2.3 Summarized ductility for NS materials: (a) for two-step processing methods (like inert gas condensation and mechanical milling); (b) for one-step processing (like electro-deposition, severe plastic deformation and in-situ mechanical milling) [19]

Koch has identified the three primary reasons for the appearance of the disappointingly low ductility in NS materials [18,19]: i) residual artifacts from processing; ii) force instability in tension; iii) crack nucleation or propagation instability. After screening out most of the first reason by employing appropriate techniques like one-step processing, researchers still found that the very low ductility seems to be the intrinsic property of NS materials, as shown in Figure 2.3b. Another general principle of NS materials extrapolated from Figure 2.3 is that ductility decreases with reducing grain size in nanometer scale, which is a contrast to the previous belief in conventional grain size regime. Combined with the strength trend, there comes, without surprise, a popular and long-standing belief that strength and ductility is a paradox in NS materials [14,30,31]. The reason for this well-established notion is closely tied to the deformation physics in NS materials.

2.1.2 Deformation mechanism of nanostructured materials

2.1.2.1 Breakdown of dislocation pile-up

The deformation physics in NS materials could be fundamentally different from that for CG materials [2]. Conventionally, the Hall-Petch effect for the observed relationship between grain size and strength is reasonably explained by the dislocation pileup model, as schematically shown in Figure 2.4 [32,33]. Generated from the Franck-Read source assumed in the middle of the grain, dislocations with the same Burgers vector assemble at the grain boundary and effectively multiply the external stress field, which promote the dislocation motion in the neighbor grain under certain applied shear stress. However, with the significant refinement, effective dislocations accumulation is not favored within the grain, i.e. pile-up concept breaks down [34,35]. This has been widely observed, both experimentally and

computationally [36,37]. The deformed grains free of dislocations have been even found in ultrafine-grained Al, as shown in Figure 2.4b.

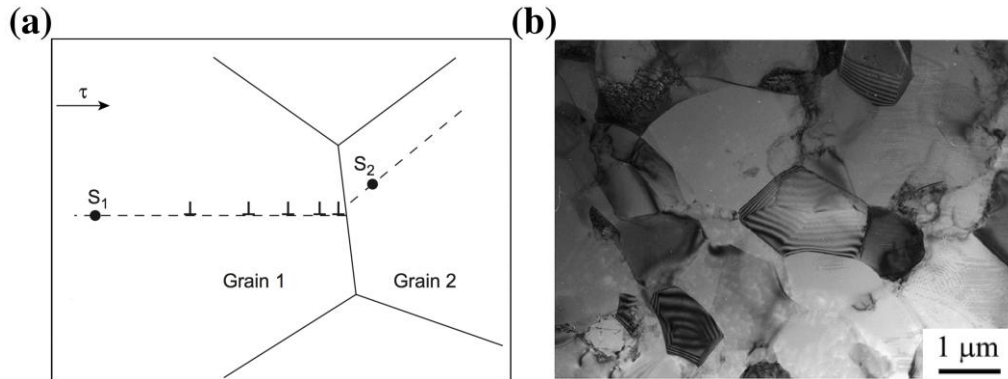


Figure 2.4 (a) Schematic illustration of a pile-up formed in grain 1 under external shear stress τ , which promote the activation of dislocation source S_2 in grain 2. Dashed line represents the preferred slip plane in each grain. (b) TEM bright field image of a pure Al sample after high-pressure torsion deformation under 1 GPa for 1 revolution. [32,38]

The absence of dislocation accumulation leads to two major consequences: first, the yield strength arises because the driving stress for all deformation would be largely carried by the external shear stress without effective multiplication. Second, strain-hardening capacity would be much poor in NS materials because hardening is typically attributed to the effective accumulation of dislocations. Hardening capacity is crucial to stable plasticity during tension, which highly related to the uniform elongation [39,40]. One should bear in mind that the breakdown of pile-up is more pronounced when grain size is extremely small, typically less than 10 nm. Other new mechanisms or minor mechanisms in CG grains become dominant and prevail the plastic deformation [41–43].

2.1.2.2 Grain boundary sliding

Grain boundary sliding was previously studied in the phenomenon of superplasticity. It accommodates shear strain by sliding one single or a group of grain with respect to the other. Later on, this deformation mechanism has been proposed to be quite operative in nanocrystalline grains by molecular dynamics simulations [44–49]. H. Hahn et.al [48] has established two hardness relationships based on the critical stresses to activate grain boundary sliding and dislocation motion/formation. It's proposed that below size of 50 nm, grain boundary sliding prevails over conventional dislocation motions. The internal stress built up across neighboring grains during the sliding, in turn, is accommodated by grain boundary and tripe junction migration. This process is favored in small grains because less planar interface provides less steric obstacles to the concurrent sliding process. H. Van [45,48] has identified two atomic processed in the interfaces to assist the sliding process: atomic shuffling and stress-assisted free volume migration and both are related to grain boundaries.

$$H_V = H_0 + \frac{k}{\sqrt{d}} \quad \text{for dislocation motion}$$

$$H_V = H_0 - \frac{m_1}{d} \sqrt{d - m_2} \quad \text{for grain boundary sliding}$$

In experiments, the grain boundary sliding was observed as well in deformation of NS materials [43,50–53]. More important, it's further proved such deformation process occurs in a collective way by coordinating a couple of grains' boundaries [43,50]. Small grains group and get aligned together during applied strain by coordinate grain boundaries of each other, which arrives at the minimum configuration of energies.

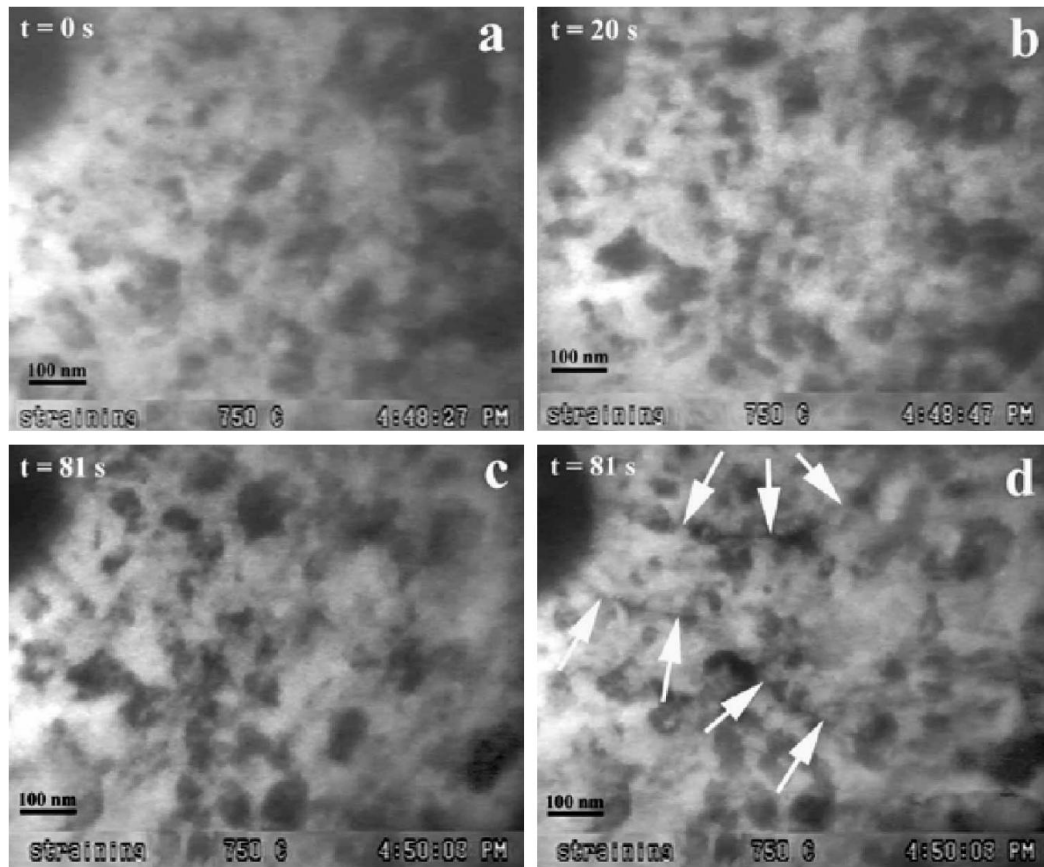


Figure 2.5 Continuous bright-field TEM observations of deformation processes in nanocrystalline Ni₃Al during in-situ tensile test. Arrows in (d) mark the apparent grain boundary sliding features during tension [53].

2.1.2.3 Dislocation emission from grain boundaries

As mentioned in the breakdown of dislocation pile-up section, the generation of intragrain dislocations becomes impractically difficult as the grain size reach nanometer scale, which has been widely accepted in experiments and simulations. Comparing the critical stress to activate dislocation motions from conventional Frank-Read source, the stress of dislocation emission from grain boundaries is relatively lower. Additionally, grain

boundaries of NS materials are usually of non-equilibrium state and high energy and therefore serve as primary dislocation sources and sinks. In fact, full and partial dislocation emissions from grain boundaries have been broadly reported in both computational simulations and experimental observations [47,54–59]. For example, molecular dynamics simulations reveals that grain boundaries plays a critical role in the deformation of nanocrystalline Al, as shown in Figure 2.6 [60]. In contrast to the formation of dislocation tangle, cells, forests within the grain interior in conventional grain size scale, deformation is majorly carried out by the grain boundary mediated dislocation process. In experiments, in-situ observations of deformation in nanocrystalline Platinum and Ni have revealed the dislocation dynamics in grain size even smaller than 10 nm [61,62]. Interestingly, examinations of X-ray diffraction during the deformation of nanocrystalline Ni indicated that the peak broadening process is reversible [63]. Its implication for the deformation physics is no residual dislocation network has been built up during the deformation.

The primary explanation is that the mean free path of dislocations in NS materials is much smaller due to the grain size scale. Therefore, the emitted dislocations have more chances to be absorbed by the opposite grain boundary without mutual interactions. However, there're still minor evidences saying existence of dislocation storage and locks in nanocrystalline materials [61,64]. Note that both observations are not conducted under the conventional uniform elongation of tensile deformation, i.e. the strain level could be much higher than target applications. Regardless the issue of dislocation storage, dislocation generation by grain boundary emission has been generally identified as a crucial deformation mode in NS materials.

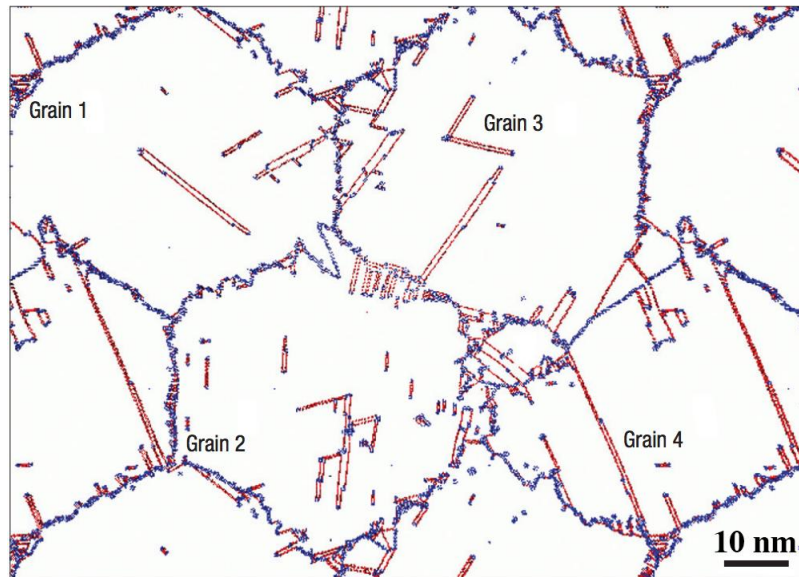


Figure 2.6 A snapshot of nanocrystalline Al at 11.9% plastic strain, showing vast dislocation activity generated from grain boundaries [60].

2.1.2.4 Grain rotation and grain growth

Rotating grains to accommodate plastic strain is first reported by Ke et al. [65], followed by observations of deformation in nanocrystalline Ni and Pt [6,42,66]. Grain rotation as a deformation mechanism in NS materials has been also investigated by MD simulation and analytical modeling [45,67,68]. Wang et al [6] has found that the grain rotation is largely mediated by the grain boundary dislocations under in-situ TEM, rather than grain boundary sliding and diffusion creep [69,70]. They observed that this is more often observed for grains with diameters less than 6 nm, as shown in Figure 2.7. However, TEM observation may not represent the case in bulk NS materials because the sample foil is too thin to reveal the real deformation story. Fortunately, texture measurement also confirmed the grain rotation mechanism in deformation of bulk NS Ni and its alloy [71,72].

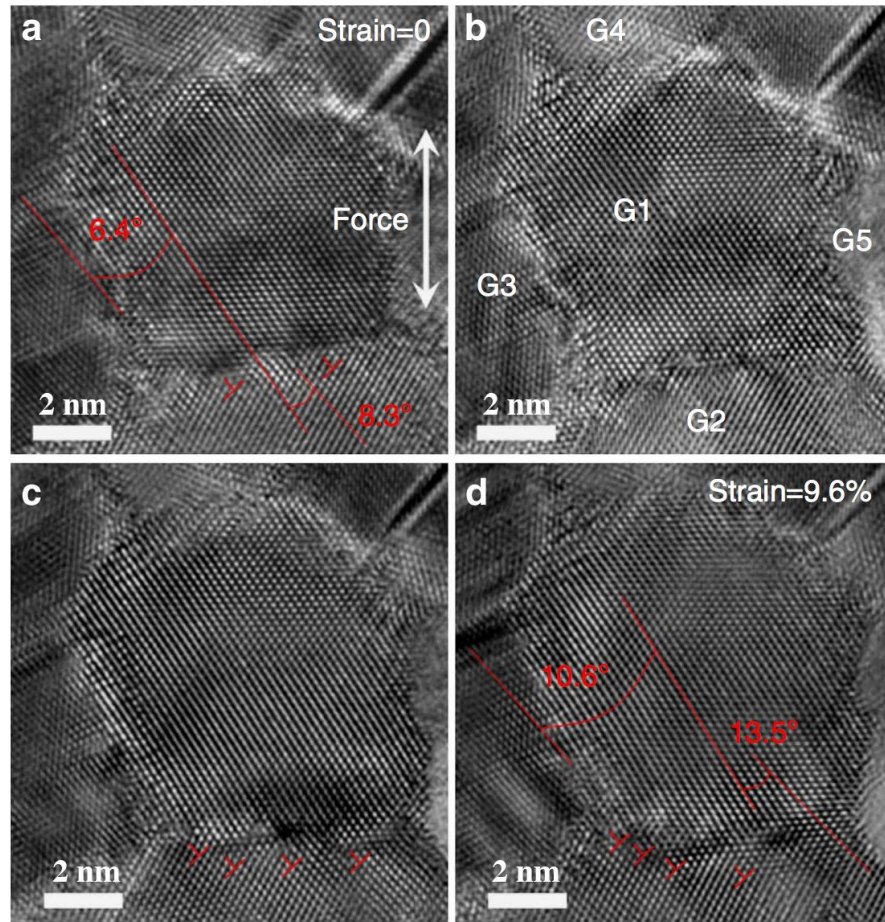


Figure 2.7 Grain boundary dislocations facilitate the grain rotation during tension. Red “T” represents the grain boundary dislocations and red number marks grain orientation difference [6].

Grain growth or coalescence is another deformation mechanism that is sometimes reported accompanied with grain rotation, collectively [73,74]. For example, severe plastic deformation of nanocrystalline Ni and its alloy is accommodated by grain growth that is assisted with grain rotation at high-applied stress. The grain growth is also revealed in the surface nanocrystallized Cu structure, which is believed to provide extraordinary tensile ductility [75]. The grain growth of nanocrystalline Cu can even occur at liquid-nitrogen temperatures and the theoretical modeling investigation shows two necessary conditions: the

existence of impurity and non-equilibrium structures [76–78]. The relation between grain rotation and grain growth is well concluded in Wang et al. [79], as schematically shown in Figure 2.8. Grain rotation facilitates converting high-angle grain boundaries to lower-angle ones. The low-angle grain boundaries then disappear and leave intragrain dislocations. In terms of practical applications, grain growth is hateful and expected to be avoided in design.

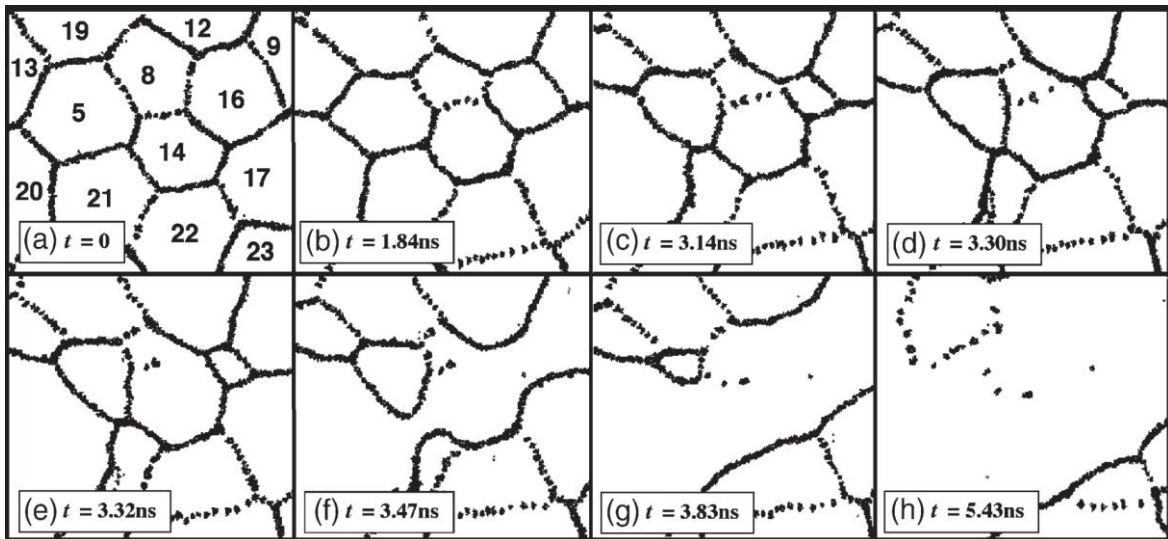


Figure 2.8 Schematic sequence of the deformation evolution of nanocrystalline Pd under shear stress of 0.6 GPa, showing the relative grain rotation followed by mutual coalescence [79].

2.1.2.4 Stacking faults and twinning

In CG face-centered cubic (FCC) and body-centered cubic (BCC) metals, stacking faults and deformation twinning usually occurs in the materials with low stacking-fault energy because of the low-energy principle [80]. While in hexagonal close-packed (HCP) metals, twinning is a common deformation mode due to fewer slip systems [81,82]. In NS

materials, stacking faults and twinning are also observed in FCC and BCC metals and alloys even when their stacking-fault energy is not low [58,58,83,84]. This is largely brought from the high energetic grain boundary and remarkable inhibition of intragrain dislocation motions [57,83]. The generation of stacking faults from grain boundaries are usually the prior condition for deformation twinning. Twinning phenomenon in NS materials is a major focus of this dissertation and will be introduced in details in section 2.2.

2.1.3 New strategies for better tensile ductility of nanostructured materials

Extraordinary efforts have been made to better off the ductility of NS materials by tailoring the microstructures during the decades' development of NS materials. Ma et al. [39] has summarized eight routes to improve the tensile ductility of bulk NS metals and alloys. Some approaches seem to make trade-off between strength and ductility at first glance while other strategies realized the simultaneous improvement of both strength and ductility. Wang et al found a bimodal microstructure with grain size ranging from micro to nano scale, which leads to remarkable improvement of tensile ductility in Cu, as shown in Figure 2.9a-b [85]. The intuitiveness is the superposition of the ductility of CG part and the strength of ultra-fine grained part. Further examination of relevant mechanics revealed that the critical role in this modification is believed to be the generation of massive heterogeneous interface, which is beneficial to the effective accumulation of geometrically necessary dislocations upon deformation [86,87]. High strain hardening and tensile ductility are thereby based on the Considère condition: $d\sigma/d\varepsilon \geq \sigma$. This general principal could also extended to the design of multiphase microstructure, which has been utilized in a Ti alloy and achieved success [88]. Recent gradient/laminate structure development is also pertinent to the bimodal concept,

more or less. Instead, gradient/laminate structures are expected more effective than the simple bimodal microstructures in achieving superior mechanical properties [89]. This is still under study and this dissertation will shed some lights on this issue in later chapters.

Nanosized and secondary precipitates are revealed to be another method to achieve decent tensile ductility in NS materials with or without sacrifice of strength [90–92]. They're effective to initiate, drag and pin dislocations and therefore elevate the strength and hardening capacity [39,93]. Figure 2.9c-d is the tensile curve and the typical microstructure in 7075 Al alloy which utilizes this approach to enhance the mechanical performance [90]. The presence of those precipitations is typically driven by aging after severe plastic deformation. Significant defective sites would be made to promote the precipitation nucleation after this process. Obviously, this strategy is limited to those alloys hold the promise of significant and controllable precipitations.

Nano-scale growth and deformation twins in lieu of the nanograins elevate mechanical properties of NS materials as well [94–96]. This firstly came as a surprise in the electrodeposited Cu by Lu et al. [94] and later on confirmed again in Ma et al. [95]. Zhao and Zhu found this strategy is pretty suitable for the NS FCC materials with lower stacking-fault energy [96]. Twin boundaries are effective obstacles for dislocation motions and primary sites for dislocation accumulations, as shown in Figure 2.10b. They also serve as defects source to maintain the plastic deformation. Therefore, the addition of twins in NS materials promotes the hardening capacity, strain-rate sensitivity and beneficial to the simultaneous improvement of strength and ductility [97–99].

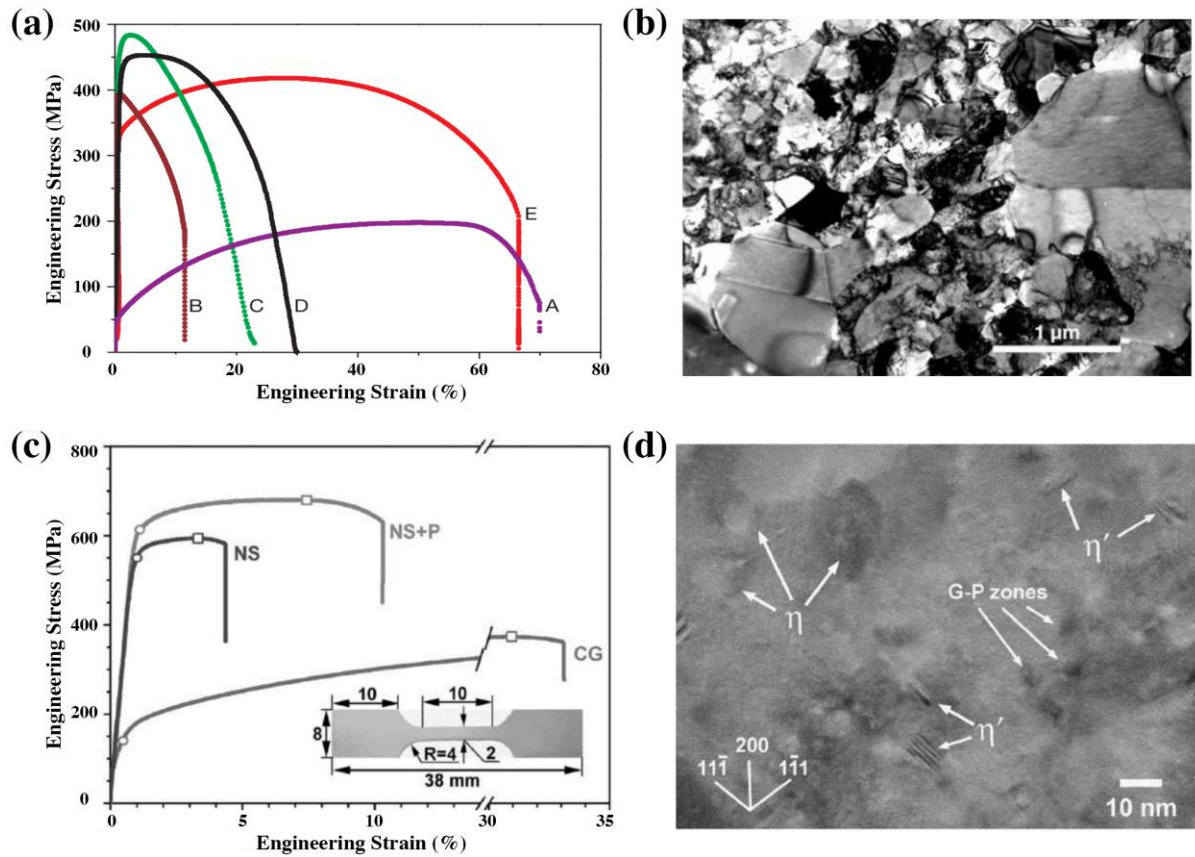


Figure 2.9 (a) Engineering stress-strain curves for pure Cu Curve A, annealed, CG Cu; B, room temperature rolling to 95% cold work; C, liquid-nitrogen temperature rolling to 93% cold work; D, 93% cold work+180oC, 3 min.; and E, 93% cold work+200oC, 3 min. Note the best performance of strength and uniform plastic strain to failure in Curve E. (b) Typical bimodal grain size microstructure in Curve E of (a). (c) Tensile engineering stress-strain curves of the CG, NS and NS+Precipitation samples of 7075 Al alloy. Open circles and squares mark the 0.2% yield strength and the uniform elongation, respectively. (d) HRTEM image along a $\langle 011 \rangle$ matrix zone axis of a NS+Precipitation sample showing spherical G-P zones, plate-shaped η' phase and equiaxed η phase. [85,90]

Stimulated by the importance of twins in NS materials, materials scientists become more interested in how to generate prosperous twin structures in NS materials via either growth or deformation. Deposition growth is always restricted by its thickness scale and therefore difficult to produce bulk materials full with nano-scale twins despite their wide application in labs. Deformation twins seem promising to extend this strategy to the application in bulk NS materials. Therefore, it's of both scientific importance and practical significance to further probe the deformation-twinning phenomenon in NS materials: mechanism, influential factors and their properties.

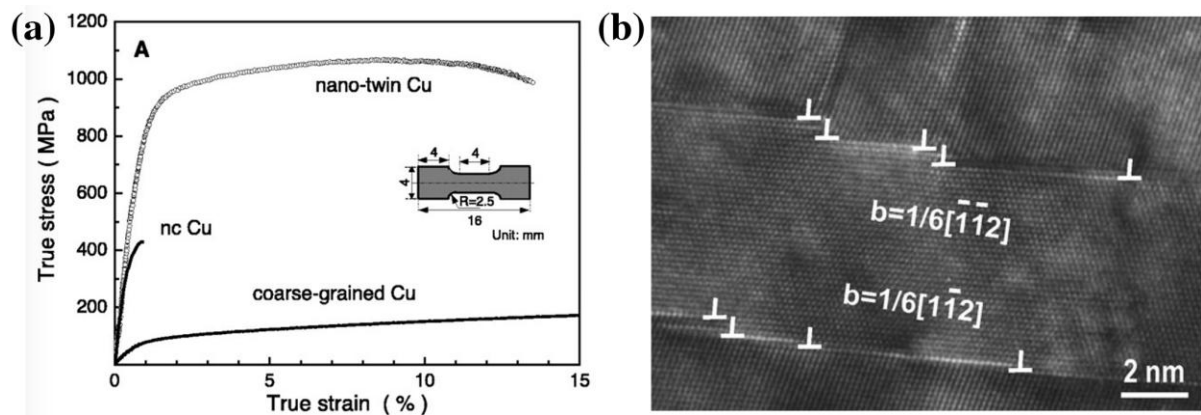


Figure 2.10 (a) Tensile stress-strain curve for an electrodeposited Cu sample with nano-twins in comparison with that for a CG and a nanocrystalline Cu. (b) HRTEM of the nano-twin structures, showing partial dislocation disassociation, dislocation pile-up and at twin boundaries. [94,99]

2.2. Deformation twinning in nanostructured materials

2.2.1 Basics of deformation twinning in FCC materials

Conventionally, deformation twins in FCC metals are believed formed by the slip of partial dislocations with the same Burgers vector on successive planes [80,100]. As shown in Figure 2.11a, if deformation twinning occurs above the twin boundary a spherical grain via partials with a Burgers vector \mathbf{b}_1 , a grain will be sheared into a new shape. Note this will produce a grain boundary kink at the twin boundary with a kink angle of 141° , which is twice of the angle between two close-packed $\{111\}$ planes. The twinning partial dislocations are all Shockley partials that can glide on the slip plane. There are three equivalent Shockley partials on each slip plane. For example, as shown in Figure 2.11b, on the (111) slip plane the three partials are $\mathbf{b}_1 = \mathbf{B}\delta = a/6[2\bar{1}\bar{1}]$, $\mathbf{b}_2 = \mathbf{A}\delta = a/6[\bar{1}2\bar{1}]$, and $\mathbf{b}_3 = \mathbf{C}\delta = a/6[\bar{1}\bar{1}2]$. Note that there are also three partials with opposite Burgers vectors, $-\mathbf{b}_1$, $-\mathbf{b}_2$ and $-\mathbf{b}_3$. On the close-packed (111) slip plane of FCC metals, the atomic stacking sequence in successive planes is ABCABCABCABC. When a partial dislocation glides across a slip plane, a stacking fault is produced and all atoms above the stacking fault change their positions. The atomic stacking position shift caused by the gliding of a partial dislocation can be described below:

Partial \mathbf{b}_1 : $A \rightarrow B, B \rightarrow C, C \rightarrow A$

Partial \mathbf{b}_2 : $A \rightarrow B, B \rightarrow C, C \rightarrow A$

Partial \mathbf{b}_3 : $A \rightarrow B, B \rightarrow C, C \rightarrow A$

In other words, although the three Burgers vectors have different orientations, they cause the same stacking position shift. As will be shown later, this has important implications for

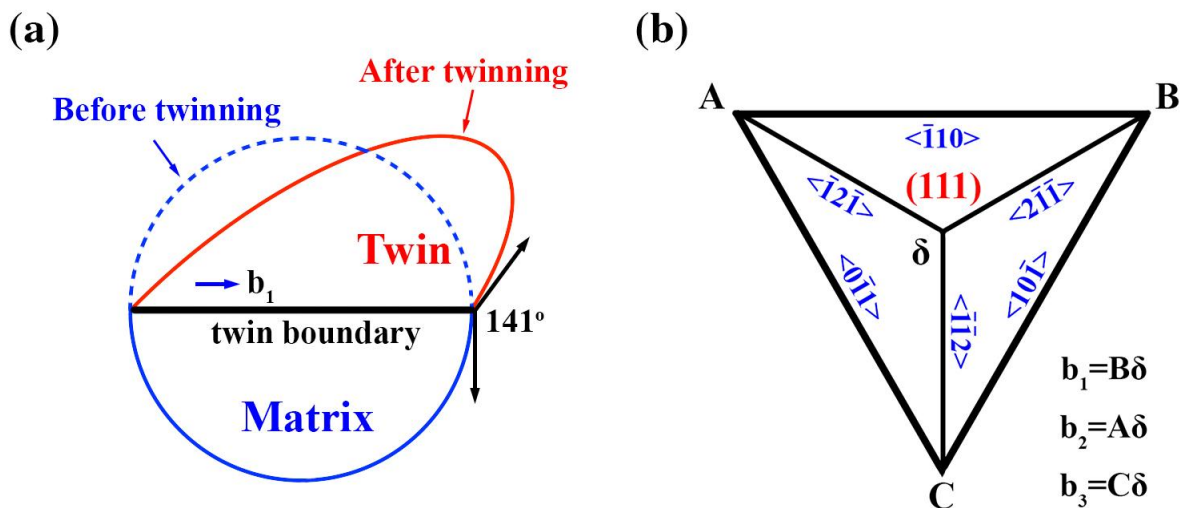


Figure 2.11 (a) Conventional deformation twinning by the gliding of partials on successive slip planes above the twin boundary changes the shape of the spherical grain above the twin boundary. (b) Three equivalent Burgers vectors b_1 , b_2 and b_3 on the (111) slip plane for Shockley partials. [83,101]

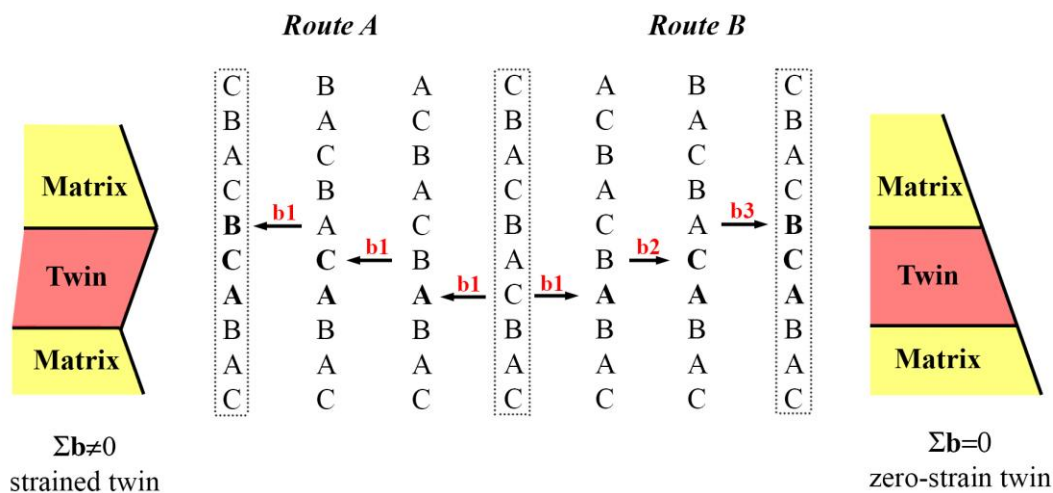


Figure 2.12 The process of forming a three-layer deformation twin by the slip of three partials with (Route A) the same Burgers vector on successive slip planes and (Route B) the slip of three partials with a mixture Burgers vector on successive slip planes. Two sides are schematic illustration of the final twin morphology caused by each route. [102,103]

deformation twinning in nanocrystalline FCC metals. Partial dislocations with opposite orientations, i.e. $-\mathbf{b}_1$, $-\mathbf{b}_2$ and $-\mathbf{b}_3$, will shift the stacking sequence to the opposite direction, i.e. $B \rightarrow A$, $C \rightarrow B$, $A \rightarrow C$. The negative partials cannot slip in a perfect FCC crystal because it is energetically unfavorable.

Route A in Figure 2.12 shows the formation of a three-layer twin via the slip of partials with the same Burgers vector, marked by the bold letter ACB. As shown, the initial stacking has a normal FCC sequence CABABCABC. The slip of the first partial \mathbf{b}_1 produces an intrinsic stacking fault (see the bold letter A), which is identical to removing a layer of C atoms. The slip of the second \mathbf{b}_1 partial on an adjacent slip plane converts the stacking fault into a two-layer twin nucleus (AC). Further slip of \mathbf{b}_1 partial grows the twin nucleus into a three-layer twin ACB, with the twin boundaries represented by two horizontal lines at left side. Since the twinning process described in Route A involves only partials with the same Burgers vector, we name such a process as monotonic twinning process. Route B shows that a three-layer twin with identical stacking sequence can also be produced by the slip of three partials with mixture of three Burgers vectors (\mathbf{b}_1 , \mathbf{b}_2 and \mathbf{b}_3) on successive slip planes. In other words, a twin can be formed by the slip of identical partials or different partials. This is because the three partials, \mathbf{b}_1 , \mathbf{b}_2 and \mathbf{b}_3 , produce the same stacking sequence shifts despite of their orientation difference. It should be noted that the macroscopic strain produced by the two twinning processes described in Figure 2.12 are very different. In Route A, all partials have the same Burgers vector, and therefore produce a shear strain in the same direction. This can collectively produce a macroscopic strain and change the grain shape as shown. In contrast, the twinning process described in Route B will produce a much smaller and even

zero macroscopic strain because partials with different Burgers vectors shear the lattice to different directions. As discussed later, most twinning mechanisms proposed for the FCC metals with coarse grains are consistent with the twinning process described in Route A, while the twinning process described in Route B could be common in nanocrystals. Factors influencing Route B in nanocrystalline FCC metals will be further elucidated.

2.2.2 Grain size effect on twinning and mechanisms

2.2.2.1 Observation of grain size effect on twinning

The grain size effect on deformation twinning was observed mostly by experimental observations [83,104] because computer simulations always have the size limit. In this section, we present the experimental observations on the grain size effect for a broad grain size range from coarse-grains (larger than 1 μm) to nanometer-sized grains (smaller than 100 nm), which can be schematically described in Figure 2.13. Briefly, in the coarse-grain size range, deformation twinning becomes more difficult with decreasing grain size for FCC, BCC and HCP metals [105], whereas in the nanocrystalline grain size range, with decreasing grain size twinning first becomes easier (the normal grain size effect) and then more difficult (the inverse grain size effect) [106,107]. This results in an optimum grain size that is easiest to deform by twinning for FCC metals. However, the twinning behavior in nanocrystalline bcc and hcp metals have not been well studied, although it is generally observed that nanocrystalline hcp metals are more difficult to twin than their coarse-grained counterparts. It should be noted that the critical grain size for the transitions in deformation twinning behavior may be affected by intrinsic material properties such as the stacking fault energy

[108,109] and shear modulus as well as external deformation conditions such as strain rate and deformation temperature.

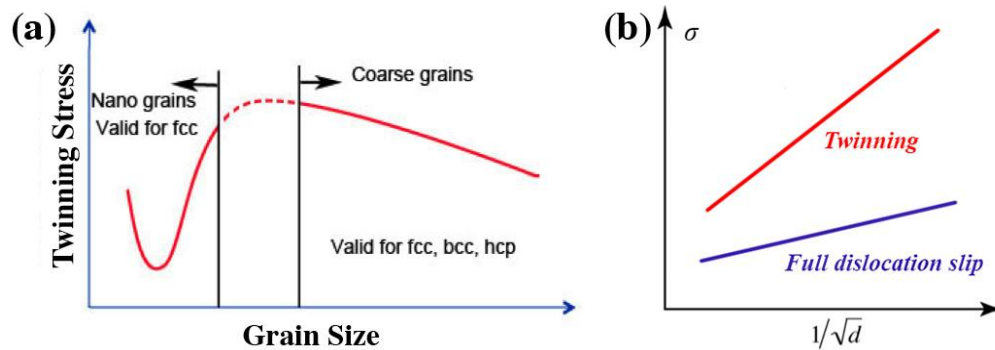


Figure 2.13 Schematic description of grain size on the critical stress needed to activate deformation twinning. The grain size effect for nanocrystalline bcc and hcp metals is uncertain. The schematic of Hall-Petch relationship for twinning and full dislocation slip in CG metals and alloys, σ is the stress and d is the grain size. [83,110]

It has been observed that larger grains are easier to deform by twinning for coarse-grained materials. This was explained as follows. It is well known that the critical stress for dislocation slip can be described by the Hall-Petch relationship $\sigma_S = \sigma_0 + k_S d^{-1/2}$, where d is grain size, σ_0 is a constant, and k_S is the Hall-Petch slope for dislocation slip. Experimental results indicate that the critical stress for twinning also shows a Hall-Petch type behavior, $\sigma_T = \sigma_0' + k_T d^{-1/2}$, where k_T is the Hall-Petch slope for twinning. Table 2.1 summarizes the Hall-Petch slopes for both dislocation slip and twinning for some FCC, BCC and HCP metals. For CG FCC metals, it is obvious that k_T is larger than k_S , which means that with decreasing grain size the critical stress required for twinning increases faster than that for dislocation slip, as

schematically illustrated in Figure 2.13b. In other words, twinning becomes more difficult than dislocation slip with decreasing grain size. The physical reason for such a grain size effect in CG metals is not understood. Yu et al. recently attempted to explain such a phenomenon by a “stimulated slip” mechanism [111]. More studies are needed to probe its fundamental physics. It should be noted that these experimental observations are not consistent with the classical dislocation model [33] that has been used to explain the grain size effect on twinning [112,113].

Table 2.1 The Hall-Petch slopes for fcc, bcc and hcp metals and alloys [105].

Material	k_S for dislocation slip	k_T for twinning	k_T/k_S
FCC			
Cu	5.4 (RT)	21.7 (77K)	4
Cu-6 wt%Sn	7.1	11.8 (77K), 7.9 (RT)	1.7, 1.1
Cu-9 wt%Sn	8.2	15.8 (77K)	1.9
Cu-10 wt%Zn	7.1	11.8 (77K)	1.7
Cu-15 wt%Zn	8.4	16.7 (295K)	2.0
BCC			
Fe-3 wt%Si	12	100	8.3
Armco iron	20	124	6.2
Steel (1010, 1020,1035)	20	124	6.2
Fe-25 at%Ni	33	100	3.0
Cr	10.1	67.8	6.7
V	3.5	22.4	6.4
HCP			
Zr	8.3	79.2	9.5
Ti	6	18	3.0

Interestingly, the ratio of Hall-Petch slope for twinning to that for dislocation slip, k_T/k_S , is larger for BCC and HCP systems than for FCC systems. This suggests that the grain size effect on twinning is larger in CG BCC and HCP systems than in CG FCC systems.

Experimentally, deformation twinning was found active in nanocrystalline FCC metals even with medium to high stacking fault energy, although their CG counterparts normally do not deform by twinning. But molecular dynamics simulations gave different considerations: some results revealed twinning as a major deformation mechanism [114], while others found twinning difficult and rare [115]. These reports raised a controversy on if nanocrystalline FCC metals were more favorable to deformation twinning than their coarse-grained counterparts.

The above controversy was solved by the experimental observation of grain size effect on deformation twinning in nanocrystalline FCC metals [106]. In a systematic study, an electrodeposited nanocrystalline Ni foil with grains in the range of 10-75 nm and an average grain size of ~25 nm were deformed under several conditions [116]. Very few twins were observed in the undeformed Ni sample. Figure 2.14 shows the histograms of (a) grain size distribution and (b) fractions of grains containing stacking faults and twins in samples deformed under tension at liquid nitrogen temperature at a strain rate of $3 \times 10^{-3} \text{ s}^{-1}$ to a strain of 5.5%, and a flow stress of 1.5 GPa. Figure 2.14b shows that with decreasing grain size the fraction of grains containing twins first increases and then decreases, while the fraction of grains containing stacking faults increases monotonically. The fraction of twinned grains is a good statistical indicator of twinning propensity. Therefore, Figure 2.14 indicates that with decreasing grain size the twinning propensity first increases and then decreases in

nanocrystalline FCC Ni. The decrease of twinning propensity with decreasing grain size is called the inverse grain-size effect. The observation of normal grain size effect and inverse grain size effect effectively reveals an optimum grain size range for the activation of deformation twinning in nanocrystalline FCC metals. In other words, the deformation twinning is easiest to form at a certain grain size in the nanocrystalline FCC metals. As will be demonstrated later in an analytical model, the optimum grain size is determined by intrinsic material properties such as stacking fault energy, shear modulus, Poisson's ratio and lattice parameter. External factors such as deformation temperature, strain rate and applied stress may also have an effect, but this is not well understood and needs further study. The observations shown in Figure 2.14 were also verified by synchrotron and neutron diffraction [117]. These observations suggest that optimum grain size for twinning is a common phenomenon in nanocrystalline FCC pure metals.

One of the salient features of the data in Figure 2.14 is that no inverse grain-size effect exists for stacking faults. This is believed due to the effect of generalized planar fault energies on the nucleation of twins, which make it more difficult to activate twinning partial than to activate the first partial to form stacking fault. In other words, the observed grain size effect on the deformation twins and stacking faults can be explained by the combined effect of grain size effect and the general planar fault energy effect. A recent study [118] viewed the grain size effect from the perspective of preference of grain orientation. Their analysis used the similar concept in our following mechanism discussion.

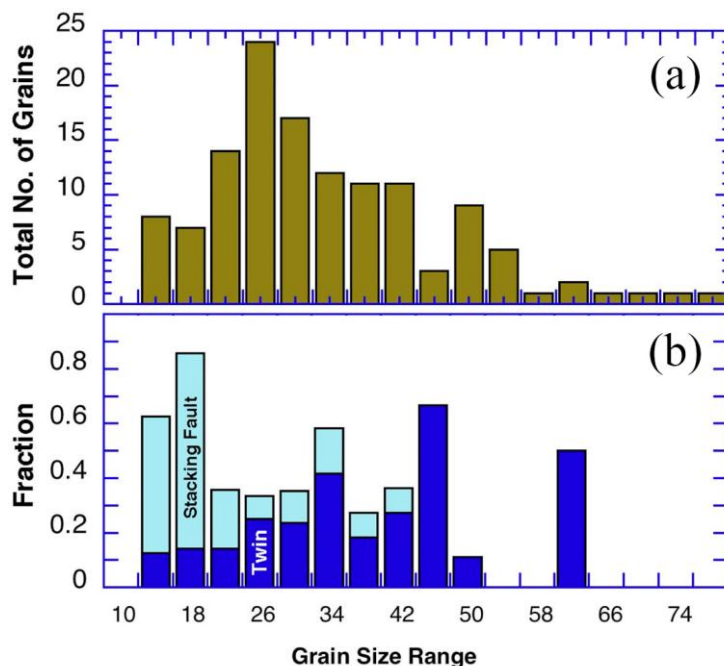


Figure 2.14 Statistical grain size effect on the formations of stacking faults and deformation twins in nanocrystalline Ni deformed under tension at liquid nitrogen temperature. (a) The size distribution of all grains examined under HRTEM. (b) The fraction distribution of grains containing stacking faults and twins. [116]

Deformation-induced detwinning has also been observed both experimentally and in molecular dynamics simulations [119,120]. This raises a critical issue on the effect of grain size on the competition between deformation twinning and detwinning. Understanding this issue would help us to predict the stability and evolution of microstructures and mechanical properties of nanocrystalline fcc materials with twins as a major structural feature and with deformation twinning as a major deformation mechanism.

Detwinning was systematically studied by [121] using an electrodeposited nanocrystalline Ni-20Fe (wt%) alloy with pre-existing growth twins and an average grain

size of 20 nm. The grain sizes were systematically increased by plastic deformation using a technique called high-pressure torsion (HPT). Plastic deformation is known to induce grain growth in nanocrystalline materials. The average grain size increased to 115 nm after 30 HPT revolutions, making it possible to study statistical changes in twin density during deformation over a wide nano-grain size range from 10 nm to over 100 nm.

Figure 2.15 shows the evolution of the size distribution of both all grains and the subset of grains containing twins with increasing numbers of HPT turns. The initial as-deposited sample has a narrow grain size distribution in the range of ~10-35 nm, and about 30% of these grains contain growth twins that were formed during the sample synthesis (Figure 2.15a). The plastic strain increases with increasing HPT turns. As shown in Fig. 8b, after 5 HPT turns, the average grain size increased to about 40 nm and the grain size distribution was broader. Significantly, only 7% of these grains contain twins, which is a dramatic drop from the initial state. These observations indicate that extensive de-twinning occurred during the HPT deformation. Further examination of Figure 2.15b-f reveals the following twinning and detwinning behavior with increasing grain sizes. At grain sizes below 40 nm, existing twins were annihilated by the detwinning process. When the grains grew to sizes above 40 nm, especially around 70 nm, twins reappeared due to the activation of deformation twinning. When grains further grew to above 110 nm, the detwinning process dominated over the twinning process, leading to the disappearance of twins.

The above experimental observations can be summarized as follows. There exists an optimum grain size range for the formation of deformation twins. Outside of this grain size

range, the detwinning process dominates and annihilates existing twins. The mechanisms for these observed twinning and detwinning behavior will be discussed later.

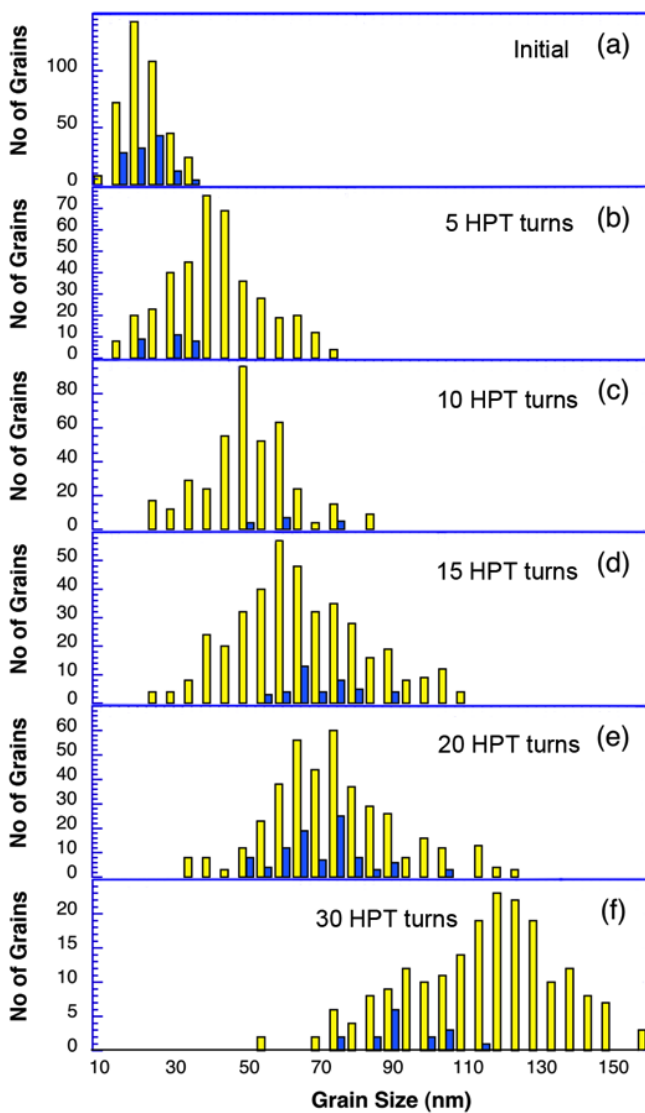


Figure 2.15 The size distribution of all grains (light yellow bars) and grains that contain twins (dark blue bars) with increasing HPT turns in a nanocrystalline Ni-20wt.% Fe alloy. The statistical data are measured using HRTEM, with sample in a location close to the edge of each HPT disk.

2.2.2.2 Mechanisms of grain size effect on twinning

The transition of twinning behaviour from coarse-grained to nanocrystalline fcc metals and alloys is caused by their different deformation mechanisms including dislocation sources and twinning mechanisms. CG fcc metals are believed to twin via several conventional mechanisms including the pole mechanism, the prismatic glide mechanism, the faulted dipole mechanism, or other mechanisms [122,123]. These mechanisms often require a dislocation source in the grain interior to operate. The grain size effect on deformation twinning in CG metals have been explained by Figure 2.13 and Table 2.1, using the concept of Hall-Petch type relationship. However, such relationship is empirical and the real physics based on classical dislocation theory is yet to be discovered.

Nanocrystalline metals and alloys are often free of dislocations in their grain interior [124], although dislocations can exist in nanocrystalline grains under certain deformation conditions. Consequently, dislocation emission from grain boundaries becomes the primary deformation mechanisms. Several twinning mechanisms in nanocrystalline fcc metals have been reported, among which the most often observed is the partial emission from grain boundaries [100]. As introduced in the next section, the change of deformation mechanism and twinning mechanism also changed the effect of grain size on twinning, which is not surprising because different deformation mechanisms are influenced by the grain size in different ways.

The optimum grain size for twinning and the inverse grain size effect on twinning was predicted by an analytical model several years before the experimental observations [125,126]. In the model, the only assumption made is the emission of dislocations from grain

boundaries, which was based on experimental observations and molecular dynamics simulation results [127,128]. For simplicity, the model used a square grain cross-section (see Figure 2.16). The shear stresses needed for the slip of various dislocations, including the leading Shockley partial to produce a stacking faults, the twinning partial, the trailing partial, the detwinning partial, and the lattice dislocation as a function of grain size and shear stress orientation angle were calculated and compared. The dislocation that needs the lowest stress to slip is considered as the active one. A twin is considered nucleated after the leading partial generates a stacking fault across a grain and a twinning partial glides across the grain on the adjacent slip plane. The model indicates that there're two critical stresses are important in determining the optimum grain size for twinning: the nucleation stress of the second (twinning) partial (τ_{twin}) and the nucleation stress for a trailing partial to remove the first partial on the same plane (τ_{trail}). Deformation twinning is statistically promoted when τ_{twin} is less than τ_{trail} under certain preferred grain orientation.

The optimum grain size values and the critical twinning stresses are estimated as [125,126]

$$\frac{d_{\text{op}}}{\ln(\sqrt{2} d_{\text{op}}/a)} = \frac{9.69 - \nu}{253.66(1 - \nu)} \frac{Ga^2}{\gamma_{\text{SF}}}$$

$$\tau_{\text{m}} = \frac{(5.69 - 2.02\nu)\gamma_{\text{SF}}}{2a}$$

where d_{op} is the optimum grain size for twinning, τ_{m} is the critical twinning stress for a nanocrystalline fcc metal, ν is the Poisson's ratio, γ_{SF} is the stacking-fault energy (SFE),

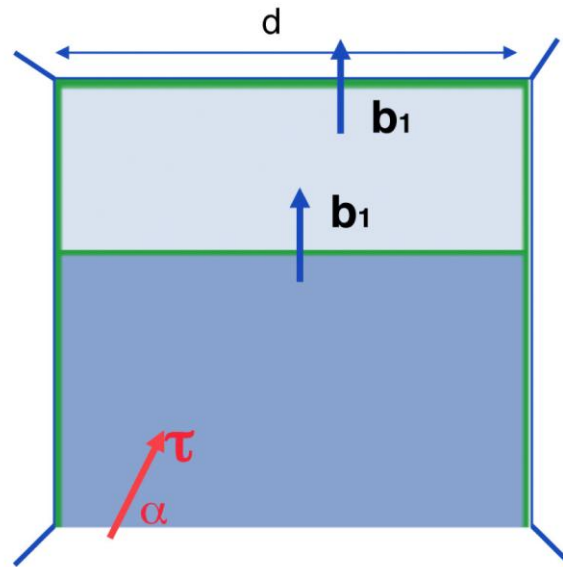


Figure 2.16 A schematic illustration of a dislocation model for the nucleation of a deformation twin via the emission of a twinning partial on a (111) plane adjacent to the stacking fault plane. [125,126]

Table 2.2 The critical stress and optimum grain size for the formation of deformation twinning in some nanocrystalline fcc metals [129].

	G (GPa)	ν	$\gamma_{SF}(\text{mJm}^{-2})$	a (Å)	τ_m (GPa)	d_m (nm)
Ag	30	0.37	22	4.090	0.16	73
Al	26.5	0.345	122	4.04	0.89	6
Au	27	0.44	45	4.080	0.31	30
Cu	54.6	0.343	45	3.6146	0.37	46
Ni	94.7	0.312	125	3.5232	1.06	23

G is the shear modulus, a is the lattice parameter. The critical stress and optimum grain size for deformation twinning in some nanocrystalline fcc metals are calculated using above

equations and listed in Table 2.2. The predicted critical twinning stresses and optimum grain sizes agree well with experimental observations in pure metals [100].

One of the most significant features of this model is its successful prediction of normal and inverse grain size effect on deformation twinning. This is an indicator that the model indeed captured the physics of deformation twinning. However, it also has a major deficiency: it does not consider the effect from the general planar fault energy, which affects the nucleation and gliding of the leading and twinning partials. Consequently, this model cannot explain why no inverse grain size effect is observed for stacking faults. The physical reason for the grain size effect is the deposition of the dislocation lines on the grain boundaries as a dislocation glides under an applied stress. The deposited dislocation lines add strain energy to the system and act to drag the gliding dislocation. The dragging force does not change with grain size d , while the driving force for the dislocation slip is proportional to the length of the gliding section of the dislocation, which is grain size dependent (see Figure 2.16). The driving force needs to overcome the dragging force for the dislocation to glide, and their difference in grain size dependences makes it more difficult for dislocations to move in smaller grains.

2.2.2.3 *Optimum grain size for twinning in nanostructured materials*

Figure 2.15 shows an optimum grain size range in which the deformation twins appear in a large fraction of grains. This grain size range is important for designing nanocrystalline fcc metals with twins as an important structural feature for enhancing the strength and ductility. For microstructures with grain sizes outside of this range, the built-in twins will be gradually annihilated during deformation by a detwinning process. On the other

hand, a stable high twin density could be maintained if the grains sizes are in this optimum range. This is a critical issue under some service conditions such as fatigue where the cyclic stress could induce extensive dislocation/twin interactions. The detwinning process could significantly soften the material, which may lead to the accelerated failure.

The existence of such an optimum grain size for highest twin density can be understood with the following analysis. As discussed in previous sections, in a nanocrystalline fcc metal there exists a grain size range within which deformation twins would form. However, the detwinning process can be caused by the interaction between the dislocation and the twin boundary, which occurs in grains of all sizes. It was found that the detwinning tendency is stronger at small grain sizes than at large grain sizes [121] because the detwinning process involves dislocation interactions with twin boundaries, which needs to overcome relatively high-energy barriers [41]. Materials with smaller grains deform plastically under a higher applied stress, which makes it easier to overcome the energy barrier for detwinning. Therefore, detwinning should be statistically easier in smaller grains. From the above discussions, the tendency for twinning and detwinning during plastic deformation can be schematically illustrated as in Figure 2.17. For a sample whose grain sizes are outside of the optimum grain size range, the detwinning process dominates over the twinning process, which leads to the annihilation of twins. On the other hand, for a sample whose grain sizes are in the optimum grain size range, the twinning process prevails over the detwinning process, which leads to the formation of deformation twins in a large fraction of grains. The twinning process and detwinning process eventually reached a dynamic equilibrium, which produces a stable twin density and microstructure.

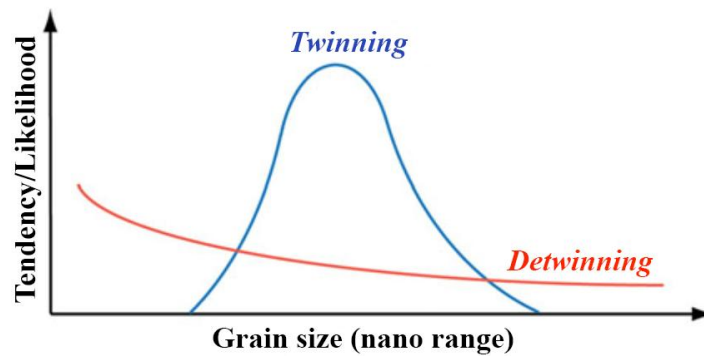


Figure 2.17 Schematic illustration of the grain size effect on the twinning and detwinning tendency.

2.2.3 Macroscopic strain of deformation twins and mechanisms in FCC materials

2.2.3.1 Observation of zero-strain deformation twinning in nanocrystalline FCC metals

As introduced in Section 2.2.1, conventional twinning in fcc metals formed by partials with the same Burgers vector may have a grain boundary kink of 141° if viewed from an appropriate $\langle 110 \rangle$ orientation (shown in Figure 2.11). Such twin-grain boundary morphology is also observed in nanocrystalline fcc materials and may represent the highest macroscopic strain that can be generated by a deformation twin [130]. Figure 2.18a is a HRTEM micrograph of such a twin in nanocrystalline Cu synthesized by HPT, whose twin morphology is the same as that of in coarse-grained fcc metals. However, in nanocrystalline fcc metals, deformation twins can be also formed by partials with different Burgers vector and therefore the macroscopic strain could be lower and be even zero. The two different deformation routes in Figure 2.11 is the schematic illustration of this difference.

Figure 2.18b shows another HREM image of deformation twins in nanocrystalline Cu, which indicates the zero macroscopic strain [130]. As shown, the grain boundary

segments were smooth even at locations where they intersect the twin boundaries, suggesting that these deformation twins shown in Figure 2.18b did not produce macroscopic strain of the grain. This phenomenon was thereafter observed in other fcc materials like pure nanocrystalline Cu and Cu-Ni alloys under both normal and severe deformation conditions [131,132], confirming the universality of this twinning behavior in nanocrystalline fcc metals. Studies also shows that the zero-strain twinning prevails over the twinning with strain in nanocrystalline Ni and Cu. It's also noted that external deformation conditions may also affect the zero-strain twin fractions. Experiments on nanocrystalline Ni in Wu et al. (2008) indicates that lower flow stress will promote the zero-strain twins. It's generally believed that the critical stress for zero-strain twinning is lower than that to conventional twinning.

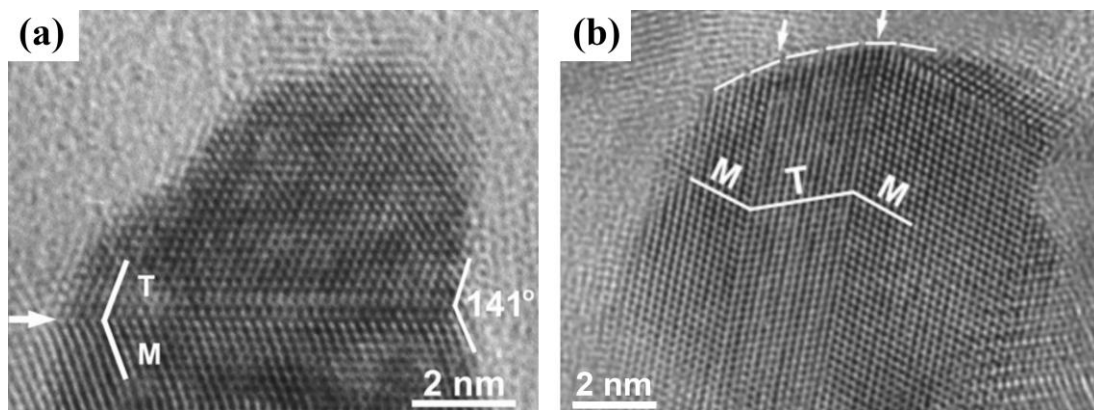


Figure 2.18 (a) HRTEM micrographs of twins in nanocrystalline Cu synthesized by high-pressure torsion. The arrow indicates the twin boundary. (a) A grain boundary has a 141° kink at its intersection with the twin boundary. (b) A zero-strain deformation twin with smooth intersection with the grain boundary (indicated by the broken curve).

Zero-strain deformation twinning helps us with understandings of mechanical behavior and microstructural evolution of nanocrystalline metals. For example, instead of locally accumulating macroscopic strain in twinned grains, zero-strain twins participate in plastic deformation by re-orienting the lattice without producing jagged grain boundaries, which makes it easy for grains to rotate and slide during further deformation [100]. Another salient feature of zero-strain twins is the easy migration of incoherent twin boundaries (ITBs) under slight external stress. This feature is believed to play a critical role in strain softening [134,135].

Up to date, there have been a couple of mechanisms proposed for the formation of zero-strain twins in nanocrystalline fcc metals. Generally, it could be classified into two major categories. One is the random activation of partials (RAP) and the other is named as the cooperative slip of three partials (CSTP). The coexistence and competition of both mechanisms in nanocrystalline fcc materials is recently studied as well.

2.2.3.2 *Random activation of partials (RAP)*

RAP mechanism was proposed by Wu et al. (2008) at the first observation of zero-strain twinning phenomenon. Figure 2.11b illustrates a set of Shockley partials involved in the RAP process. As shown, on the (111) slip plane, there are three Shockley partials, $\mathbf{b}_1=\mathbf{B}\delta$, $\mathbf{b}_2=\mathbf{A}\delta$, and $\mathbf{b}_3=\mathbf{C}\delta$. It's obvious that $\mathbf{b}_1+\mathbf{b}_2+\mathbf{b}_3=\mathbf{0}$. As discussed before, a twin can be formed by the slip of identical partials or different partials, because the three partials, \mathbf{b}_1 , \mathbf{b}_2 , \mathbf{b}_3 , produce the same stacking sequence shifts despite of their orientation difference. Therefore, if all of the three partials propagate in equal number of times, one after another, there will be no net accumulation of macroscopic strain. Consider a Shockley partial dislocation loop on a

(111) plane with the Burgers vector $\mathbf{b}_1 = 1/6[2\bar{1}\bar{1}]$. Figure 2.19 illustrates such a dislocation loop emitted from a grain boundary triple junction and deposited on other segments of the grain boundary of a hexagonal grain. Part of the dislocation line segments parallel to grain edges AB and DE has pure screw character and can easily cross-slip in the GB to the next slip plane. On the next slip plane, \mathbf{b}_1 can slip by itself under appropriate stress or produce other dislocations via the following two reactions:

$$\frac{a}{6}[2\bar{1}\bar{1}] = \frac{a}{6}[\bar{1}2\bar{1}] + \frac{a}{2}[1\bar{1}0], \text{ or } \mathbf{b}_1 = \mathbf{BA} + \mathbf{b}_2$$

$$\frac{a}{6}[2\bar{1}\bar{1}] = \frac{a}{6}[\bar{1}\bar{1}2] + \frac{a}{2}[10\bar{1}], \text{ or } \mathbf{b}_1 = \mathbf{BC} + \mathbf{b}_3$$

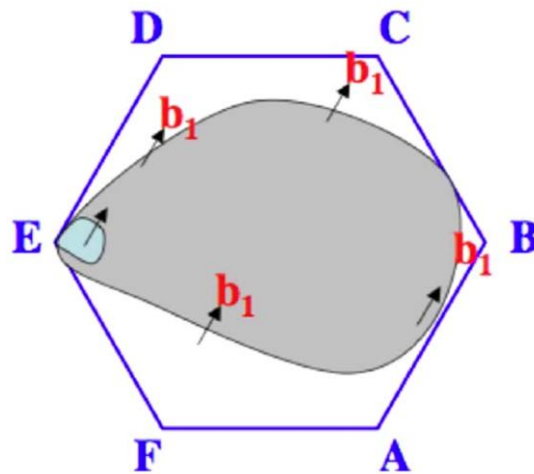


Figure 2.19 A Shockley partial dislocation loop with Burgers vector \mathbf{b}_1 emitted from a grain boundary triple junction at E, grows, and deposits on other grain boundaries of a hexagonal grain. Part of the dislocation line segments parallel to grain edges AB and DE has pure screw character and can move along the grain boundary to the next slip plane.

Thus it is possible to randomly emit the three Shockley partials, \mathbf{b}_1 , \mathbf{b}_2 and \mathbf{b}_3 , on the next (111) slip plane. A global shear stress cannot drive the three partials simultaneously. So what drives the \mathbf{b}_1 , \mathbf{b}_2 and \mathbf{b}_3 partial slip? It is argued that it is possible for these partials to randomly nucleate and slip one at a time, driven by changing local shear stresses. These stresses could significantly differ from the global shear stress. The possibility of such scenario is revealed by atomistic simulations under stress concentration of 3–3.5 GPa, which is many times higher than the applied shear stress, near the edge of a stacking fault [136]. Furthermore, grain boundary sliding and grain rotation, significant in nanocrystalline materials, alter local stress state and/or change the orientation of the twinning grain [137]. These local stress variations can promote the random emission of partials. Other locations for high local stress concentration include triple junctions, and grain boundary ledges.

2.2.3.3 Cooperative slip of three partials (CSTP)

This mechanism was first discovered in detwinning process of fcc materials under in-situ observation of deformation and verified by atomic simulation as well [138,139]. Later on, CSTP is also reported as the mechanism for twinning in nanocrystalline fcc metals like Cu and Ag [132,140]. Figure 2.20a is a HRTEM micrograph of a $\Sigma 3\{112\}$ coherent twin boundary (ITB) in Cu, showing a repeatable pattern of atomic structures. Such ITB can be represented as a set of Shockley partial dislocation on every $\{111\}$ plane with a repeatable sequence $\mathbf{b}_2:\mathbf{b}_1:\mathbf{b}_3$, whose sum of Burgers vector is also zero. CSTP mechanism for twinning is based on the migration and stability of this $\Sigma 3\{112\}$ ITB [138], as shown in the process in Figure 2.20b-d. The initial triple partials are readily emitted from energetic grain boundaries in nanocrystalline materials, which is also proved by a in-situ observation [141]. In the

absence of external stress (Figure 2.20b), each group of triple partials are not far away from each other ($\sim 1\text{nm}$) to achieve their stress balance due to the mutual interactions. In the presence of an appropriate low external stress, one or two partials move ahead to propagate the twin along the favorable direction while other(s) is prevented by the unfavorable stress orientation (Figure 2.20c). Under certain separation due to the propagation, the attraction between Burgers vectors of the partials and the constraint from the new generated stacking fault upon the propagation of moved partial(s) would drag the other partial(s) to catch up, as shown in Figure 2.20d. The triple partials will, again, reach the stress balance between each other after one cycle of the so-called “move-drag” process. This process can be repeated under the drive of external stress and therefore propagate the twin. “Move-drag” mechanism can be also applied to the detwinning process. The favorable propagation direction for twinning or detwinning is determined by the external stress and grain orientation [138].

CSTP mechanism requires a couple of conditions. First, the SFE of fcc materials should be considerably lower to cause the separation of the partials. Simulations have indicated that the operation of CSTP mechanism is easier in Cu and Ag but not favorable in Al [139]. Higher SFE will make the dissociation of the triple partials much harder from a perspective of energy. Second, the twin thickness is another factor affecting this process. Experimental observation and computer simulation have revealed that thinner twins like nanometer twins are easier to propagate by CSTP mechanism because they have less excess energies [138].

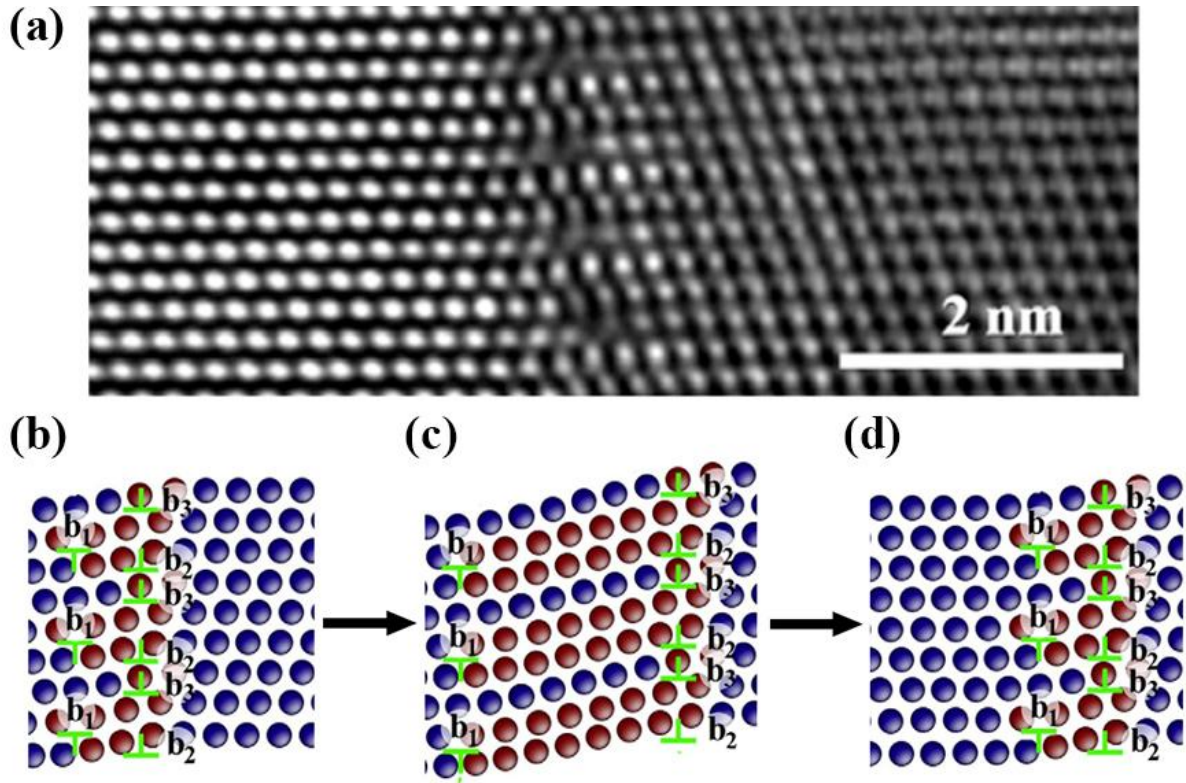


Figure 2.20 (a) HRTEM micrograph of a $\Sigma 3\{112\}$ ITB showing periodic contrast on every three (111) atomic planes. (b-d) Schematic description of CSTP operation, “move-drag” propagation, to generate a zero-strain deformation twin: (b) the initial stable structure of $\Sigma 3\{112\}$ ITB, (c) part of triple partial(s) move ahead under external stress, (d) the rest partial(s) catch up and reach the stress balance again.

2.2.3.4 Coexistence of RAP and CSTP in zero-strain twinning

The two theories on the formation of *zero-strain* twins raise a critical issue: which mechanism plays a major role in the formation of deformation twins with zero-strain nanocrystalline fcc metals? To solve this issue, Wu et al. designed a layer-by-layer microstructure to suppress the RAP and to deter the grain rotation and grain boundary sliding

of nanocrystalline Cu grains during the deformation [142]. In addition, the nano-grains are textured to have their $\{111\}$ planes parallel to the film surface, and the residual stress is oriented to have resolved shear stress on one type of partial dislocations only. Such a microstructure and stress state not only suppresses the RAP mechanisms, but also should promote the CSTP mechanism. It was found that macro-strains were generated in $\sim 56\%$ of the twinned Cu grains, which is lower than previous reports of dominance of zero-strain twinning in pure fcc metals like Ni and Cu. This result shows that with RAP suppressed, zero-strain twins cease to dominate in our nanocrystalline Cu grains. This indirectly proves that the RAP mechanism played a significant role in producing deformation twins with zero-strain. The result also means that the CSTP mechanism accounted for at least 44% of the deformation twins with zero-strain in the current experiment, suggesting that CSTP should be also a major mechanism for producing deformation twins with zero-strain.

Alternatively, another HRTEM studies of nanocrystalline Cu after tension shows two kinds of ITB atomic structures [132], where one is the $\Sigma 3\{112\}$ ITB with repeated pattern and the other is a disordered ITB. These two various features are attributed to the operation of CSTP and RAP processes, respectively. Their observation serves as another evidence to support the coexistence of both mechanisms in nanocrystalline FCC metals.

2.3 Laminate/gradient structures

Laminate/gradient structures have evolved over millions of years in biological world to optimize the multi-functionality of living organisms [143,144]. For example, it's found that the shell of the bivalve *Placuna placenta*, a layered assembly of elongated diamond-shaped calcite crystals, is capable to simultaneously achieve penetration resistance due to the

pervasive nanoscale deformation twinning surrounding the penetration zone, which catalyzes a series of additional inelastic energy dissipating mechanisms in the wake of the existence of dense interfaces in laminate structures [145]. The advantage of laminate/gradient structures is intuitively the full utilization of differing layers/components by combining their unique properties and therefore to maximize the overall mechanical performance like stiffness, fracture toughness, energy dissipation, crack resistance and etc. [144,146–148].

Learning from nature, materials scientists are triggered to develop artificial laminate/gradient materials to cater to the structural requirement in practical applications.

2.3.1 Fabrication of laminate/gradient structures

Although laminate and gradient structures have a lot in common, the fabrication approaches in laboratory are not essentially the same. In this session, we'll, separately, introduce different current methods for laminate and gradient structures, including their advantages/disadvantages and validity.

2.3.1.1 Overview of fabrication methods for metallic laminates

Earlier, Hussey et al. reported the successful fabrication of nickel-aluminides layer structures via the method of vacuum plasma spraying and exothermic in-situ reactions [149]. Xia et al. further found that the tensile strength of metal-intermetallic laminates increase with the increase of volume fraction of intermetallic products, which is reasonable considering the particle strengthening effect [150]. Through reaction between layers, the bonding strength is usually not ideal to burden transverse loading. Directional solidification and arc casting represent another type of techniques attempting to produce metallic laminates from the beginning process of materials [151–153]. This method gave rise to sufficient bonding

strength as the materials are always treated as a whole. But, macroscopically, it's not strictly consistent with the definition of laminate structures despite local satisfaction. Deposition is another direction to go for metallic laminates and achieve certain success [142,154,155]. More often, those laminates are typically referred as multi-layer thin films. Implication of this terminology is the difficulty of scaling up, i.e. deposition is, undoubtedly, beneficial to scientific discovery of fundamental understandings of materials, but not suitable for the production of bulk metallic laminates. There're also some trials on other techniques like high-pressure torsion, friction stir welding, single rolling to process laminates/sandwiches with limited number of layers [156–159].

One of the most promising techniques to fabricate bulk metallic laminates is accumulative roll bonding (ARB), which was firstly reported by Saito et al. to process various metals and alloys including commercial aluminum, Al-Mg alloy and interstitial free steel [17]. The general procedure of ARB is diagrammatic represented in Figure 2.21a [17,160,161]. Experimenters begin with an alternating stack of sheets of two metals/alloys and then carry out the ARB process. Unlike conventional rolling, ARB strains the sample via a cycle of rolling, cutting and restacking, and maintains the original sample dimensions. To prevent oxide contamination at the interface during the entire process, a specific surface treatment like wire brushing and cleaning is typically necessary between cycles. By this way, researchers have successfully fabricated a series of metallic laminates with controllable various layer thickness even reduced to nanometer scale, as shown in Figure 2.21b.

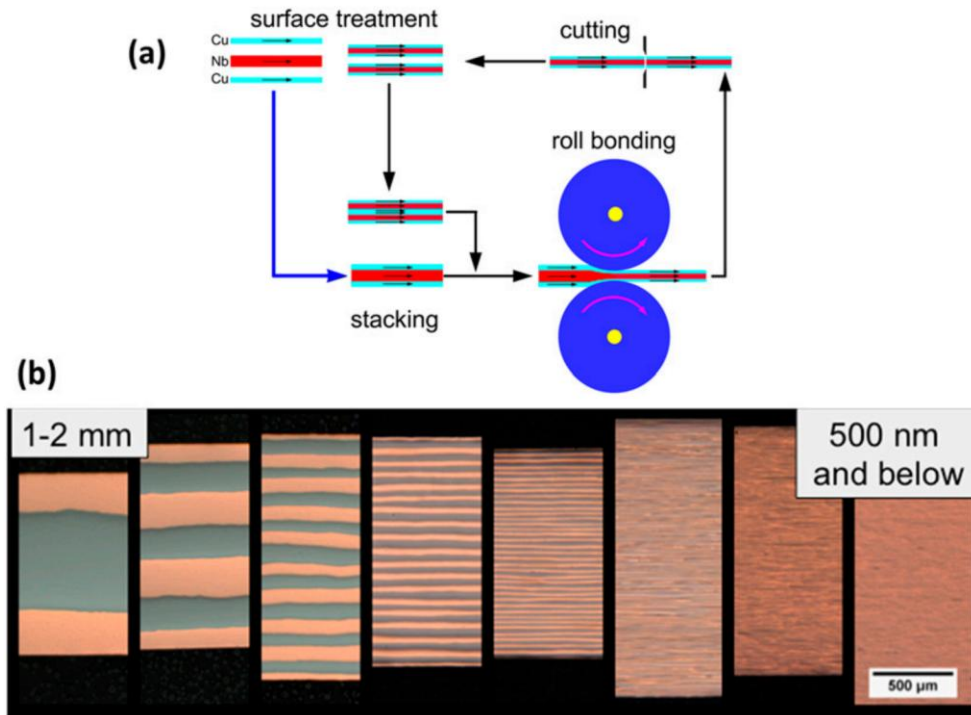


Figure 2.21 (a) Schematically representation of a typical accumulative roll bonding (ARB) process.
 (b) A series of Cu-Nb laminate composites with controllable layer thickness produced by the method in (a). [160]

Another critical feature of ARB is the significant grain refinement it could produce by continuous cyclic processing, which makes it an effective severe plastic deformation method as well [160]. The efficient conversion of strains to 2^n by easily n cycles of processing also leads to the sufficient bonding strength across layers except the last-formed interface. Taking this advantage, ARB holds the capability of fabricating various bulk NS metallic laminates even in university labs [162–164].

Up to date, the limitation of this technique for metallic laminates mostly relies on the following issues. First, the edge-crack gets easily initiated, especially at higher cycles. Some materials, like Al-Mg alloy, are sensitive to those edge-cracks because they propagate readily to the center of the sheets in the subsequent rolling cycle [161]. Second, as a rule of thumb, the last inter-layer interface is not as strong as others since the imposed strain is far less. Last, the surface treatment between processing cycles is critical and sometimes troublesome. Therefore, technically, some as-processed laminates are not strictly free of contamination across layers, which will throw effects on their mechanical properties [165].

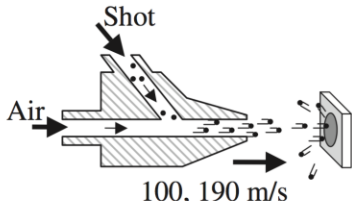
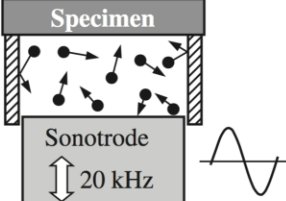
2.3.1.2 Overview of fabrication methods for gradient structures

Gradient structure is not a brand-new concept for manufacturing. The conventional shot-peening technique has something in common with this perception, more or less. However, shot peening doesn't purposely aim at introducing significant grain refinement at surface, but providing compressive stress to avoid the crack initiation and improve the fatigue property [166]. Therefore, conventional shot peening doesn't appear as a well-established method but inspired the community to generate gradient structures by modifying this approach at early attempts.

Assisted with ultrasonic generation, shot peening process could become more efficient by dramatically increasing the frequency of ball impacts. J. Lu and K. Lu first proposed this idea in late of 1990s [167,168]. Further studies shown that microstructures and properties of processed samples could be tuned by the material, size, velocity and amount of the impact balls [169]. Another earlier attempt to achieve surface nanocrystallization is the so-called air blast shot peening, which, typically, uses compressed air to shoot the steel balls

to achieve powerful impacts on specimen and induce deformation and refinement [170,171]. The detailed comparisons of two early techniques are summarized in Table 2.3. It's worth to note the ultrasonic shot peening is not limited to the 20 kHz frequency and further modified to lower frequency like 50 Hz and the processing chamber is also flexible so that some specific requirement can be satisfied as well [172,173].

Table 2.3 Comparison of conditions of air blast shot peening and ultrasonic shot peening [171]

Air blast shot peening	Schematic illustration of equipment	Ultrasonic shot peening
		
ϕ 0.05, 0.3 mm	Shot size	ϕ 0.4 mm
High (> 100 m/s) Velocity distribution - Small	Shot velocity	Low (< 20 m/s) Velocity distribution - Large
Single-direction (~ 90°)	Impact direction	Multi-direction
100, 170 % / s	Coverage rate	20 % / s

In addition to the modification of shot peening, other advanced techniques also achieve success in fabricating gradient structures, mainly by introducing a surface nanocrystallization layer to the CG matrix. For example, Li et al. [174] reported a novel machine-induced plastic deformation method to create surface nanocrystallization, which is called surface mechanical grinding treatment. Basically, it employs a machining tool tip to produce large shear strains (typically 2~10) as well as high strain rate (up to $10^4 \sim 10^6 \text{ s}^{-1}$) in

zones ahead of the tip. With increasing the size of the tip, structural refinement in the surface layer of the ground materials is anticipated due to the severe surface plastic deformation and therefore a gradient structure from the surface to the material interior is expected. The key idea of surface mechanical grinding treatment is conceptually illustrated in Figure 2.22. Gradient structures fabricated by this method have been reported in Cu, Ni, interstitial free steel and various alloys [75,174–177].

Other techniques like friction sliding, wire brushing and friction stir processing also achieve some encouraging results in modifying the surface microstructure, especially grain refinement [178–180]. But generally, the hitherto most popular techniques for producing bulk gradient structures in metals and alloys are the first mentioned two.

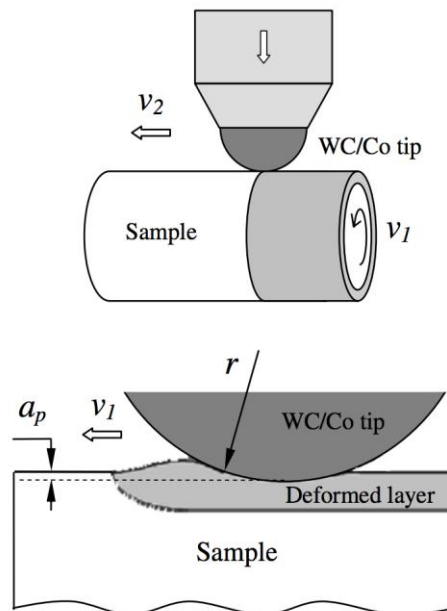


Figure 2.22 Schematic illustration of the surface mechanical grinding treatment set-up and the plastic deformation layer induced by the tool tip. [174]

2.3.2 Mechanical properties of laminate/gradient structures

Generally, investigation of mechanical properties of laminate/gradient metallic structures is a cutting-edge field with a growing body of studies [89,181]. We'll devote two sub-sections to describe their properties researches, separately. Laminate and gradient structures have much in common with respect to fundamental understandings, which will be detailed addressed further. But the reason for the separated descriptions here is the different judgment standards of mechanical properties for these two structures. Usually for laminate metallic structures, two or more materials with various chemical compositions, like aluminum alloy and steel, titanium and its alloy, etc., are processed together [182–184]. Therefore, the most popular approach to tell better performance is to compare the mechanical properties across samples with different total layer numbers/layer thickness in an individual research. Due to the technical difficulties and different experimental details, rare studies made direct comparisons across different groups for the same laminate components. In contrast, for gradient structures, most studies so far focus on the fabrication with one single material component [75,147,175,177]. Not surprising, people could readily make comparisons across all the historical results for this material with various processing and microstructures. Two different methods of assessment have different concentrations and sometimes their conclusions are not comparable to each other.

2.3.2.1 Controversial results in laminate structures

As mentioned in previous section, the most used way to make macroscopic laminate metallic structures is ARB, which will be the focus of following results in comparisons. The resulted relationship between mechanical properties, including strength and ductility, and

layer numbers/layer thickness of laminate samples is really dependent. Different processing routes, base materials, pre-treatments and even operation details will significantly influence the relationship and mask their fundamentals in common. Therefore, there's so far no absolute statement on this issue and we list some of the literature results for reference. Figure 2.23 shows two different trends between mechanical properties versus various ARB cycles. It seems widely accepted that the strength of the laminates is generally increased with the increase of ARB cycles, i.e. fewer layer thickness. However, the ductility or uniform elongation is largely controversial. Figure 2.23a shows a slight increase, or least no obvious drop, of the elongation with increasing ARB cycles in Al/Cu laminates [183]. While Figure 2.23b indicates a distinct trend in Al /Al-12%Si laminate composites: ductility significantly dropped with more ARB cycles [185]. These two dataset are representatives of copious results from ARB processing and truly present the two general trends [186–189].

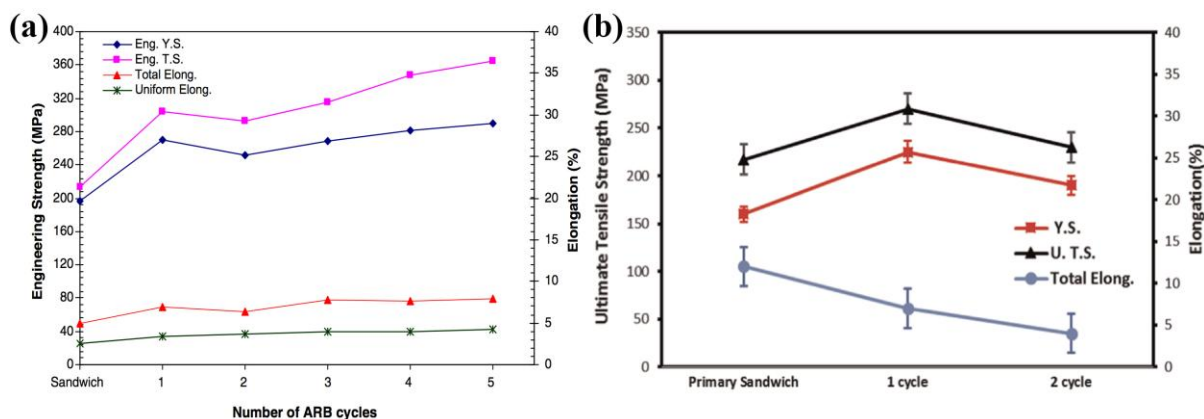


Figure 2.23 (a) Relationship between strength and ductility in (a) Al/Cu samples and (b) Al/Al-12%Si samples: showing two different ductility trends versus number of ARB cycles. [183,185]

It's worth to bear in mind that the presented data doesn't include any post-processing after ARB, which would add complication to the comparison. However, post annealing is sometimes preferred for the specific scientific purpose in research. An example will be shown in Chapter 6 and 7.

2.3.2.2 Beyond rule-of-mixture in gradient structures

Unlike the disputable observations in laminate structure, the mechanical properties in gradient structures have been found, in most cases, better off than their conventional counterparts. Researches on pure Cu and interstitial free steel show a great improvement of the overall mechanical performance by elevating the strength without noticeable sacrifice of ductility in tension. These results are summarized in Figure 2.24a-b. Note that both gradient structures embrace a particular nanocrystallized surface layer, which was considered to make extraordinary contribution to the observed strength. Meanwhile, the considerable retainment of the ductility is found as a unique characteristic of gradient structures, whose mechanism is still not fully understood.

Lu et al. has proposed that the combination of strength and ductility of gradient structures will reshape the traditional "banana" curve for engineering materials, making it a outward curve rather than inward one, as shown in Figure 2.25 [89]. The advantage of gradient structures is not simply trading off the balance between two critical properties, but maximizing and achieving one superior combination of them under certain microstructure design. Gradient structures have also been revealed other exceptional mechanical properties like enhancing fatigue and wearing properties, which is not the focus here and thereby not undergo details [190,191].

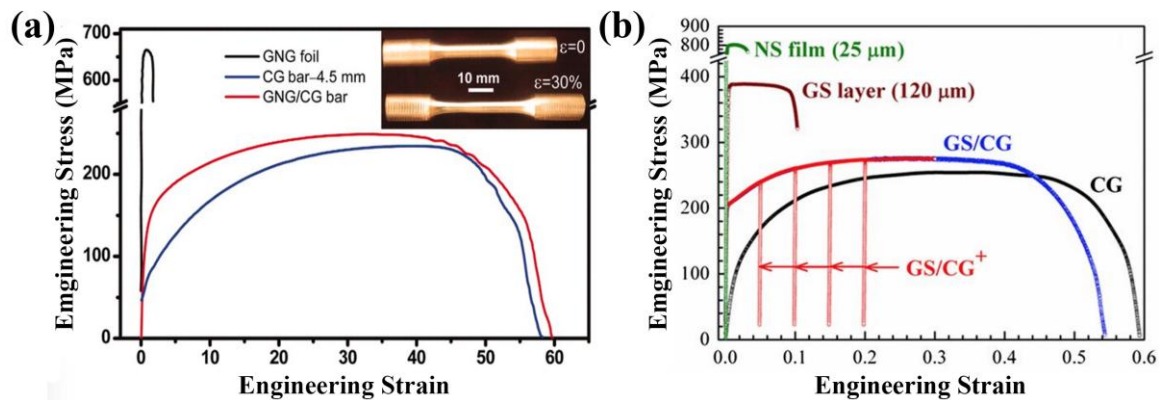


Figure 2.24 Tensile curves of gradient structures of pure (a) Cu and (b) interstitial free steel. Both contain a NS surface [75,147].

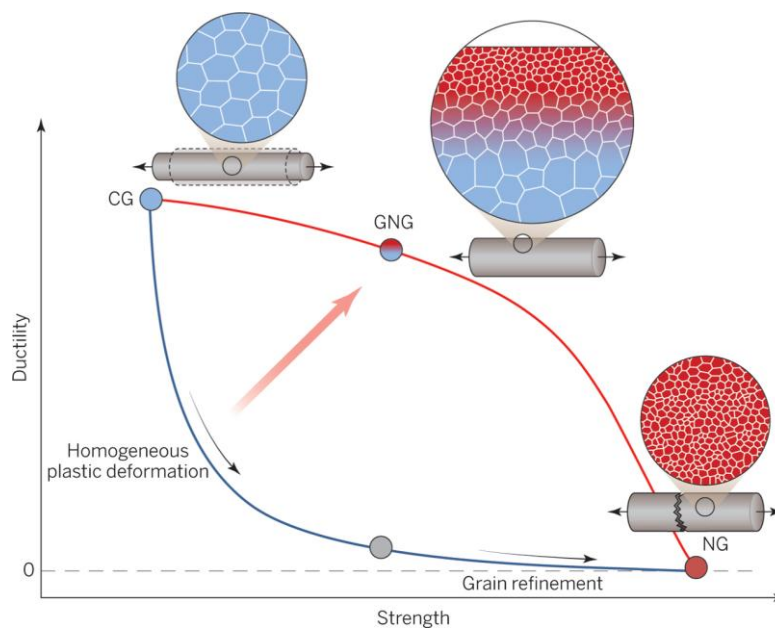


Figure 2.25 Conceptually illustration the strength/ductility relationship in traditional homogeneous microstructure and gradient structure: the strength of a metal is increase at an expense of ductility and follows a typical inward “banana-shaped” curve (blue). However, strength-ductility synergy is achieved with gradient nanograined (referred as GNG) structures (red) [89].

2.3.3 Current perspectives of deformation mechanisms in laminate/gradient structures

Laminates and gradient structures are put together in this dissertation because they have a couple of microstructural features in common. First, they both contains discrepant components within one material matrix, for example, differing grain size. As a natural result, there exist heterogeneous interface across those microstructural discrepancies. Second in mechanics, the material is not elastically or plastically consistent as a whole. Different microstructures respond the deformation in various ways but eventually exhibit a collective result. Both structures experience mechanical incompatibility and need to handle it during deformation in a way, which may have many similarities. The details of the deformation physics is still under investigations and Chapter 6&7 of this dissertation will shed some lights to this topic based on our observations.

The hitherto reported works have proposed several possible mechanisms that play some roles in the deformation of laminate/gradient materials. Early work in gradient Cu focused the interests on the mechanisms for the extended tensile ductility of the surface NS Cu. It was discovered that under the support of CG matrix, the NS Cu is capable to continue plastic deformation by mechanical grain growth, as shown in Figure 2.26. The post-deformation grain size distributions further confirm that the extent of grain growth is positively related to the undergoing strain levels. Fang et al. proposed that the CG matrix provided the most strain hardening during deformation provided and effectively suppressed the emergence of strain localization [75]. Thereby it made room for the sustainable plastic deformation for the very top NS layer based on the Considère condition for plasticity instability for tension.

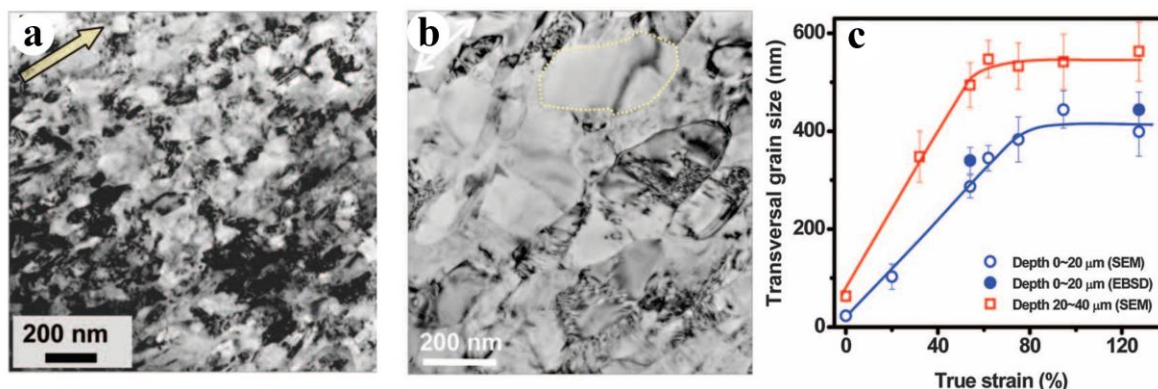


Figure 2.26 (a) A bright-field TEM image showing the grain size distribution of topmost surface of the gradient Cu. (b) The grain size distribution of the topmost layer of the sample after tensile deformation with true strain of 33%. (c) Average grain size measurements in different sample locations with various deformation strains. [75]

Another important proposal regarding the deformation physics in gradient materials emphasized the comprehensive effects from the whole structures during the deformation. Wu et al. observed an up-turn feature in strain hardening curve of a gradient interstitial free steel sample during tension [147]. Interestingly, this up-turn feature is absent when the sample is divided into two parts and tested both standalone (see Figure 2.27a). Wu believed that the extraordinary hardening is caused by the interaction between CG and NS components that compose the whole gradient structure. They further supported this claim by the observation of an extra stress state at lateral surface upon the incompatible deformation, as shown in Figure 2.27b. Most recently, Wu's work in heterogeneous lamella structured Ti indicated the microscopic details of the interaction between CG grains and surrounding finer grains, as shown in Figure 2.27c. By measuring the back stress generated in cyclic tests, they proposed

that the interaction is implemented by back-stress hardening, which generates more dislocations at CG grains than homogeneous structures.

Researches on laminate structures also highlight the roles of the bi-metal interface in mechanical properties. For example, Misra et al. summarized the relationship between strength and layer thickness in Cu/Nb laminates and proposed different deformation mechanism for corresponding length scale [192]. It's found that when the layer thickness is really small, saying a few nanometers, the conventional dislocation pile-up and dislocation bowing breaks down and dislocations are not confined to the individual layer and trying to perform interface crossing, which needs more activation stress and promotes higher strength as observed. Although most metallic laminates haven't reached such extreme length scale, it shed lights on the understandings of the heterogeneous interface role in deformation.

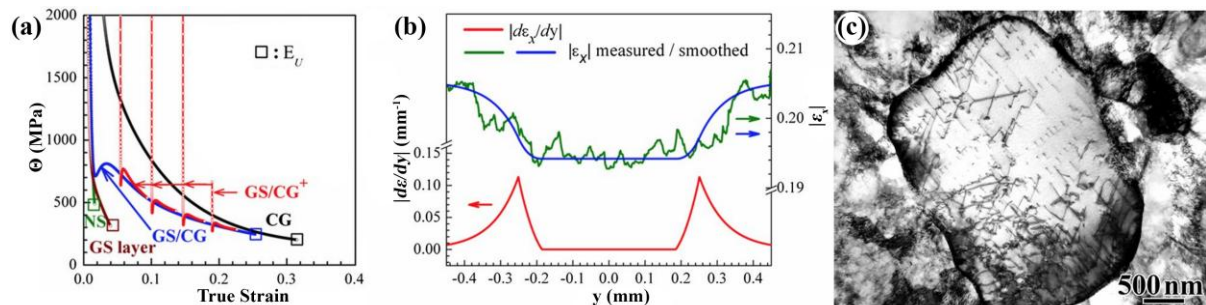


Figure 2.27 (a) Strain hardening rate ($\Theta=d\sigma/d\epsilon$) vs. true strain curves for gradient interstitial free steel sample and its homogeneous counterparts. (b) Measured distribution of lateral strain (ϵ_x) and strain gradient ($d\epsilon_x/dy$) across the thickness along one transverse line across the sample after tension. (c) TEM image showing the dislocation accumulation in a CG grain surrounded by finer grains at tensile strain of 2% of a lamella Ti sample. [147,193]

Generally, there're considerable reports on the delights and advantages brought from the design of laminate or gradient structures on mechanical properties [194–197]. However, the fundamental deformation mechanism regarding the laminate/gradient structures still remains quite blur despite some pioneer studies like mentioned above. It's also one critical interest of this dissertation in later chapters to provide some new perspectives and evidences on this issue. Last but not least, one should also keep in mind that laminate and gradient structures have dissimilarities as well, which may have been glossed over by the extensive description of their similarities before. For laminate structure, the heterogeneous interfaces are usually sharp and stationary during deformation while the interfaces in gradient structures are assumed much smoother and sometimes invisible to microscopy during deformation [75,198]. Another difference is the macroscopic symmetry of the microstructure design. Laminate structures are typically of periodic alteration of their microstructure arrangement while gradient structures reported so far is mostly monotonically graded from interior to the surface or vice versa. There're also not much studies on the potential effect of this difference on mechanical performance, neither.

Chapter 3

General Experimental Techniques

3.1 Sample Preparation

3.1.1 Nanocrystalline Cu-Zn alloys

The raw commercial Cu-Zn alloys with different Zn content (C22000: Cu-10wt.%Zn, C23000: Cu-15wt.%Zn and C26000: Cu-30wt.%Zn) were purchased from McMaster-Carr Supply Company (<http://www.mcmaster.com>) and Zoro (<https://www.zoro.com/>). The composition details of the as-received raw materials are summarized in Table 3.1. The as-received materials are homogenized under 700°C for 3hrs before further treatments. Disks with diameter of 10 mm were punched from the raw materials with its original thickness, following by mechanical polishing with a series of sandpapers to the thickness of 1.5 mm.

Table 3.1 Composition standards for the selected commercial Cu and Cu-Zn alloys [199]

	Cu (wt.%)	Pb (wt.%)	Fe (wt.%)	Others (wt.%)	Zn (wt.%)
C11000	≥99.90	-----	-----	≤0.10	-----
C22000	89.0~91.0	≤0.05	≤0.05	-----	Balanced
C23000	84.0~86.0	≤0.06	≤0.05	-----	Balanced
C26000	68.5~71.5	≤0.07	≤0.05	≤0.15	Balanced

The sample disks were put into a house-built high-pressure torsion (HPT) machine (see Figure 3.1a-b) and subjected to severe plastic deformation at room temperature for 6 revolutions at 1.5 rpm under pressure of 1 GPa to achieve most refinement at disk edges. An example of sample disk before and after HPT was presented in Figure 3.1c. These disks are

original sample for researches in Chapter 4 and 5. The general principle for HPT operation is to assure the material overflow to guarantee the full deformation of the sample.

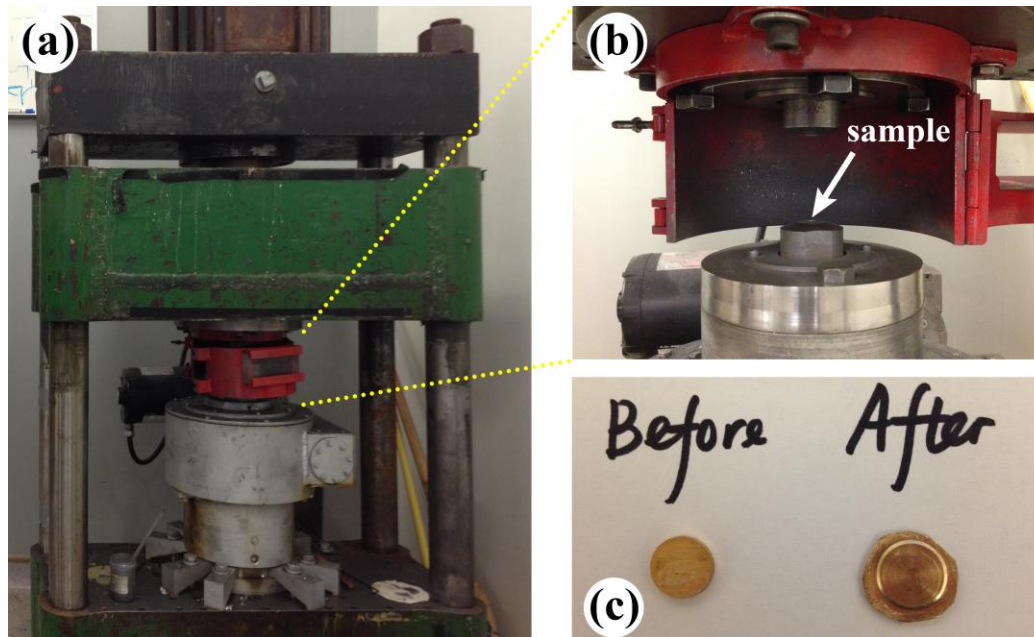


Figure 3.1 (a) Overview of high-pressure torsion (constrained type) facility in lab. (b) The magnification of the central part to hold the sample. (c) Typical sample geometries before and after HPT processing

3.1.2 Nanostructured Cu-10Zn sandwiched by coarse-grained Cu

The sandwich laminates used in Chapter 6 is fabricated by incorporation HPT technique with appropriate rolling and annealing. Φ -10mm disks with desired thickness punched from pure Cu (99.9%) and Cu-10wt.%Zn sheets were carefully cleaned with acetone and ethanol solutions in ultrasonic environment. Thereafter, three disks with the specific order were placed together into the HPT machine and processed under abovementioned

conditions except changing revolutions to 10. The sandwiches were then rolled by a mini rolling machine in lab (Figure 3.2a) to the desired the thickness, followed by annealing at 240°C for 2hrs in vacuum tube furnace, as shown in Figure 3.2b.

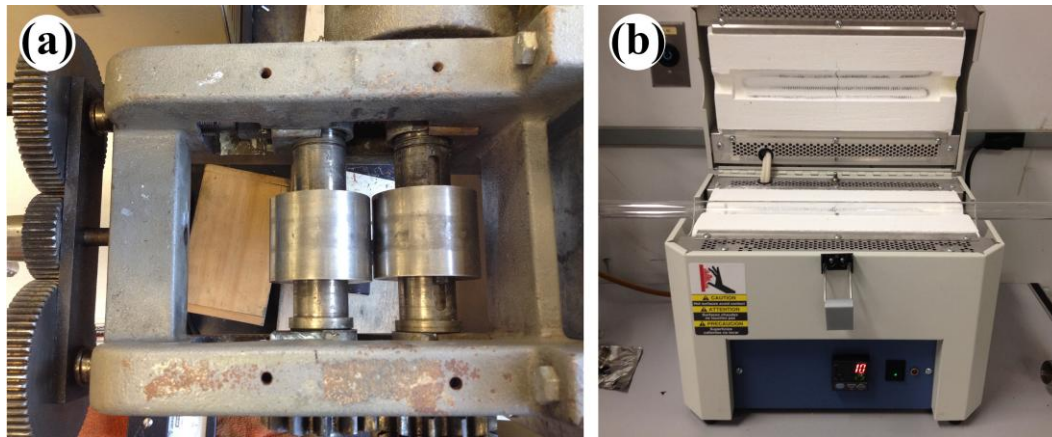


Figure 3.2 (a) Overview of mini rolling machine in lab for sample processing. (b) Overview of vacuum tube furnace to perform necessary annealing.

3.1.3 Multilayered Cu/Cu₁₀Zn laminates

The fabrication of multilayered Cu/Cu₁₀Zn laminates is conducted in Dr. Heinz Werner Höppel's lab, one of our collaborative groups in German. We appreciate their kind assistance with laminate sample preparation by accumulative roll bonding (ARB). The combination of original Cu and Cu₁₀Zn sheets was processed with different cycles of rolling: 2, 3 and 5. For the processing details and specific surface treatment between rolling cycle, please refer their publications pertinent to ARB processing [184,200,201]. In order to produce laminates with remarkable microstructure differences and further enhancing the

bonding strength after ARB, additional annealing treatment under 250°C for 2hrs was performed for all samples in the previously mentioned furnace.

3.2 Mechanical Tests

3.2.1 Uniaxial tension tests

To test the samples' strength and ductility, uniaxial tension tests are conducted on a Shimadzu AGS 20kNG machine with software of both simple tension and cyclic tension programs (as shown in Figure 3.3a). In order to accommodate the specimen dimension in our studies, a specific tension grip (see inset in Figure 3.3a) is house built and incorporated with the facility during tests. The typical mini dog-bone shaped tension samples were machined by a Sherline CNC mill system (8600) with Linux software, as shown in Figure 3.3b. The codes for sample dimensions were individually programmed. One example of such code is attached in final appendix. Post-test analysis is assisted with Matlab program to precisely and objectively determine the uniform elongation, 0.2% offset yield strength and other parameters in mechanics. An example of Matlab code is attached at the end as well.

3.2.2 Micro-hardness tests

Micro-hardness testing is another tool to loosely characterize the mechanical properties of metallic samples and sometimes used to detect the extent of hardening after deformation. The micro-hardness tester for measurement is shown in Figure 3.3c. All samples are mechanically polished to a mirror finish by sandpapers or SiC lapping films. The loadings of the tester are carefully selected to match and facilitate the comparisons across samples.

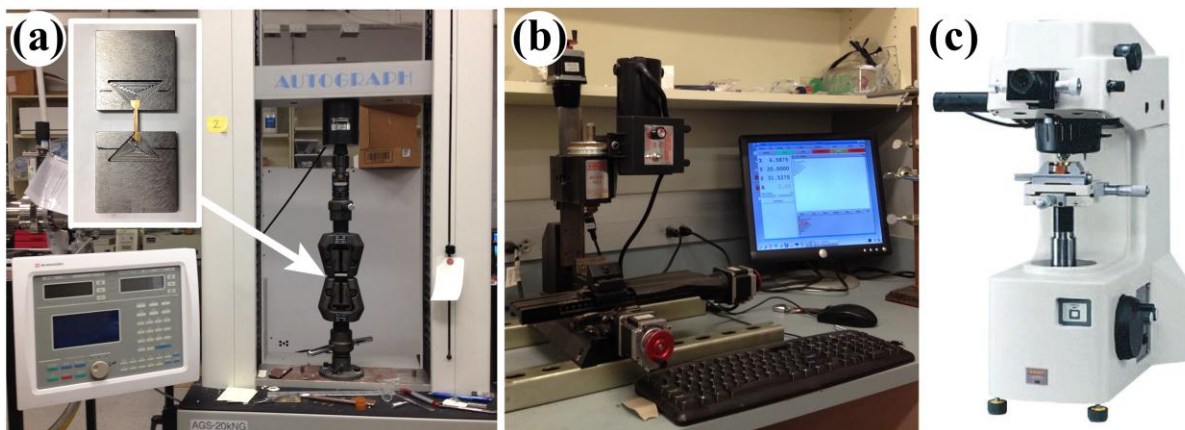


Figure 3.3 Overview of (a) Shimadzu AGS-20kNG uniaxial tension tester. (b) Sherline CNC mill system (8600) to machine the dog-bone shaped tensile specimen. (c) Micro-hardness tester with loading variation from 10g to 200g.

3.3 Transmission Electron Microscopy (TEM)

3.3.1 TEM foil preparation

The TEM samples/foils in our studies are prepared in multiple ways dependent on the original sample geometry, location sensitivity in research. In Chapter 4&5, TEM samples were firstly cut from the every edge of Cu-Zn disk after HPT. The cross-sectional samples were then polished via a MultiPrep™ polishing system from Allied High Tech Inc. (see Figure 3.4a). By using SiC lapping film with different grades, samples are finally polished to a foil with thickness $\sim 30 \mu\text{m}$. Foils were then carefully attached to Φ -3mm Cu or Mo rings by superglue and ion milled by Precision Ion Polishing System (see Figure 3.4b) from Gatan Inc. The milling process was under protection of liquid nitrogen at -50°C to avoid potential grain growth. For Cu-Zn alloys, our recipe for ion mill was 4.0/3.5kV with high angle for

rough mill and 3.0/2.5kV with low angle for fine milling till perforation. The resulted edge regions around the perforation were usually ready for the following observation under TEM.

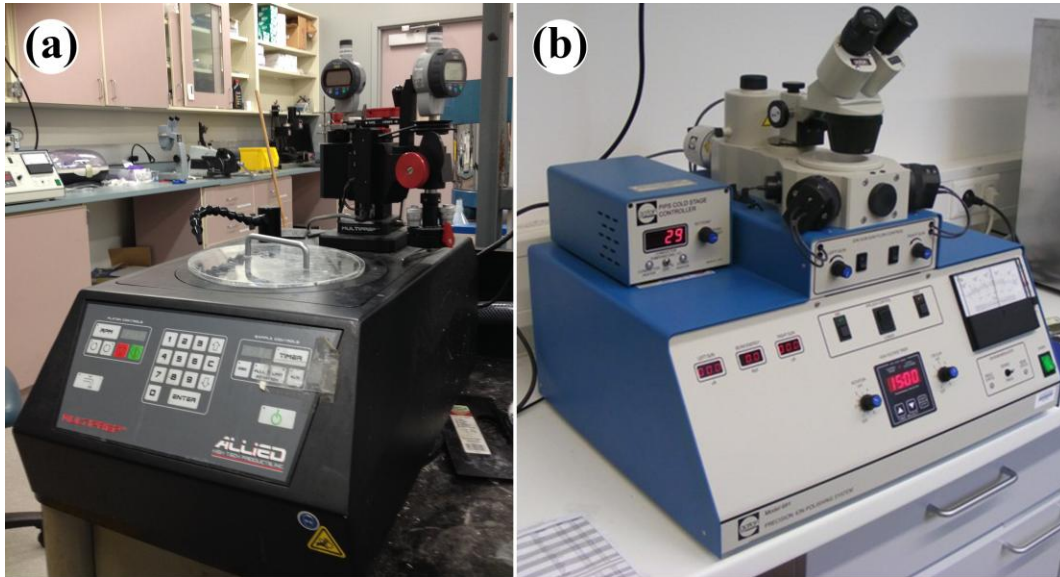


Figure 3.4 Overview of (a) MultiPrep™ system from Allied High Tech. (b) Precision Ion Polishing System (PIPS) from Gatan Inc.

For location sensitive purpose like particular interface in laminate structures, another technique called Focused Ion Beam (FIB) “lift-out” was employed in that case. Mini samples underwent similar grinding and polishing process under MultiPrep™ polishing system and then were mounted in a FEI Quanta 3D FEG dual-beam instrument, as shown in Figure 3.5.

The general procedures for FIB lift-out technique are:

1. Locate the sample region of interest and deposit a thin Pt layer for protection.
2. Bulk milling both sides of the Pt strip.

3. U-shape cuts to the sample to prepare for the lift-out release.
4. Lift out the original sample foil by using the Omni-Probe
5. Attach the original foil to sample grid and do final thinning

The applied voltage and current of Ga^+ vary with proceeding steps. For samples contain specific interface of interest, more cautions are needed to take care of different milling rates of materials across interfaces. Appropriate additional millings are sometime necessary to achieve electron transparent regions for both sides. Cross-sections of sample after bulk milling with low current also provided great chances to image the microstructure by Ion Channeling Contrast Microscopy (ICCM). ICCM under ion-beam mode with lower current facilitates the overview of sample microstructure and enables the recognition of various grain orientations, grain size and other microstructure details.

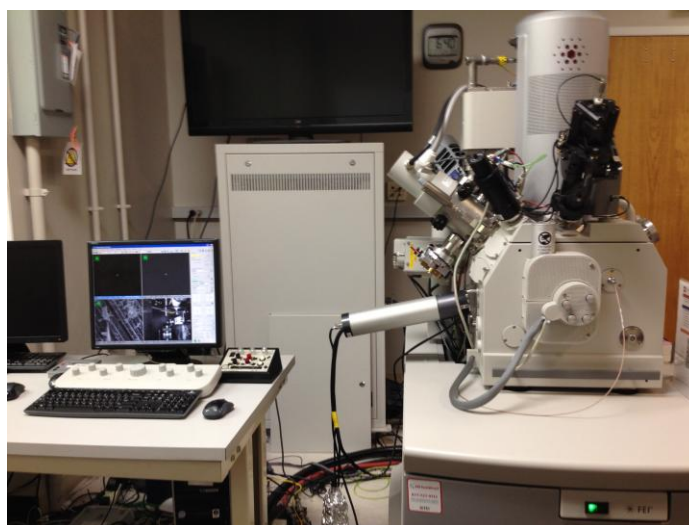


Figure 3.5 Overview of a FEI Quanta 3D FEG dual-beam system for both FIB lift-out technique and EBSD observations

3.3.2 TEM observation

Most TEM work of this dissertation was performed in a JEM-2010F transmission electron microscope operating at 200 kV at room temperature (Figure 3.6a). The high-resolution micrographs were mostly taken along zone axis of $\langle 110 \rangle$ of Cu or Cu-Zn alloys under magnification more than 300k. The high-angle annular dark-field (HAADF) images were taken using an aberration-corrected FEI Titan G2 microscope (see Figure 3.6b) operated under 200 kV. Additionally, the Energy-disperse X-ray Spectroscopy (EDS) mapping was also acquired under this microscope for the region of interests. The microscope is equipped with four large-area silicon drift detector system and a collection solid angle of 0.7 sr for the EDS signal detection, which facilitate resolving elemental identification with a high spatial resolution. The EDS composition was analyzed using the Cliff-Lorimer method in Bruker Esprit software.

3.4 Electron Back-Scattering Diffraction (EBSD) Microscopy

3.4.1 EBSD sample preparation

EBSD samples were prepared using electrochemical polishing plus slight ion mill to clean the surface contamination. The electrolyte recipe of Cu and Cu-Zn alloys for electrochemical polishing is phosphoric acid (concentration of 85%), ethanol and deionized water with volume fraction of 1:1:2. Before electrochemical polishing, samples were carefully mechanically polished by MultiPrepTM system and arrived at a mirror surface. The electrochemical polishing was performed under a simple house-built facility where 301 stainless steel served as the cathode (as shown in Figure 3.7a). It took ~1 min to polish each

sample for each sample to get grid of the most surface with strain. The applied voltage and current were customized dependent on the sample dimension. Samples were then placed into a Fischione Ion Mill instrument (Model 1060, as shown in Figure 3.7b) for further cleaning. Milling process followed the recommended recipe for Cu and Cu alloys is available from the instrument website. (<http://www.fischione.com/model-1060-sem-mill-ion-milling-recipes-bulk-materials>)

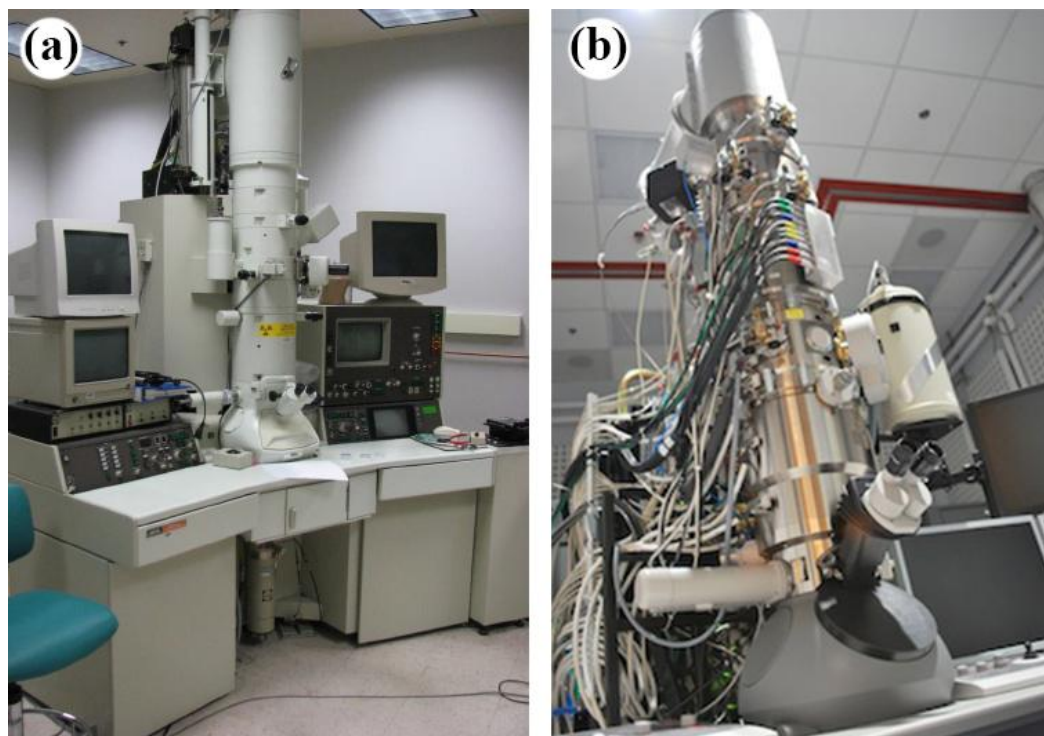


Figure 3.6 Overview of (a) JEM-2010F transmission electron microscope and (b) aberration-corrected FEI Titan G2 microscope

3.4.2 EBSD observation

The EBSD observations were performed in the abovementioned FEI Quanta 3D FEG dual-beam instrument with backscattering electron detectors. The operating software for EBSD tests was Aztec from Oxford instruments Inc. Most EBSD data were acquired under 20 kV and 16nA with appropriate step size and binning mode.

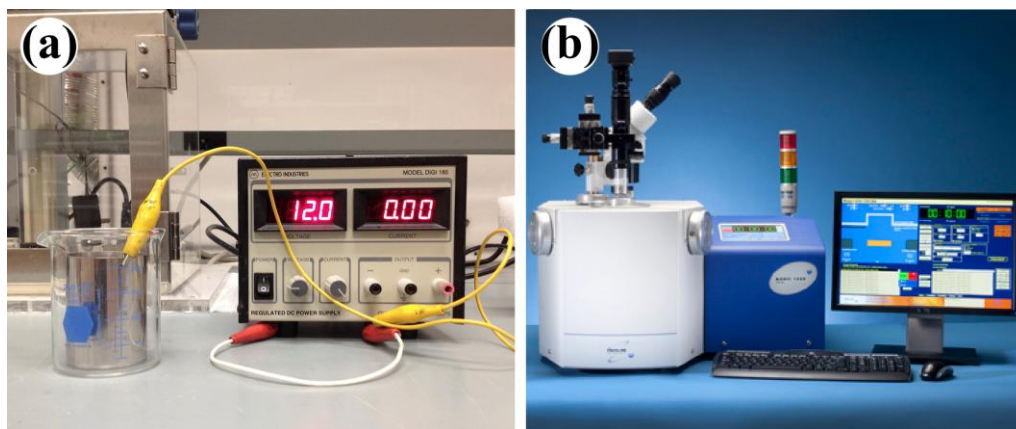


Figure 3.7 Overview of (a) house-built simple electrochemical polishing system (b) Fischione Ion Mill instrument (Model 1060)

Chapter 4

Alloying Effect on Grain-Size Dependent Deformation Twinning in Nanocrystalline Cu-Zn Alloys

Grain-size dependency of deformation twinning has been previously reported in nanocrystalline face-centered-cubic metals, which results in an optimum grain size range for twin formation. In this chapter, for the first time in experiments, the observed optimum grain sizes for deformation twins in nanocrystalline Cu-Zn alloys slightly increase with increasing Zn content. This result agrees with the reported trend but is much weaker than predicted by stacking-fault-energy based models. Our results indicate that alloying changes the relationship between the stacking-fault and twin-fault energy and therefore affects the optimum grain size for deformation twinning. These observations should be also applicable to other alloy systems.

4.1 Introduction

Twinning is a widely observed deformation mode in face-centered cubic (FCC) metals and alloys with nanometer-sized (<100nm) grains, even in metals that usually do not deform by twinning at their coarse-grained state under quasi-static strain rate and room temperature [58,80,100,104,110,135,202]. Twin boundaries are effective in inhibiting dislocation slip and thereby increasing yield strength in a way similar to grain boundaries [203–206]. Meanwhile, twin boundaries are able to interact with dislocations to form steps and serve as dislocation sources for further plastic deformation [41,95,138,207]. In additions,

twin boundaries can also act as effective locations for dislocation accumulation, which increases the strain hardening rate and consequently improves the ductility [90,97,100]. Therefore, deformation twinning has been found one of the most promising strategies to simultaneously enhance strength and ductility in FCC materials.

The benefit of twinning in enhancing mechanical properties makes it a significant issue in science and engineering of FCC nanocrystalline (NC) materials. Extensive studies have revealed that the deformation twinning is influenced by both extrinsic deformation conditions, including strain, strain rate, flow stress and temperature [118,208–211], and intrinsic materials characteristics such as stacking-fault energy, general planar fault energies (GPFE), crystal orientation and grain size [100,105,121,212,213]. Recent experimental investigations have found that twinning propensity first increases then decreases with decreasing grain size in different FCC NC materials, indicating that there exists an optimal grain size window for the formation of deformation twins (d_{op}) [107,116,214,215]. This is important to practical design of nano-materials for superior mechanical properties since this is the grain size window in which the twin structure is most stable [100,116,121].

In the analytical model that predicted the optimal grain size for deformation twinning, stacking-fault energy is one of the most important factors that affect the optimal grain size [125,126]. The model agrees reasonably well with experimental observations in pure FCC metals [100,216]. Generally, the optimal grain size for twinning increases with decreasing stacking-fault energy. The most effective way to change stacking-fault energy is by alloying. However, there have been so far no systematic experimental studies on alloying effect on the optimal grain size for deformation twinning. Recent *ab-initio* simulation on GPFE has

uncovered some salient differences between pure metals and their alloys [217]. For example, the generally accepted relationship in pure FCC metals, γ_{SF} (stacking-fault energy, SFE) $\approx 2\gamma_{twin}$ (twin-fault energy), is no longer valid in their alloys due to the inhomogeneous distribution of solutes [217–219]. In other words, the configuration of grain-size effect on deformation twinning in alloys may differ from the predictions of the reported model.

In this chapter, Cu-Zn alloys were deformed and refined to nanometer grain sizes by high-pressure torsion (HPT). By changing the Zn compositions and deforming under identical conditions, we were able to systematically investigate the effect of alloying on grain-size dependent twinning propensity and the optimal grain size for twinning in NC materials.

4.2 Experimental Method

Commercial Cu-10wt.%Zn, Cu-15wt.%Zn and Cu-30wt.%Zn plates with coarse grains were punched into ϕ -10mm disks, which were subjected to HPT for 6 revolutions with an imposed pressure of 1GPa at 1.5rpm. The grain size distributions were characterized in a JEOL-2010F Transmission Electron Microscope (TEM) operated at 200kV. Statistical analysis of deformation twins was conducted by high-resolution electron microscopy (HREM) observation of at least 170 grains in each sample. All TEM samples were cut from the very edge of as-HPTed disks as this is the region with the greatest degree of grain refinement. Samples were subsequently mechanical polished and ion milled. Theoretical critical stress and the optimal grain size for twinning in each alloy were calculated through previously proposed model based on pure metals, which helps to identify the influence of alloying and establish correlations with experimental results.

4.3 Results and Discussions

Figure 4.1 shows the typical bright-field TEM images and diffraction patterns of three alloys after HPT for 6 revolutions at room temperature. All samples have achieved significant grain refinement to nano-scale compared to raw materials. The simple shear strain at edge of HPT-ed is sufficient enough to make microstructure evolution reach the equilibrium in our samples compared with previous studies [220]. But the microstructure morphologies vary slightly in different alloys. Some elongated grains are present in Cu-10Zn while the major constituent of Cu-30Zn microstructure is equiaxed grain. This is probably ascribed to their various SFEs, which will determine different capabilities of the formation of subgrain boundaries during the deformation and refinement [221,222]. It's worth to note deformation twins are frequently seen in as-processed samples (marked by white arrow in Figure 4.1). Insets are corresponding diffraction patterns. The presence of cluster diffraction spots and rings imply almost random misorientations of grains. Despite the minor discontinuity of diffraction rings, there's no prevailing texture along the observation direction. These results are consistent with previous result of Cu after high strain torsion [220]. Figure 4.1d-f are statistical grain-size distributions in each material, indicating the average grain sizes are 77nm, 53nm and 43nm for Cu-10Zn, Cu-15Zn and Cu-30Zn, respectively. Grain size is determined by geometric mean of its long and short dimensions. The difference among effectiveness of refinement in alloys is related to their SFEs [222–225]. Note that large grain-size range from below 10nm to more than 100nm allow us to perform careful statistical analysis of grain size dependent twinning in each material.

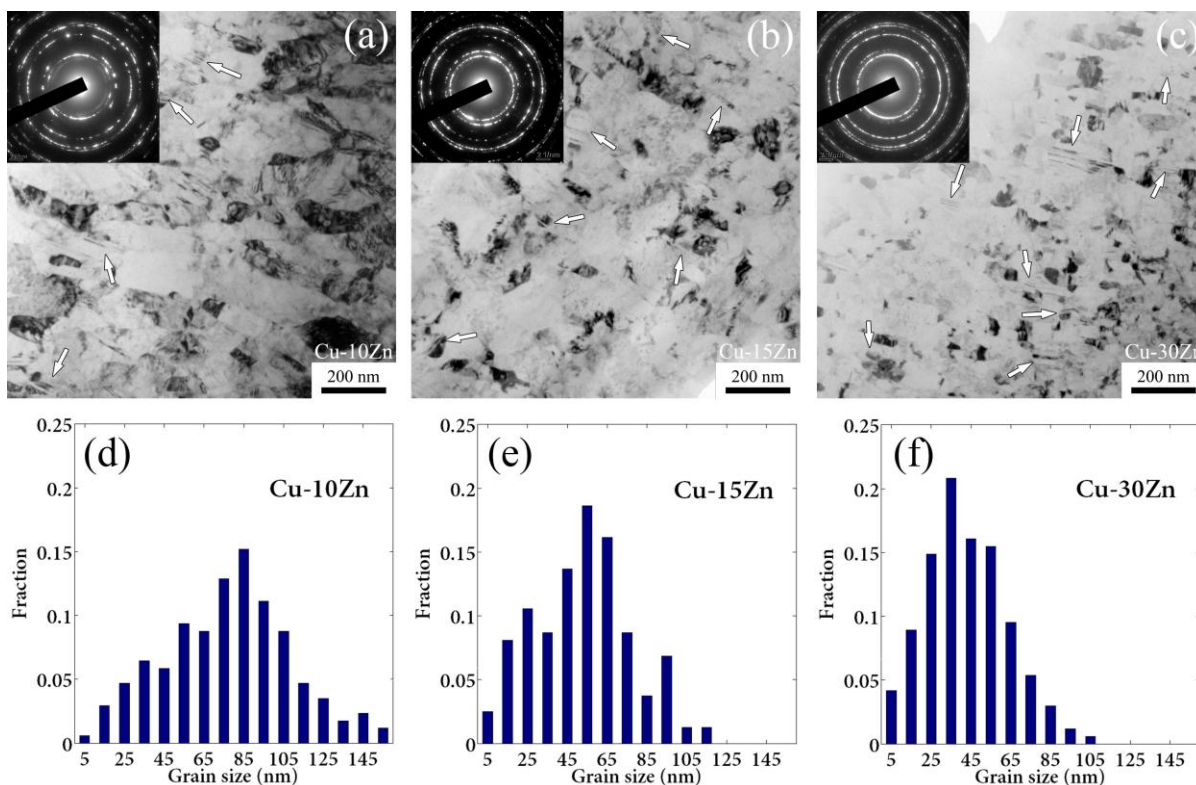


Figure 4.1 Bright-field TEM images of (a) Cu-10Zn, (b) Cu-15Zn and (c) Cu-30Zn show HPT-ed microstructures containing nano-size grains and deformation twins. Insets are corresponding selected area diffraction patterns. Statistical grain size distributions of (d) Cu-10Zn, (e) Cu-15Zn and (f) Cu-30Zn show considerable proportions of nano-grains for statistical analysis.

HREM images in Figure 4.2a-c depict three typical twin morphologies in Cu-Zn alloys, which were counted as deformation twins in statistical analysis. Figure 4.2a shows a deformation twin with both ends terminated at grain boundaries (GBs) (as indicated by white asterisks in the inset), which is typical in NC materials. Non-equilibrium GBs with high energy usually exist in severely deformed NC samples [16,226]. They can serve as sources for partial emissions and promote the nucleation of deformation twins by readily overcoming

the barrier of unstable stacking-fault energy and unstable twin-fault energy [57,100,227,228]. Therefore, the other two important parameters in GPFE curve: SFE (γ_{SF}) and twin-fault energy (γ_{twin}) will dominate the twinning propensity in such scenario [126,229]. Figure 4.2b shows a deformation twin terminated in the grain interior (marked by white dots). Such features appear in these samples and provide evidence for the formation mechanism of partial emission from GB [228], which is the basis for following model analysis. Figure 4.2c illustrates a deformation twin with migrated coherent twin boundary that was formed by interactions with other defects such as Shockley partials. As mentioned in the introduction, twin boundaries can also act as defect source to emit Shockley partials. Figure 4.2d-f demonstrate specific locations (dotted squares) of these three deformation twins at corresponding nano-grains. Note that all of them are bounded by GBs (as marked by asterisks), which is the most frequently observed in this study. This provides the fundamental basis for the semi-quantitative model that will be discussed later. It should also be clarified that not all twin structures in FCC could be revealed on any single $\langle 110 \rangle$ zone axis under HREM because only those with the right orientation can be observed [100]. However, statistical results of deformation twins from large samples are still informative and qualitative comparisons are valid.

Figure 4.3 shows the statistical histogram of randomly observed nano-grains and those with deformation twins, as well as the corresponding fractions of grains with deformation twins versus grain size. In order to keep the consistency of all statistical results, additional precautions are taken to leave out those grains with severely lenticular shape (i.e. long dimension/short dimension >2).

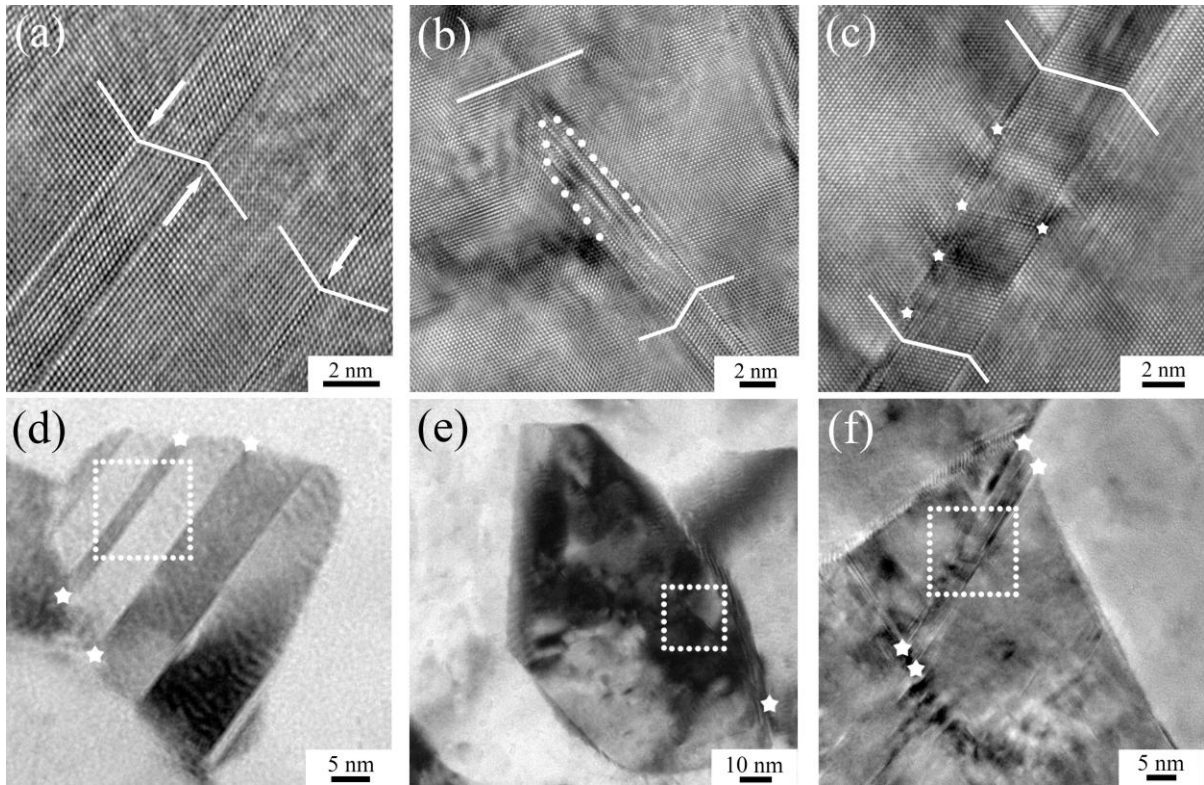


Figure 4.2 Typical twinning morphologies in deformed NC Cu-Zn alloys: (a) Deformation twins across the whole grain. (b) Deformation twin terminated in the grain interior. (c) Deformation twin highly interacted with other defects. Specific locations in corresponding nano-grains are shown in (d)-(f). Note all twins are bounded by GBs, as shown by asterisks.

Table 4.1 Parameters and results in calculations of the model [230,231]

Material	γ_{SF} (mJ/m ²)	a (Å)	G (GPa)	ν	d_{op} (nm)
Cu10Zn	35	3.64	44	0.307	44
Cu15Zn	25	3.65	44	0.307	72
Cu30Zn	14	3.69	40	0.375	144

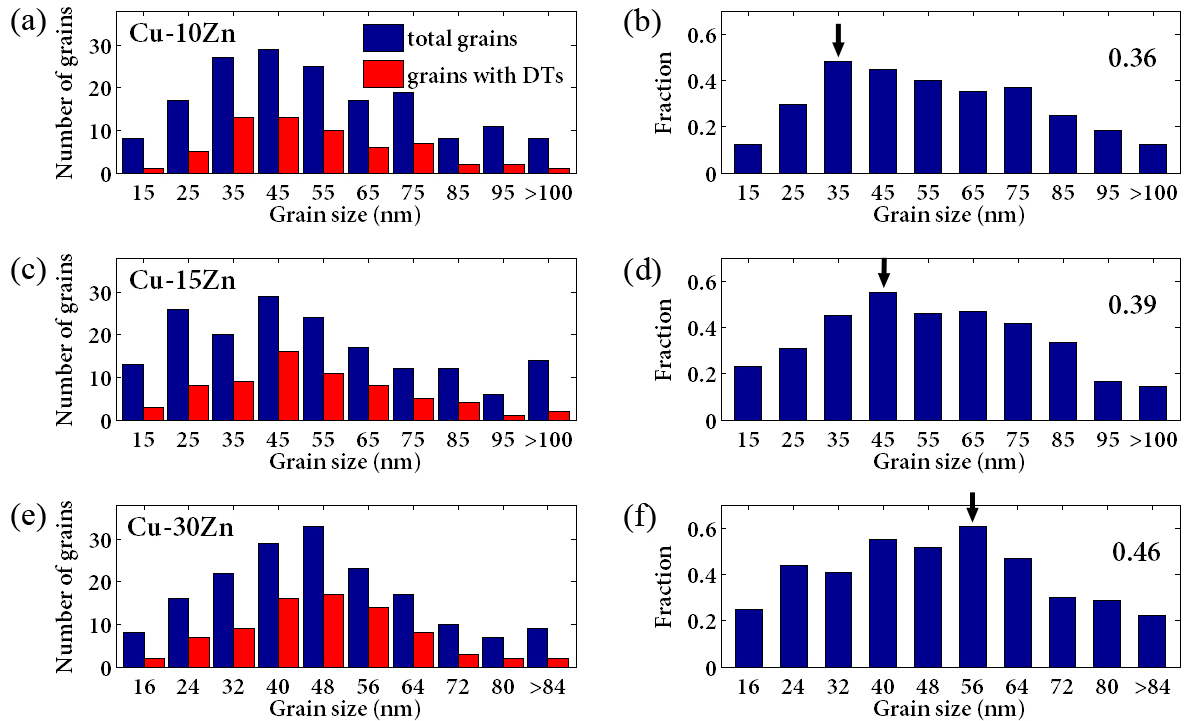


Figure 4.3 Statistical analysis of randomly observed nano-grains and their twinning propensities. Grain-size distributions of all observed grains (blue bar) and those with twins (red bar) in (a) Cu-10Zn, (c) Cu-15Zn, (e) Cu-30Zn. Corresponding fractions of grains with twins in (b) Cu-10Zn, (d) Cu-15Zn, (f) Cu-30Zn, including total fraction (number at top right) and those of each size region (blue bar).

As a result, the total fraction of twinned grains, which can be used as an indicator of twinning propensity, increases (0.36 to 0.46) with increasing Zn content, which is also consistent with GPFE effect on twinning [215,228,229]. Fraction (Figure 4.3b, d, f) plots also indicate a similar trend of the effect of alloying. In all three NC alloys, with decreasing grain size, the twinning propensity first increases and then decreases after certain grain sizes, i.e. there is an optimum grain size d_{op} for twinning for each alloy. The d_{op} for twinning is estimated by the

location of fraction peak (black arrows in Figure 4.3), showing 35nm, 45nm and 56nm for Cu-10Zn, Cu15Zn and Cu-30Zn, respectively. This indicates an increase in d_{op} with increasing Zn content, which has never been systematically reported before.

An analytical model has been developed to analyze the grain size effect on twinning propensity in FCC NC materials [125,126]. This model is based on classical dislocation theory and the assumption that leading Shockley partials are readily emitted from energetic GBs, which agrees with the case in this work. The critical stresses for twin nucleation (τ_{twin}) and trailing partial (τ_{trail}) to remove the first twin partial are expressed as (take screw system as an example [126])

$$\tau_{twin} = \frac{Ga}{2\sqrt{6}\pi d \sin \alpha} \ln \frac{\sqrt{2}d}{a} \quad (4.1)$$

$$\tau_{trail} = \frac{\sqrt{6}}{\cos(\alpha - 30^\circ)} \left[\frac{Ga(8-5\nu)}{48\pi(1-\nu)d} \ln \frac{\sqrt{2}d}{a} - \frac{\gamma_{SF}}{a} \right] \quad (4.2)$$

where G is the shear modulus, ν is the Poisson's ratio, γ_{SF} is the SFE, α is the angle between the applied shear stress and the dislocation line, a is the lattice parameter, d is the grain size. Deformation twins are statistically promoted under the condition of $\tau_{twin} < \tau_{trail}$. Assuming the grains are randomly oriented and the orientation distribution are the same for grains in all size ranges, the optimum grain size for twinning d_{op} can be obtained by solving

$$\frac{d_{op}}{\ln(\sqrt{2}d_{op}/a)} = \frac{9.69 - \nu}{253.66(1-\nu)} \frac{Ga^2}{\gamma_{SF}} \quad (4.3)$$

The parameters used in model calculations are listed in Table 4.1 [230,231]. The comparison between model calculations and the experimental results is summarized in Figure

4.4. It can be concluded that the trend of alloying effect on optimum grain size for deformation twinning (d_{op}) is consistent in models and experimental observations: d_{op} increases with the increase of Zn content. However, experimental results indicate a weaker effect as predicted by calculations. For Cu-30Zn, d_{op} is only around 56nm, which is a much smaller increase than predicted by models (144nm). The mechanisms underneath these two features are elucidated below.

First, increase in solute contents leads to larger optimum grain size for deformation twinning. As indicated in the model, d_{op} is determined when τ_{win} and τ_{trail} are equivalent. It can be inferred from Eq 6.1 and 6.2 that SFE primarily affects τ_{trail} by eliminating the formed stacking fault. Therefore, when SFE is decreased, more stress is required to remove the generated fault, i.e. higher τ_{trail} . In contrast, most other material parameters, like shear modulus, Poisson's ratio and lattice parameter, are similar in the same series of alloys, as seen in Table 4.1. Consequently, as shown in solid plots of Figure 4.5, more solutes in alloys will cause the shift of d_{op} to higher region by decreasing SFE.

Second, the shift of d_{op} is not as severe as speculated by model calculations. We note that the analytical model originates from pure FCC metals. The quoted relation in this analysis is $\gamma_{SF} \approx 2\gamma_{twin}$, which is derived from hard-ball models and applicable to most pure FCC metals [33,234]. In reality, solute atoms are not homogeneously distributed in alloys. They prefer to locally reside near or away to the planar fault, i.e. the well-known Suzuki effect [33,235]. As a result, recent *ab-initio* calculations have revealed that actual alloy systems deviate from this relationship [217,219,236], namely

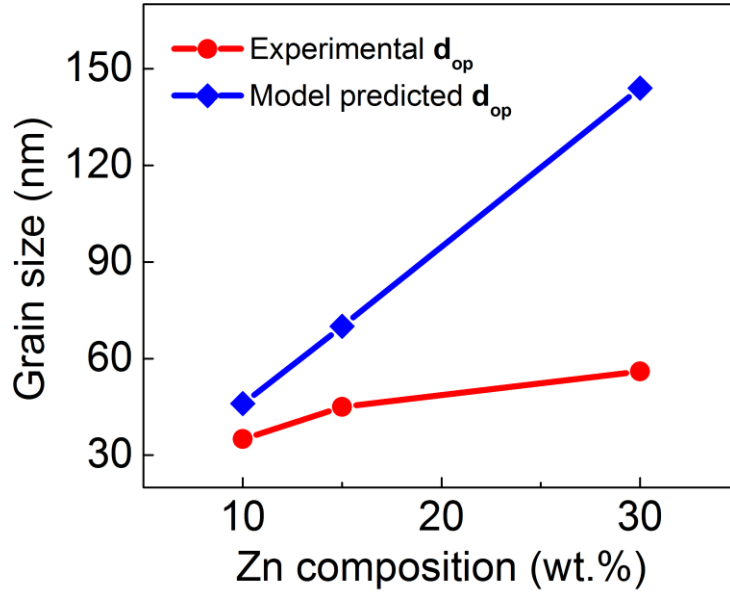


Figure 4.4 Summary of experimental results and model predictions of optimum grain sizes (d_{op}) for deformation twinning in different nanocrystalline Cu-Zn alloys vs. their Zn compositions

$$\gamma_{SF} \neq 2\gamma_{twin} \quad (4.4)$$

For example, $2\gamma_{twin}$ is higher than the intrinsic SFE γ_{SF} when Cu are alloyed with Al atoms [219,237]. In addition, simulations also implicate that this discrepancy becomes more significant with increasing Al composition [236]. For materials in our studies, previous work has indicated the Suzuki segregation is operative even under room temperature in α -brass alloy [238], proving the validity of Eq 4.4 in Cu-Zn alloys here. Therefore, one can envision that the energy barrier to form a deformation twin (two interfaces, i.e. $2\gamma_{twin}$) is not exactly identical to that of erasing a single stacking fault (γ_{SF}), especially for the highly alloyed materials (Cu-30Zn).

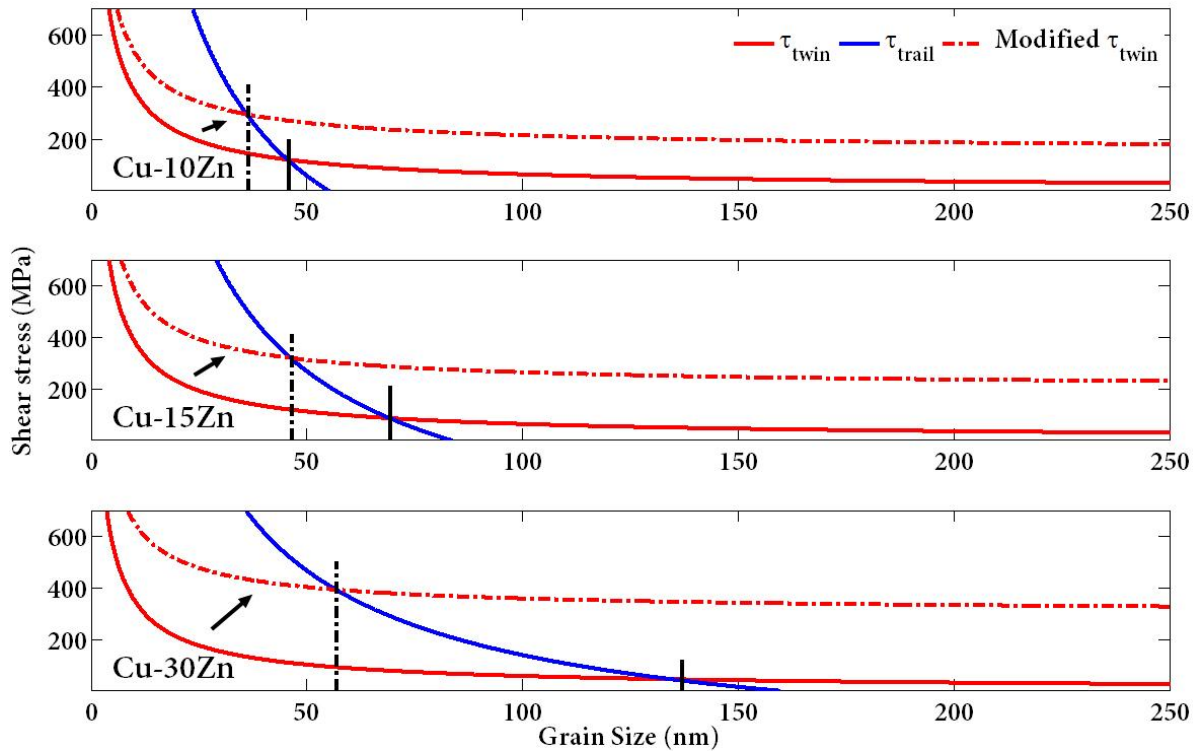


Figure 4.5 Model-based stress calculation (solid lines) of twinning partial (τ_{twin}) and trailing partial (τ_{trail}) and resulted optimum grain sizes (d_{op}) for deformation twinning in Cu-Zn alloys. Dash-dot curves schematically represent the modifications due to the inequality of $\gamma_{SF} \neq 2\gamma_{twin}$ in alloy systems and therefore modified optimum grain sizes d_{op} .

Hence, the abovementioned element-based model requires modifications to incorporate alloying effects. We are currently working on this issue and intend to publish the modified model in the future. Here, we demonstrate a qualitative modification. As schematically presented in the dash-dot plots in Figure 4.5, the change of τ_{twin} curve results in the shift of d_{op} . Based on experimental results, $2\gamma_{twin}$ should be larger than γ_{SF} when Zn is locally segregated around planar fault, i.e. d_{op} shift to small size in each alloy. Since this effect could

be amplified with increasing solute composition due to more chance of preferential and inhomogeneous segregations [236], it is reasonable for Cu₃₀Zn to exhibit maximum deviation of d_{op} from model predictions (see the trend in Figure 4.4-4.5).

4.4 Chapter Conclusion

In summary, deformation-twinning propensities in NC Cu-Zn alloys were systematically studied by HREM. Statistical results reveal a significant grain-size and inverse grain-size effect on twinnability in all alloys, indicating an optimal grain size window for deformation twinning in nano-grains. Also, alloying is found to affect the optimum grain size for twinning, making it deviate from what is predicted by an analytical model developed for pure FCC metals, where the twin boundary energy is assumed to be half of the stacking fault energy. However, in an alloy system, this assumption of energy relationship is no longer valid, which is the primary reason for the observed deviation. These observations should be applicable to other alloys systems.

Chapter 5

Stacking-Fault Energy Effect on Zero-Strain Deformation

Twinning in Nanocrystalline Cu-Zn Alloys

It has been reported that most deformation twins in nanocrystalline face-centered-cubic metals do not produce macroscopic strain. In this chapter, we report the decrease of zero-strain deformation twinning with decreasing stacking-fault energy. One of the two major mechanisms that produce zero-strain twinning is cooperative slip of three partials under external applied stress. Lower stacking-fault energy weakens this mechanism and statistically reduces the fraction of twins with zero-strain.

5.1 Introduction

In conventional coarse-grained metals, deformation twinning is usually accompanied by macroscopic strain [80,100]. This was considered a characteristic of twinning for over half century because all of the conventional twinning mechanisms in coarse-grained materials, including pole, prismatic glide, faulted dipole, etc. require the slips of twinning partials with the same Burgers vector on consecutive slip planes [123,239,240]. As a result, deformation twinning always generates a macroscopic strain. Recently, zero-strain deformation twinning has been widely found in nanocrystalline (NC) face-centered-cubic (FCC) metals and alloys and even in a few coarse-grained materials [130–132,140,202,241]. Zero-strain twins are generated via twinning partials with different Burgers vectors, whose sum is zero [100]. They could affect the mechanical behavior and microstructural evolution of NC metals. For

example, instead of locally accumulating macroscopic strain in twinned grains, zero-strain twins participate in plastic deformation by re-orienting the lattice without producing jagged GBs, which makes it easy for grains to rotate and slide during further deformation [130]. Another salient feature of zero-strain twins is the easy migration of incoherent twin boundaries (ITBs) under slight external stress [139,140]. This feature is believed to play a critical role in strain softening [138,207].

Two major mechanisms have been proposed for deformation twinning with zero-strain in NC FCC metals. Wu et al. proposed that random activation of partials (RAP) was the mechanism for their observation of zero-strain twins in severely deformed NC metals such as Ni, Cu and Al [130,228]. It was hypothesized that Shockley partials were individually activated on neighboring slip planes. Due to the random nature of the partials, the sum of their Burgers vectors is close to zero. Experimental observations and molecular dynamics simulations revealed another important mechanism, named as cooperative slip of three partials (CSTP), which generates a twin by cooperative slip of three different partials on three adjacent planes [139–141,242], where $\mathbf{b}_1 + \mathbf{b}_2 + \mathbf{b}_3 = \mathbf{0}$. The twin propagates through the movement of the $\sum 3\{112\}$ ITBs controlled by the stress balance between each set of three partials, which is simply called the “move-drag” mechanism. Specifically, one or two partials are driven by applied stress while the rest is dragged along due to the stacking-fault energy (SFE) and/or twin fault energy. Both mechanisms were found to play a significant role in zero-strain twinning in NC Cu, which has medium stacking fault energy [202].

In the CSTP mechanism, SFE is assumed to play a critical role while the RAP mechanism is not affected much. However, their comprehensive influence on zero-strain

twinning has not been experimentally investigated. The objective of this study is to systematically investigate the SFE effect on zero-strain twinning and the underlying mechanism. Alloying is an effective approach to change SFE [243]. Cu-Zn alloys are selected for this study.

5.2 Experimental Method

Commercial Cu-10wt.%Zn, Cu-15wt.%Zn and Cu-30wt.%Zn plates were punched into ϕ -10mm disks, which were subjected to HPT for 6 revolutions under the same pressure of 1 GPa at 1.5 rpm. Transmission Electron Microscopy (TEM) foils were made from the very edge of the HPT-processed disks. Each TEM foil was ion milled under the protection of liquid nitrogen. The temperature was set at -100°C to prevent potential grain growth. Statistical analysis of macroscopic strains and thicknesses of deformation twins was conducted by high-resolution transmission electron microscopy (HRTEM) observation of at least 170 grains in each sample. The average grain size is 40~50nm for all samples [244]. Vickers micro-hardness tests were performed to estimate the applied stress in each sample.

5.3 Results and Discussions

The morphology of a grain boundary (GB) segment intercepted by a deformation twin is a good indicator on whether a twin produces strain [100]. Smooth GB implies a net zero macroscopic strain and vice versa. A few other factors including GB shuffling and free volume migration may also affect the GB smoothness. However, assuming those factors affect the GB smoothness in an unbiased way, they do not hinder our statistical study here.

Figure 5.1 shows typical structures of GBs intercepted by deformation twins. GBs with kinks correspond to twins that produce macroscopic strain, while those without kinks correspond to zero-strain twins. Figures 5.1a-c clearly show grain-boundary kinks in three Cu-Zn alloys (marked by dots and arrows). The various kink angles depend on both the view orientations under TEM and sum of Burgers vectors for the partials that contribute to the twin formation [100]. As seen in Figures 5.1d-f, zero-strain twins are also observed in all NC alloys, which are consistent with early reports [131,132,202].

Statistical analysis shows the fractions of twins with strain and zero-strain twins in Figure 5.2a. As shown, zero-strain twins outnumber twins with strain in the Cu-10Zn sample whereas the opposite is true in the Cu-30Zn sample. In other words, the fraction of zero-strain twins is reduced in the low-SFE NC Cu-30Zn alloy (Figure 5.2b).

For those zero-strain deformation twins, their ITBs terminated in the grain interior indicate how they were generated [135,139,141]. The CSTP mechanism is operated by cooperative slip of three partials (\mathbf{b}_1 , \mathbf{b}_2 and \mathbf{b}_3) on three slip planes. This feature gives rise to $\Sigma 3\{112\}$ ITBs with periodic atomic structures, as shown in Figure 5.3a. In contrast, another kind of ITB is shown in Figure 5.3b. This ITB is not periodic in atomic structure, which is probably generated by the RAP mechanism because RAP randomly generates the partials. Analysis of such ITB structures is helpful to understand the fundamentals of how intrinsic properties and extrinsic conditions affect the formation of zero-strain twins.

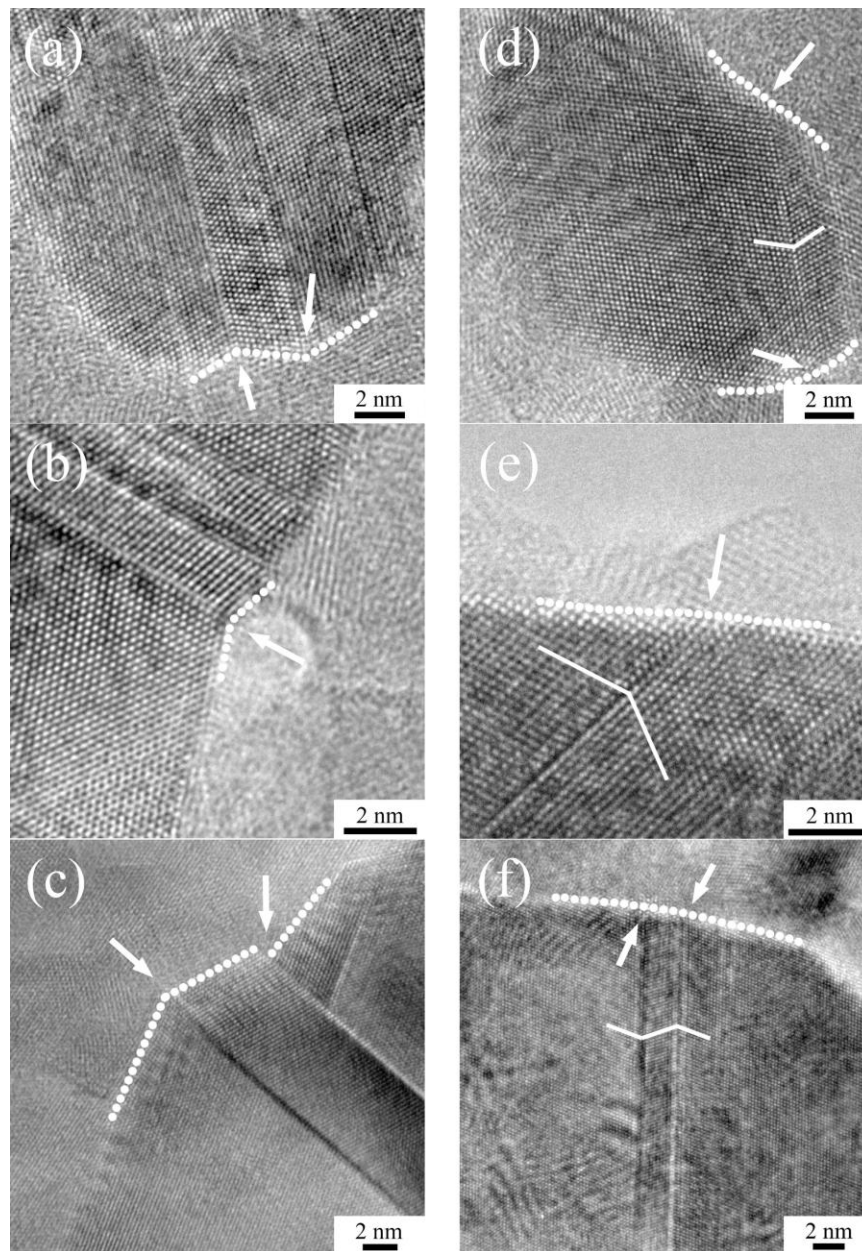


Figure 5.1 Typical high-resolution TEM images of deformation twins with macroscopic strains in NC (a) Cu-10Zn, (b) Cu-15Zn, (c) Cu-30Zn and zero-strain twins in (d) Cu-10Zn, (e) Cu-15Zn, (f) Cu-30Zn. Solid lines mark the matrix-twin relationships. The twin-GB interceptions are highlighted to indicate the macroscopic strain or the lack of it.

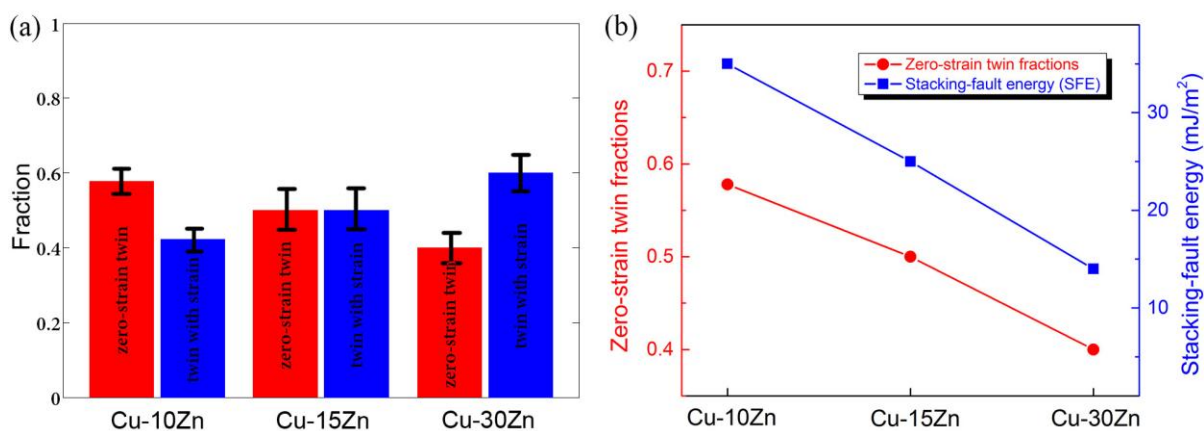


Figure 5.2 (a) Fraction of zero-strain deformation twins in each Cu-Zn alloy. Red bars stands for fraction of zero-strain twins and blue bars stands for twins with macroscopic strain. (b) Fractions of zero-strain deformation twins and stacking-fault energy (blue) in Cu-Zn alloys.

Figures 5.3c-e are HRTEM images of ITBs with the CSTP feature in Cu-10Zn. Such features are also present in other two alloys. During the twin propagation, $\Sigma 3\{112\}$ ITB is split and a periodic atomic sequence is generated due to the local stress balance [242], which is identified by the extra spots in corresponding fast Fourier transforms (FFT) (inset of Figure 5.3e) compared to typical FCC $\langle 110 \rangle$ pattern. By carefully locating the exact ITBs (marked by dotted lines), we measured the split length and found that it varies from twin to twin. When free of local stress, the near-equilibrium length should not be too different from that of pure Cu, which is 0.8nm [131,139]. This is consistent with what is shown in Figure 5.3c with a split length of only 0.88nm. However, this split length is susceptible to local stress fluctuation. Much longer split length such as 3.7 nm and 18.3 nm are shown in Figures 5.3d-e. It's noteworthy that 18.3 nm is much longer than previous observations [131,140] in Cu

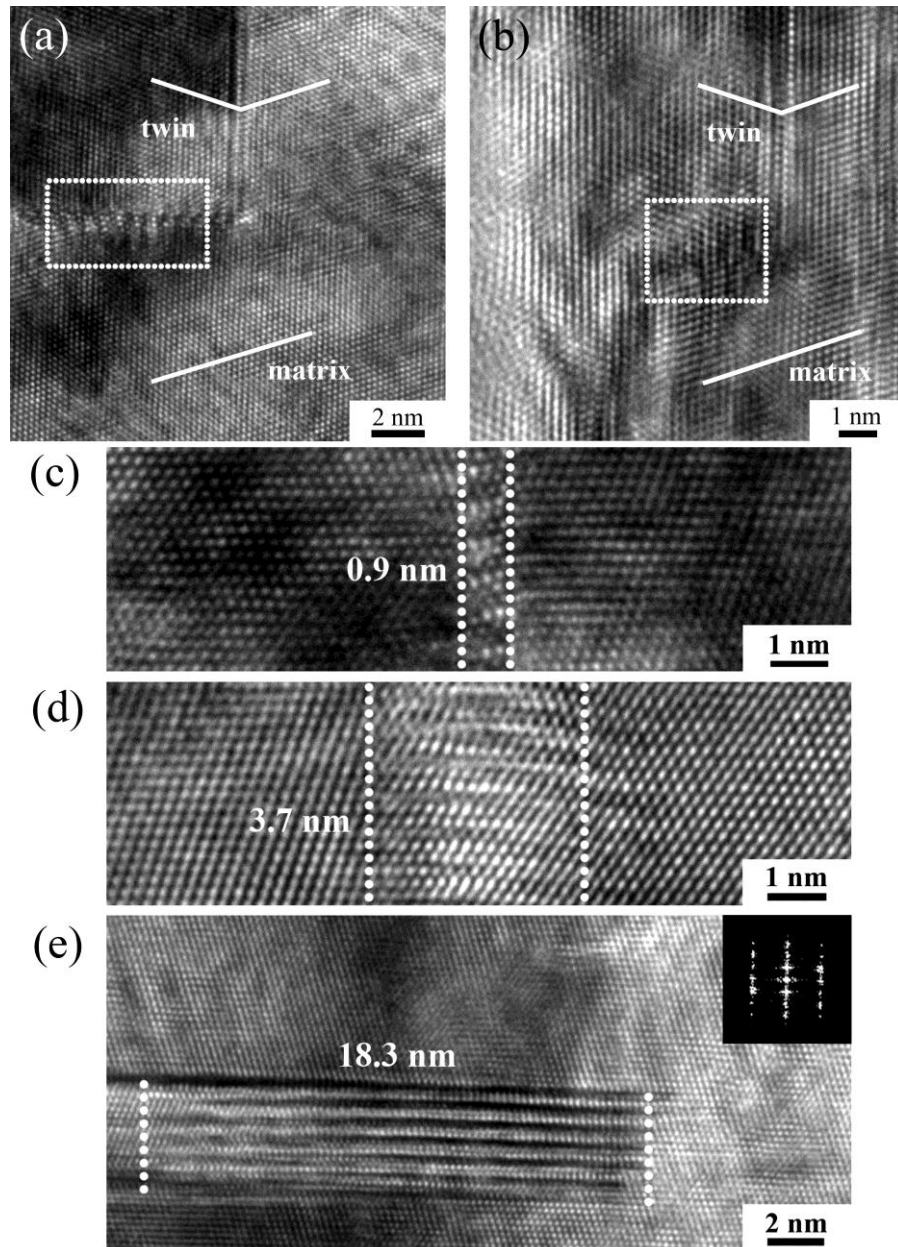


Figure 5.3 Typical atomic morphology of ITBs of zero-strain twins in the Cu-10Zn alloy: (a) with periodicity: $\Sigma 3\{112\}$ ITB, (b) without periodicity. Split of $\Sigma 3\{112\}$ ITBs under (a) near zero stress to (b, c) lower residual stress under equilibrium states in as-deformed nano-grains. Inset in (c) is FFT pattern for the extended ITB, confirming the existence of periodic structure by extra spots.

alloys and may represent an extreme case. More importantly, such evidence is a strong clue to even more extreme cases: breakdowns of ITB equilibrium. This is a reasonable hypothesis in our samples during severe plastic deformation, which is also verified by applied stress estimation later.

Figures 5.4a-c are schematic illustrations of the breakdown process of $\Sigma 3\{112\}$ ITB, a possible mechanism to explain the shrinkage of zero-strain twin proportion in low-SFE samples. At stage A, energetic GBs of nano-grains caused by severe plastic deformation nucleate a twin readily and a temporary near-equilibrium ITB is generated at the twin front. The unstable SFE, another critical factor to partial nucleation, doesn't affect this process much because the non-equilibrium GBs contain dissociated dislocations already [226]. Stage B depicts the stable propagation of this twin frontier under appropriate external stress. During this stage, one or two partials (taking \mathbf{b}_1 for example and hereafter named as leading partial) moved ahead to propagate the twin. There are two major constraint forces against the separation of this leading partial from the other two: interaction between dislocations with different Burgers vectors and the SFE. Obviously, the longer the split length of ITB is, the weaker the attraction is from the other two partials. Therefore, stacking fault constraint (blue lines) plays a more important role in balancing ITB as the split length becomes larger. Lower SFE will decrease the mutual constraint within each tri-layer and may destroy the stress quasi-equilibrium. In addition, if the grain size is reduced to nano scale and comparable to the split length, it'll open up more possibilities for the breakdown of ITB equilibrium. As a result, leading partial has more chance to independently extend and be absorbed by the opposite GB before the other two partials catch up. The other two partials will be prevented

from gliding by local stress and leave a periodic structure at GB, which is composed of the same partial on every three atomic planes, shown in Figure 5.4c. The ITB equilibrium breaks down and the original zero-strain twinning nucleus disappears. This hypothesis is consistent with observations of such debris of periodic structure terminated at GB in the Cu-10Zn sample (shown in Figure 5.4d). Lower magnified inset of the GB indicates the generation of macroscopic strain as expected. Figure 5.4e is the FFT of the selected region in Figure 5.4d, further confirming the same periodic structure in Figure 5.3e. The final structure of this process may not be exactly the same as stage C because extended leading partial may interact with other existing defects on the way [41]. Lower SFE makes this “move-drag” propagation less favorable and statistically reduces the proportion of zero-strain twins, as shown in Figure 5.2. On the other hand, even for the lowest SFE in Cu-30Zn, there’s still considerable proportion of zero-strain twins during deformation. It seems SFE doesn’t affect the proportion so “significantly” in Figure 5.2. This is reasonable because lower SFE only influences CSTP mechanism while RAP is still free to operate in NC materials and generate zero-strain twins [202].

Note that there is possible segregation of Zn solute atoms to the GBs and stacking faults, which may be affected by the Zn concentration. If Zn segregation significantly affects the nucleation of ITB’s or its migration, the effect should be similar for both the RAP and CSTP mechanisms. The experimental observation that the CSTP mechanism is suppressed while the RAP mechanism is not suggests that the effect of the solute segregation is less significant than the SFE effect.

Another concern is whether applied stress is sufficient to activate CSTP mechanism

in our experiments. Although the net force exerted on propagating ITB is nearly zero, it still needs a threshold shear stress to start the “move-drag” process [139,245]. Logically, the threshold driving shear stress for CSTP in Cu-Zn alloys should be lower than that in Cu (~100MPa) [245] since their SFEs are lower and probably comparable to that of Ag (<100MPa) [140]. The applied shear stress is estimated from Vicker hardness (Table 5.1), which is calculated by dividing hardness value by an empirical coefficient [246] and Taylor factor for FCC. The applied shear stresses are ~300MPa in the Cu-Zn NC alloys, which are sufficient to initiate CSTP in all samples. In addition, recent study also indicates that thinner twins with thickness of a few nanometers will promote the CSTP mechanism because they have more excess energies [138]. Statistics of twin lamella thickness in observed twins are listed in Table 5.1. Clearly, average twin thickness in all materials are 3~4nm with only a slight change.

Table 5.1 Experimental applied shear stress, stacking-fault energy, observed average twin thickness in NC Cu-Zn alloys [33,140,230,245]

Materials	Cu10Zn	Cu15Zn	Cu30Zn	Cu	Ag
SFE (mJ/m ²)	35	25	14	45	16
Stress (MPa)	Applied shear stress			Stress to initiate CSTP	
	275	291	334	~100	<100
Twin thickness	4.1	3.7	3.1		

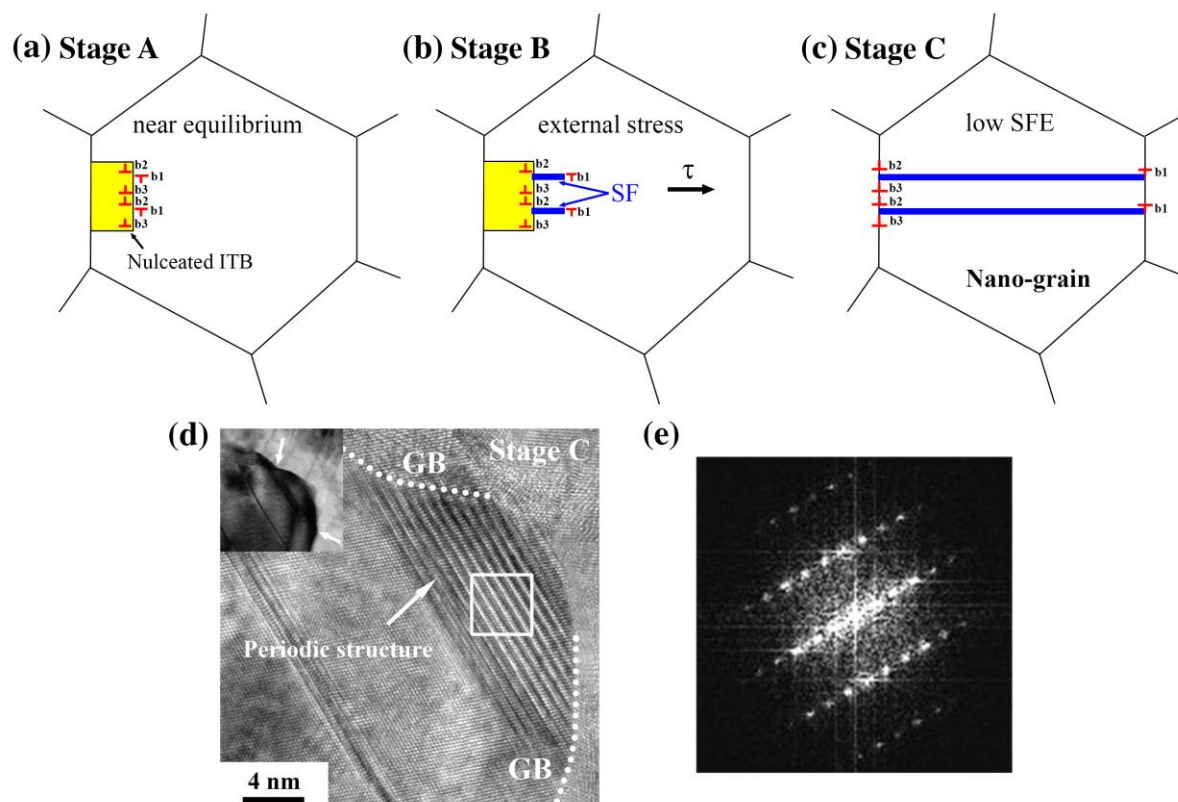


Figure 5.4 (a-c) Schematic illustration of breakdown process of $\Sigma 3 \{112\}$ ITB in nano-grain FCC materials with low SFE. (d) HRTEM observation of periodic structure at GB in the Cu-10Zn alloy. Inset is the low magnified GB image to show the macroscopic strain. (e) FFT result of the selected region in (d), showing the same pattern in Figure 5.3e.

5.4 Chapter Conclusion

In summary, lower SFE will decrease the fraction of zero-strain twins. This observation is attributed to the weakening of the CSTP mechanism for zero-strain deformation twinning based on observation of atomic structures of ITB. Lower SFE has statistically more chance to induce the breakdown of stress balance between partials, which deactivates CSTP mechanism and therefore leads to lower fraction of zero-strain twins.

Chapter 6

Strain Hardening and Ductility in a Coarse-Grain/Nanostructure Laminate Material

A laminate structure with a nanostructured Cu-10Zn layer sandwiched between two coarse-grained Cu layers was produced by high-pressure torsion, rolling and annealing. Sharp interlayer interfaces were developed and remained safe during uniform tensile deformation. Mechanical incompatibility between the different layers during plastic deformation produced high strain hardening, which led to a tensile ductility that is higher than prediction by the rule-of-mixture. These observations provide insight into the architectural design and deformation studies of materials with gradient and laminate structures.

6.1 Introduction

Gradient structures (GS) with a grain-size gradient have been recently introduced to structural materials to optimize their mechanical properties with low cost [75,147,198,247,248]. To date, some exceptional combination of enhanced strength and considerable ductility are reported in different material systems with multiscale grain-size structures [89,194,196,249], including GS and multi-layered materials. However, the fundamental principles that govern the deformation behaviors of GS are still not fully understood [75,147]. Elastic/plastic interface and stable/unstable interface caused by mechanical incompatibility during deformation have been reported to play a critical role in

both strengthening and strain hardening of GS materials [147,198]. However, such interfaces migrate dynamically during the deformation of GS, which makes it hard to perform quantitative postmortem investigation [75,148,198]. In fact, GS can be approximately regarded as the integration of numerous layers and interfaces (laminated structure) [198]. Therefore, there are some similarities in the deformation behaviors of GS structures and laminated structures. For example, both structures have the mechanical incompatibility during the deformation. The advantage of the latter is that its interfaces are stationary [160] and can be easily located after the deformation, making it easier to analyze quantitative mechanics and investigate postmortem microstructures. Therefore, it might be possible to use laminated (or sandwiched) structures to study some fundamentals in deformation behaviors of GS structure.

The fabrication of laminated nanostructured (NS)/coarse-grained (CG) structures with sharp interfaces is also a challenge since interfacial strength and selective grain refinement are required simultaneously. Here, we fabricated a laminated structure with a NS bronze layer sandwiched between two CG copper layers by utilizing two principles: (a) different grain refinement effectiveness of Cu and bronze during deformation. It has been shown that the grain size of bronze can be refined much more effectively than that of copper during severe plastic deformation due to its lower stacking-fault energy [96]. (b) Different thermal stabilities of Cu and bronze. Alloying elements are generally effective in pinning grain boundaries and resisting grain growth [250]. Hence, bronze can remain much finer grain size compared to Cu after proper annealing. Using this approach, we can produce a laminated structure with sharp and well-bonded NS/CG interfaces. Another objective of this work is to

use NS/CG sandwich to study the effect of grain-size-difference across the interfaces on mechanical behaviors.

6.2 Experimental Methods

Figure 6.1a schematically illustrates the procedure of sample processing. Commercial Cu (99.9 wt.%) and bronze (Cu-10 wt.%Zn) plates were punched into ϕ -10mm disks and polished to 3 groups of thickness. The total initial thickness of three disks was around 3.5 mm so that sufficient thickness reduction (~83%) after processing can be achieved to form strong interfacial bonding (thickness reduction history as show in Fig 6.1a). Mechanical polishing and ultrasonic cleaning were carried out before sandwiching the disks together. High pressure torsion (HPT) was applied at room temperature with imposed pressure of 1 GPa for 10 revolutions at 1.5 rpm in order to obtain more homogeneous deformation along the radius direction [251]. Thereafter, as-HPTed sandwiches were rolled to thickness of 0.6 mm from 1.2 mm and then annealed at 240 °C for 2 hours.

Microstructures near interfaces were characterized by FEI Quanta 3D FEG with Ion Channeling Contrast Microscopy (ICCM), JEOL-2010F Transmission Electron Microscopy (TEM) operated at 200 kV and Electron Dispersive X-ray Spectroscopy (EDS) mapping in FEI Titan 80-300. Dog-bone shaped samples with gauge dimension of $0.6 \times 2 \times 8.4 \text{ mm}^3$ were cut from the middle of sandwiches and mechanically tested under uniaxial tension at a strain rate of $9 \times 10^{-4} \text{ s}^{-1}$. Scanning electron microscopy was used to examine fracture surface and interface.

6.3 Results and Discussions

Three groups of samples with varying volume fraction of central NS Cu-10Zn layer (Sample A: 0.10, Sample B: 0.22, Sample C: 0.47) were fabricated. Fig 6.1b shows a typical optical micrograph (cross-sectional view) of Sample C. Different color contrast clearly indicates three layers with two sharp interfaces. As shown in Fig 6.1c, microhardness within each layer is rather homogeneous, while there are abrupt transitions at the interfaces, indicating that the central NS layer has a yield strength over twice of that of the CG Cu layers. These hardness levels in each layer are also representative in all samples in spite of various volume fractions.

Fig 6.2a is a channeling contrast image showing the typical microstructures near the interface. On the left side is typical CG Cu with grain size of $\sim 4 \mu\text{m}$, while on the right side is NS bronze with grain (sub-grain) size of $\sim 100 \text{ nm}$. Magnified image of the NS/CG interface is shown in Fig 6.2b, which reveals a void-free transition from NS bronze to CG Cu. The exact Cu/bronze interface is hard to tell in TEM and can be identified by EDS mapping. Fig 6.2c is a typical high-angle annular dark-field (HAADF) image including a Cu/bronze interface, whose precise location is unknown. EDS mappings in Fig 6.2d and 6.2e show the elemental distribution of Cu and Zn and resolve the exact interface (marked by dotted lines) in Fig 6.2c. Concentrations of Zn are measured as 0.64 wt% in left side and 10.22 wt% in right side, respectively. This agreement of specific composition in Cu and bronze implies no significant bulk diffusion from each side during the processing. Therefore, Fig 6.2c-e confirm the generation of well-bonded and sharp Cu/bronze interface.

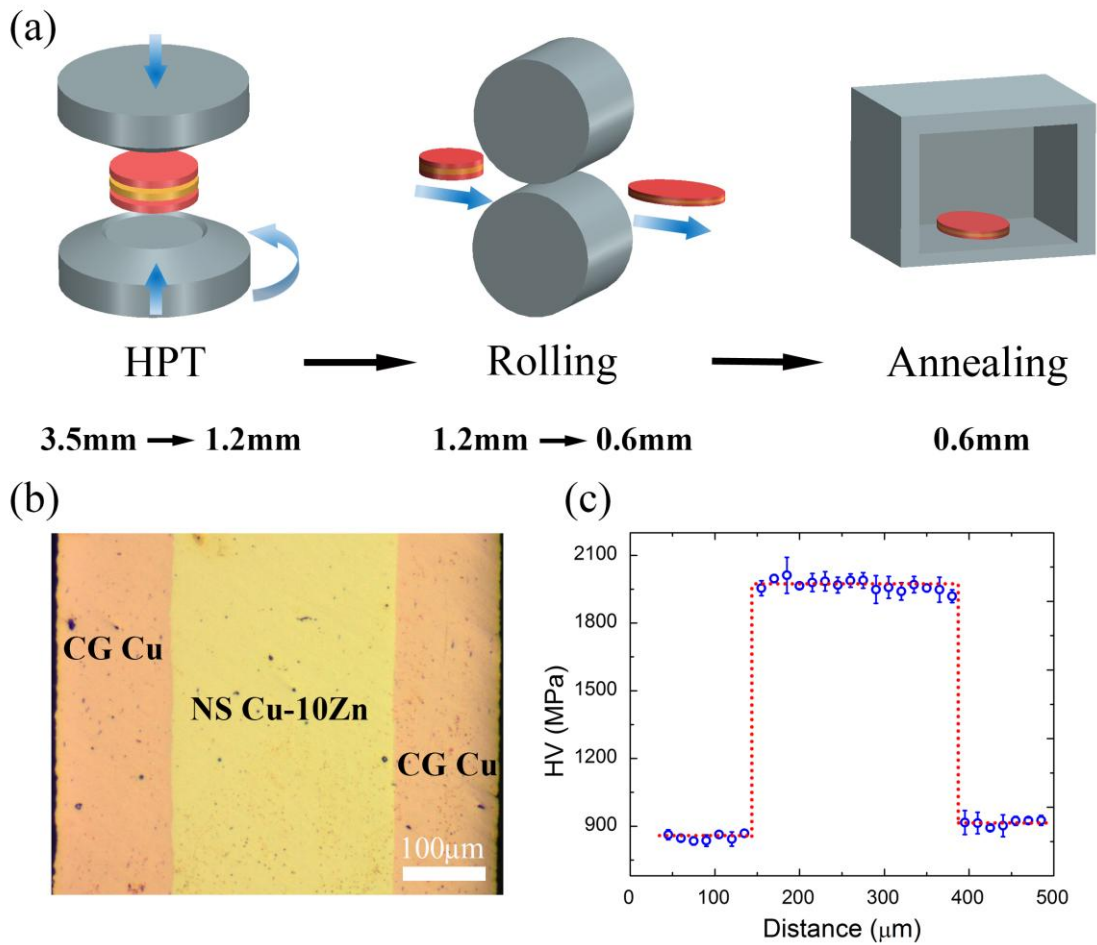


Figure 6.1 (a) Schematic illustration of major procedures to fabricate CG/NS/CG sandwich materials. Deformation history of thickness reduction is also provided below the corresponding step. (b) Optical microscopy observation of as-processed sandwiches with NS Cu-10Zn volume fraction 0.47. (c) Vickers Micro-hardness indentation (with loading 25g) on cross-sectional sample in (b).

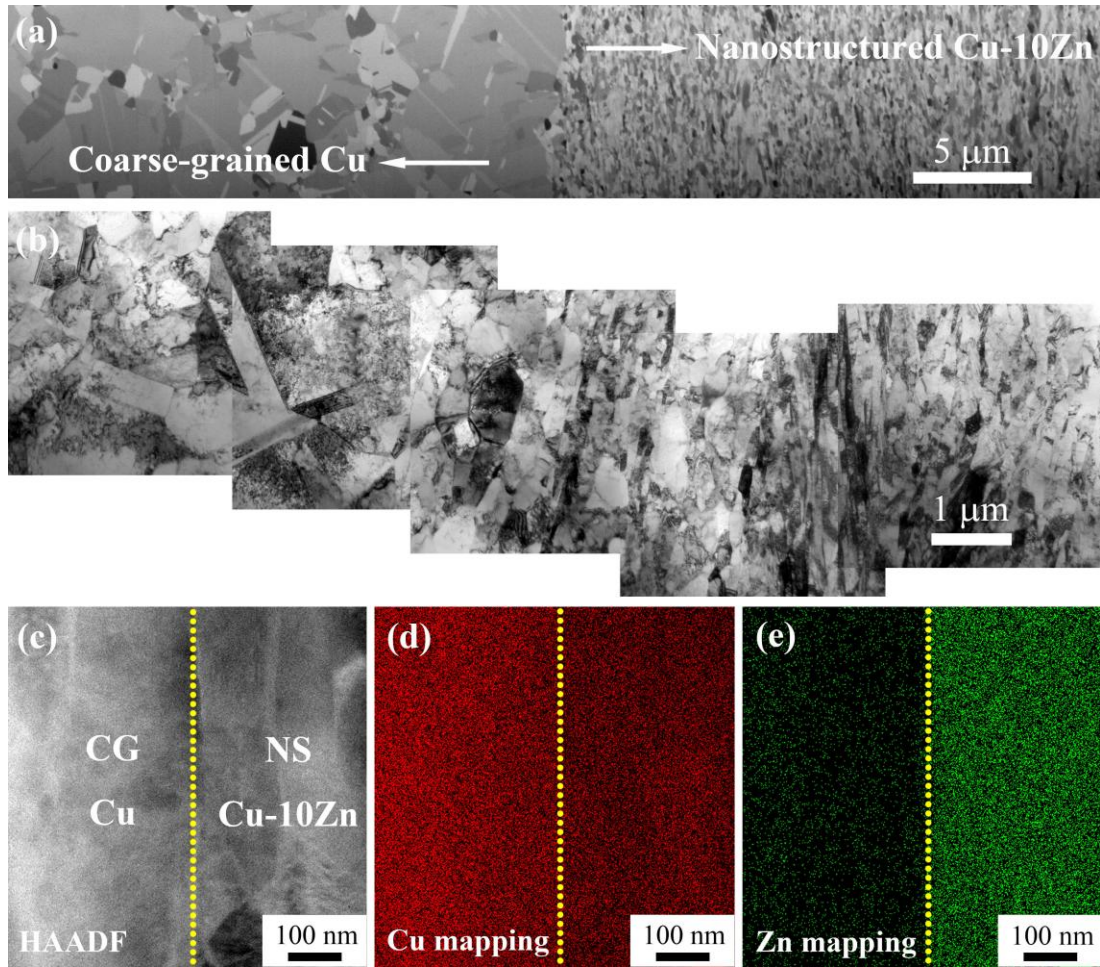


Figure 6.2 (a) ICCM of a typical NS/CG interface in sandwich (70° tilt of sample while imaging). (b) TEM observation of as-processed interface. (c) HAADF imaging of an enlarged area around Cu/Cu-10Zn interface by STEM. EDS mapping of (d) Cu and (e) Zn in corresponding regions in (c).

Fig 6.3a shows the tensile stress-strain curves of laminated samples, pure CG Cu and NS bronze samples. Pure samples were made from the sandwiches by polishing off other layers. The yield strengths (0.2%-strain offset stress) for samples A, B and C were measured as 142 MPa, 201 MPa and 266 MPa, respectively, while their uniform elongation (engineering strain) were 27.1%, 19.6% and 12.3%, respectively. The yield strength of the

laminated sample increases and its tensile ductility decreases with increasing volume fraction of central NS bronze layer. Note that the uniform plastic deformation of NS bronze layer in sandwich is much higher (>12%) than that (~0.7%) of its pure counterpart. This is because its early necking tendency was constrained by the stable CG Cu layers from both sides via the two interfaces.

In conventional theory of rule of mixture (ROM) for laminated composite structure, yield strength (σ_{ys}), strain hardening ($d\sigma/d\varepsilon$) and uniform elongation (ε_{UE}) (true strain) can be expressed as [2, 16, 17]

$$\sigma_{ys} = \sum V_i \sigma'_{i,ys} \quad (6.1)$$

$$\frac{d\sigma}{d\varepsilon} = \sum V_i \frac{d\sigma_i}{d\varepsilon} \quad (6.2)$$

$$\varepsilon_{UE} = \frac{\sum V_i \sigma_{i,UE} \varepsilon_{i,UE}}{\sum V_i \sigma_{i,UE}} \quad (6.3)$$

where V_i is the volume fraction of component i , $\sigma'_{i,ys}$ is the flow stress of component i alone at 0.2% plastic strain of the composite sample [198], σ_i is the true stress of component i , σ and ε represent the true stress and true strain of integrated composite sample. $\sigma_{i,UE}$, $\varepsilon_{i,UE}$ stand for the true stress and true strain of component i at necking point.

It is found that the yield strength of laminated-structured samples agrees reasonably well with the ROM (Eq 6.1) (shown in Fig 6.3b). Comparisons of strain hardening and uniform elongation (true strain) between experimental results and theoretical prediction from

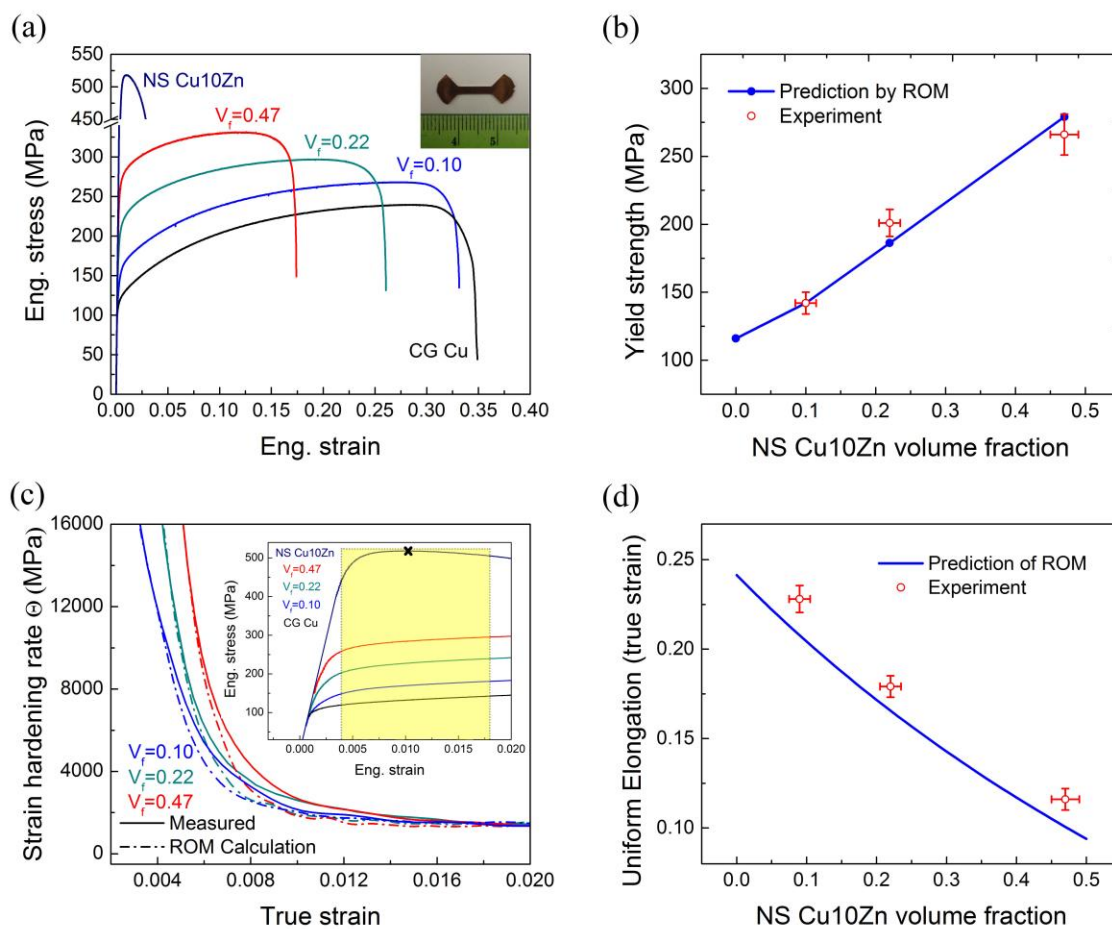


Figure 6.3 (a) Uniaxial tensile engineering strain-stress curves for pure CG Cu and NS Cu-10Zn and sandwiches with various compositions. Inset shows the dimension of tensile test samples $0.6 \times 2 \times 8.4$ mm³. (b) Yield strength versus volume fraction of NS Cu-10Zn from tensile tests and prediction from ROM. (c) Strain hardening curves from corresponding tensile tests and calculation based on ROM. Inset is the magnified tensile curve at low strains where outperformance of strain hardening (yellow shadow) occurs compared to ROM. Black crossover stands for the necking strain level in pure Cu-10Zn. (d) Uniform elongation versus volume fraction of NS Cu-10Zn from tensile tests and prediction from ROM.

ROM are shown in Fig 6.3c and d. When calculating the strain-hardening rate, we assume a constant engineering stress after necking for pure bronze. This assumption provides the maximum applied stress that a standalone bronze layer can sustain according to Considère criterion. Namely, the derived strain-hardening rate is the upper limit based on ROM and would give a conservative comparison to experimental observation. For Eq (6.3), it is also assumed that during the uniform elongation, the strain hardening of each component can be expressed by Hollomon law of $\sigma_i = k_i \varepsilon^{n_i}$ [252]. In fact, the Hollomon law has been used on NS materials in compression test [253,254] despite limit reports of applications for tensile tests due to the plasticity instability. Fig 6.3c shows that the strain-hardening rate of the laminate structure (solid) is higher than that predicted by ROM (dash-dot) at strains around necking of pure NS bronze layer. This occurs only at a limited intermediate strain range as marked by yellow shade in the inset of Fig 6.3c. The underlying mechanism of this extra strain hardening is discussed later. Consequently, the uniform elongations of laminate samples are measured higher than what is predicted by ROM (Fig 6.3d).

The integrity of interface after tensile testing was examined by SEM. Fig 6.4a is an overview of a sample, showing no inner cracks or failure through the entire uniformly elongated region except the fracture at the end. Fracture debonding should be a post-necking process due to high strain localization. In this work, the specific requirement for interface strength is only to maintain its integrity during uniform elongation until the strain where mismatch between layers and its effect on mechanical properties can be activated (<2%, as shown Fig 6.3c). In addition, the fracture surface shown in Fig 6.4b reveals a frequently-seen dimple-like feature in NS/CG interface vertical to tensile direction, suggesting the strong

interactions between NS/CG layers even after necking. All of above characteristics imply well-bonded interfaces between NS and CG layers.

Pure NS bronze has a limited tensile ductility of only 0.7% due to the lack of sufficient strain hardening. However, when sandwiched by CG Cu, its uniform elongation was increased up to over 27% (Fig 6.3a). Recent modeling work of structures with grain-size difference [255] also revealed enhanced ductility in an otherwise low-ductility layer. CG Cu has considerable strain hardening capability and therefore constrains the NS layer to postpone its necking by preventing the early-emerging tensile instability. Under such constraint, the NS bronze layer should be able to uniformly deformed further [64,147]. In addition, the mutual constraint of NS bronze layer and CG Cu layer actually adds extra strain hardening, as shown in Fig 6.3c. The proposed reason is as follows. A standalone NS bronze layer will start early necking at very low strain by fast local lateral shrinkage. When sandwiched by CG Cu, this necking process is quickly suppressed by the stable outer layers at both sides. Therefore, we refer to this as “virtual necking” since it could not proceed very far. The instable middle layer and stable outer layers mutually constrain each other as the interface still holds them together, which converts uniaxial applied tensile stress to bi-axial stresses (Fig 6.4c). As a result, more dislocations will be accumulated around the interface in order to accommodate the mechanical incompatibility across the interface, which produces the observed extra strain hardening. It follows that the strain-hardening rate of our laminate structure under this intermediate strain level can be described by modifying Eq 6.2 as

$$\frac{d\sigma}{d\varepsilon} = \sum V_i \frac{d\sigma_i}{d\varepsilon} + \Delta\Theta \quad (6.4)$$

where $\Delta\Theta$ is the extra strain hardening in addition to what is predicted by conventional ROM. This observation of extra hardening is consistent with the recent discoveries in GS IF-steel [147]. In addition, extended elastic-plastic transition due to the large yield stress mismatch, as another form of mechanical incompatibility, may also contribute more or less to this phenomenon. But careful examination of magnified tensile curve (Fig 6.3c inset) reveals those strain levels (yellow shade) for extra hardening are far away from the supposed elastic-plastic transition region ($\sim 0.1\%$ - 0.4% in Fig 6.3c inset) with comparison to virtual necking strain (black crossover). Therefore, the extra hardening in this study is majorly ascribed to the mismatched tensile instabilities across interfaces.

A big difference in the mechanical behaviors of the laminate structured materials and the GS IF steel reported earlier [147] is that no strain hardening up-turn is observed here. The reason for this difference is not clear and need further study. One possible reason could be the differences of interface nature in two cases. As reported earlier, the dislocation accumulation mainly occurs near the interfaces. Interfaces in laminates are stationary due to sharp discrepancy across layers and homogenous microstructure within each layer. Dislocation accumulation occurs only near the fixed interface and ceases when saturation of dislocation density is locally reached. Therefore, it cannot produce enough strain hardening for the whole sample. In contrast, interfaces in the GS IF steel is dynamically migrated and then allows the deposition of high-density of dislocations over their entire migrating path [147]. This makes the strain hardening free from the restriction of localized dislocation saturation and able to achieve more, which results in an up-turn characteristic.

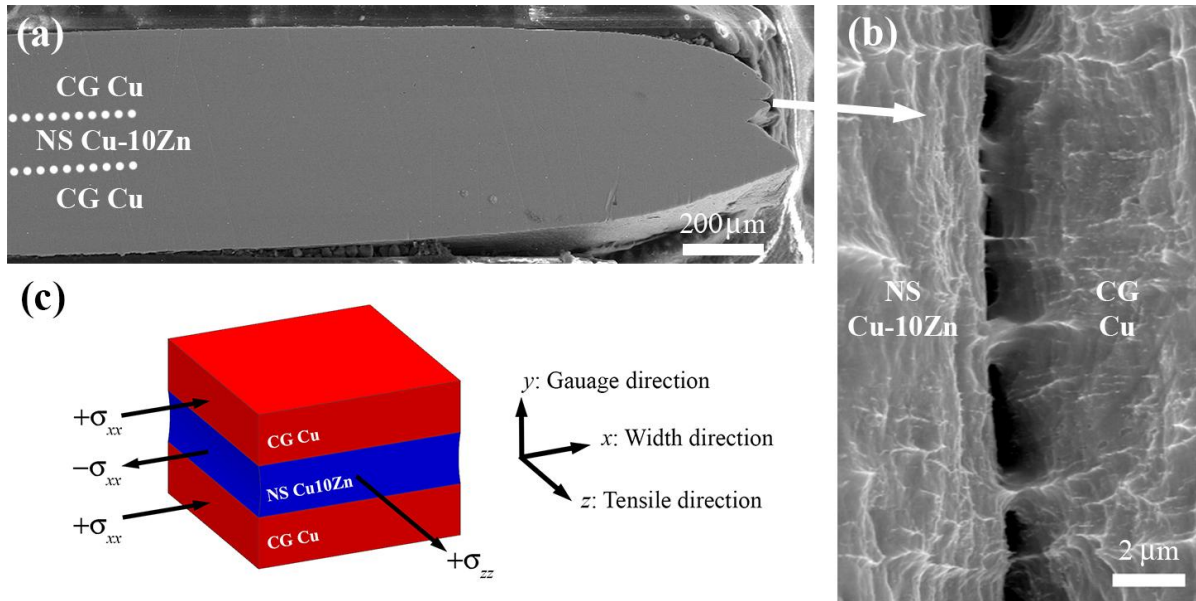


Figure 6.4 (a) Overview of the sandwich piece after tensile fracture. (b) Typical morphology at lateral fracture interface in (a). (c) Schematic illustration of stress status of the laminates around the strain level where the middle NS layer tends to shrink while outer CG layers stabilize it.

6.4 Chapter Conclusion

In summary, HPT followed by rolling and annealing was used to produce laminated materials by sandwiching a NS layer between CG layers. Uniaxial tensile test is performed and reveals an extra strain hardening that lead to larger uniform elongation than what is predicted by conventional ROM. The interface is well bonded to maintain the concurrently uniform deformation of CG and NS layers. This preliminary work suggests the importance of interface between heterogeneous plasticity and its effect on mechanical behaviors in laminate and gradient structured materials.

Chapter 7

Mechanical Properties of Cu/Cu10Zn Laminates: Role of Interfaces

Interfaces have been believed to play a crucial role in mechanical behaviors of both laminate and gradient structures. Despite the popular belief, there're very few systematic and elaborate experimental investigations to probe the details of their role in deformation physics and thereby mechanical performance. In this work, heterogeneous interfaces connecting similar microstructure but with various interface spacing are fabricated in Cu/Bronze laminate samples via accumulative roll bonding and appropriate annealing. The heterogeneity across interface involves chemical composition, grain size, hardness and texture. Simultaneous improvement of strength and ductility in samples with increasing interface density is found in tension tests. Extra accumulation of geometrically necessary dislocations in the vicinity of interfaces is experimentally observed by semi in-situ EBSD mapping during tension and fits well with pile-up model. As a result, each interface generates a most affected zone spanning only a few micrometers, which is not affected by interface spacing. On the other hand, the inverse proportional relationship between back stress hardening and interface spacing is further quantitatively verified at presented length scale. Based on the collective observations, we propose that there's an optimum interface spacing design, probably a few micrometers, for such laminate structures to achieve the best hardening capacity and tension ductility. This work highlights the unique role of

heterogeneous interface in enhancing mechanical properties of metallic materials and deepens the understanding of deformation physics in laminate and gradient structures.

7.1 Introduction

Laminate and gradient metallic structures have garnered extensive interests in the community for their very potential to achieve beneficial mechanical properties of both strength and ductility [75,256,196,160,198,257,247]. Fang et al. and Wu et al. had successfully strengthened pure Cu and interstitial free steel via gradient structures with nanocrystallized surface layer and coarse-grained interior matrix [75,198]. Furthermore, the ductility of such gradient structures didn't suffer much degradation compared to the single coarse-grained counterpart. Recent development of heterogeneous lamella structure in pure Ti embraced both the high strength of ultra-fine grains and the decent ductility of the coarse grains [193]. Both structures contain numerous heterogeneous interfaces, which are usually defined as the boundaries across which are remarkably differing chemical compositions and microstructures, like grain size and crystallographic orientation (texture) [258–260]. Heterogeneous interfaces were suspected closely related to the deformation physics and contributive to the observed high hardening and ductility in both laminate and gradient materials [148,255,196,261,255,89]. The possible mechanisms of their effect on deformation have been sketched by some recent work. Some scholars proposed the gradual stress redistribution across interfaces to explain the enhanced working hardening in a multi-layered ultrafine-grained titanium [196,262,263]. Wu and Zhu accounted for this by the transition of strain status and back-stress strengthening assisted by heterogeneous interfaces in their recent studies [147,159,193]. In retrospect, early literatures have theoretically connected

microstructural heterogeneity with strain gradient theory and the generation of geometrically necessary dislocations (GND) during plastic deformation [264–266,87]. Applying this general theory to laminates, Ashby et al. had pioneered the quantitative models and developed a reciprocal relationship between the average GND density and interfaces' spacing in an idealized laminate structures with single crystal matrix and equally spaced rigid plate-like particles [264]. However, this theoretical prediction was based on simplified assumptions and real materials may appear more complicated. For example, laminate components are mostly engineered from polycrystalline matrix and none of them are absolutely rigid [201,267]. Additionally, the details of GND configuration and their dependence on interface spacing are not fully revealed in conventional theory and have been rarely investigated in experiment-wise. These questions are both critical to understanding the fundamental mechanisms and imperative to practical material designs. For example, to what extent or how long does every single heterogeneous interface affect most during deformation? Does the most affected zone width depend on the interface spacing/layer thickness? Very few systematic evidences from both mechanics and microscopy have been provided before to clear up those questions.

Experimental clarification for abovementioned issues through direct observations has been long blocked for following reasons. First, in gradient structured, the interfaces are everywhere with the change of a gradient [148,198]. Consequently, imposed deformation across the whole gradient leads to dynamic plastic/elastic interfaces [75], which are difficult to identify or track experimentally and thereby fail to reveal their roles while deformation. Second, even for laminate structures with stationary interfaces instead, most of their

microstructures across interfaces are not quite similar for different interface densities, which poses a challenge to experimentally extract interface effect from other influences. For example, majority of laminate metallic structures fabricated by solely accumulative roll bonding (ARB) always possess finer microstructures when increasing rolling cycles [183,184]. To validly and quantitatively probe the effect of heterogeneous interfaces on mechanical performance, identical or very similar interfaces with various interface densities are necessary. The implication is that the best candidate subject for this study is the carefully designed laminate samples with similar microstructure but different interface spacing/ layer thicknesses. Third, another obstacle to impede this study was the technical difficulty of direct or in-situ observation of deformation characteristics like dislocation density during plastic loading, which was as such rarely reported before.

In present study, ARB technique incorporated with appropriate post-annealing was employed to fabricate Cu and Cu10Zn laminates. As mentioned above, the advantage of such samples are their best candidacy for systematic investigation of heterogeneous interfaces' role in mechanical properties and its mechanism. Benefited from the semi in-situ electron back-scattering scattering diffraction (EBSD) technique under tension and its intense data, deformation history of the local regions of interest are successfully recorded and provides detailed evidences to reveal how and to what extent do those interfaces affect GND activities [268–270]. Cyclic tension tests were accompanied to further confirm the interfaces' role from mechanics perspective.

7.2 Experimental Methods

Commercial copper (ASM-C11000) and bronze (ASM-C22000) were selected for this work. The chemical compositions and the general mechanical parameters of these raw materials can be referred from Table 7.1 [230,231]. The advantage of these two materials is their similar elastic constants so that experimental focus could reasonably emphasized on the plastic deformation regime. The 1mm thick raw Cu and bronze sheets were ARB-processed with 2, 3 and 5 cycles and achieve 4, 8 and 32 layers, respectively. The edge regions where sheets tend to tear from each other were cut away and the central part with better initial bonding strength was used for following treatment. Details of ARB processing can be referred from early work [200,201]. All of the samples were then annealed at 250°C for 2hrs in a vacuum tube furnace (Mini-Mite™) together under Argon protection and thereafter named as N2, N3 and N5 samples, respectively.

Table 7.1 Chemical compositions and general material properties of raw materials [200,230]

Chemical Compositions (wt.%)						
	Cu	Pb	Fe	O	Zn	Others
Copper	≥99.90	-----	-----	0.04	-----	≤0.06
Bronze	89.0~91.0	≤0.05	≤0.05	-----	10.0	-----
Material Parameters						
	a (Å)	γ_{SF} (mJ/m ²)	E (GPa)	ν	G (GPa)	
Copper	3.61	45	115	0.324	44	
Bronze	3.64	35	115	0.307	44	

Samples for Ion Channeling Contrast Microscopy (ICCM), micro-hardness testing and Electron Back-Scattering Diffraction (EBSD) observation were first cut from the annealed samples and then mechanically polished by sandpapers to achieve a mirror surface. Electrochemical polishing was then performed to remove the possible strained surface layers that may affect following tests. The electrolyte consists of a phosphoric acid (concentration of 85%), ethanol and deionized water with volume fraction as 1:1:2. ICCM and EBSD were conducted under a FEI Quanta 3D FEG dual-beam instrument. Texture analysis was based on EBSD maps with view-size of $30 \times 100 \mu\text{m}^2$ to capture the global characteristic. For local misorientation mapping, each EBSD scan was performed under 30kV and 16nA electron beam and with binning size of 2x2 to achieve the angular resolution as high as possible from the instrument [271,272]. Statistical averaging was conducted in later analysis to further reduce the noise significance. Scan step size was set $0.1 \mu\text{m}$ to ensure appropriate spatial resolution. Transmission Electron Microscopy (TEM) foils were prepared by mechanically polishing specimen to $\sim 30 \mu\text{m}$ and attached to Φ -3mm Mo rings followed by ion-milling perforation. The milling process was under protection of liquid nitrogen at -50°C to avoid potential grain growth. TEM observation was performed in a JEM-2010F microscope operating at 200kV at room temperature. Dog-bone shaped tensile samples with a gauge dimension of $10 \times 2 \times 1 \text{mm}^3$ were machined from the annealed sheets and uniaxial tension tested by a Shimadzu AGS machine. Both single and cyclic tension tests were carried out under room temperature at strain rate of $9 \times 10^{-4} \text{s}^{-1}$ and each test was repeated as least for 3 samples to guarantee the data reproducibility. Note that the semi in-situ mapping was realized by transporting one specimen back and forth between cyclic tension tester and EBSD facility

chamber. Three strain levels, 0%, 3% and uniform elongation strain, were selected to map the region of interest in each sample. The interfacial region of interest was carefully marked by a close but immaterial milling feature.

7.3 Results

7.3.1 Overview of microstructures

Figure 7.1a-c are the optical microscopy observations of all sample, indicating a clearly differing laminate geometry due to their various layer thickness/interface spacing. In this study, samples for all tests are were cut from the middle of the sheet and their layer symmetry is quite satisfied and inter-layer interfaces are well aligned, which won't throw much error in the quantitative analysis based on component factions. Given the same sheet thickness, the each layer thickness for N2, N3 and N5 samples are correspondingly 250, 125 and 31 μ m. The post-annealing microstructures around interfaces are present in Figure 7.1d-e, which present a quite similar microstructure in all samples despite their different ARB cycles. Coarse Cu grains with considerable annealing twins are observed in all N2, N3 and N5 samples in ICCM. This feature was believed originated from its recrystallization process during annealing, which is further confirmed by the texture analysis later. With respect to Cu₁₀Zn phase after annealing, it still largely remains the rolling feature in all samples. Compared to N3 and N5 samples, Cu₁₀Zn has a slightly greater feature size in N2 samples, as shown in Figure 7.1. This is probably resulted from the relatively fewer rolling extent in N2 sample. But later hardness and texture characteristics show that their difference is not

quite significant. Very minor ultra-fine and even nanocrystalline Cu₁₀Zn grains were locally dispersed in the vicinity of the interfaces, which is observed in all samples under ICCM.

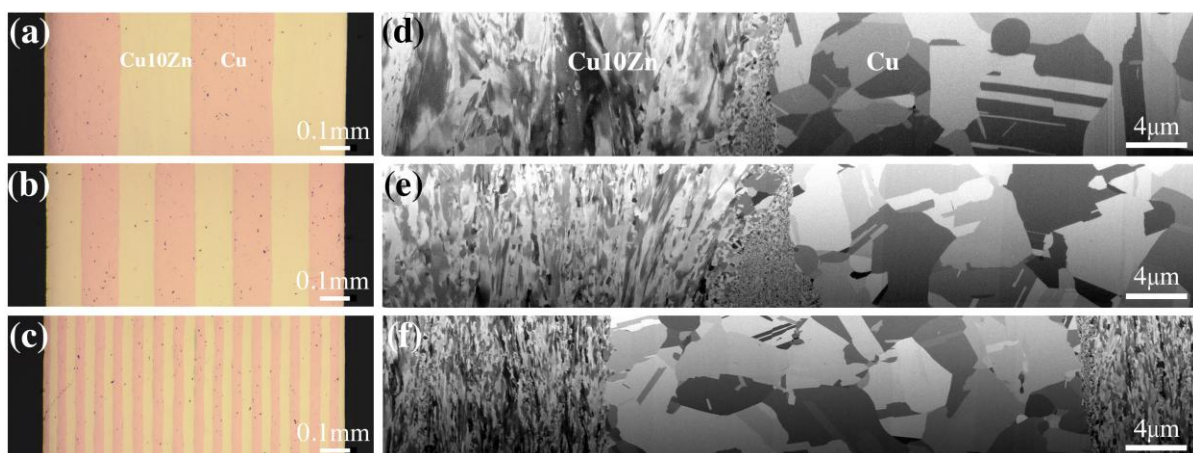


Figure 7.1 Optical microscopy of (a) N2, (b) N3 and (c) N5 samples, respectively. It clearly shows the inter-layer contrast and the interface spacing. ICCM observation of (d) N2, (e) N3 and (f) N5 samples, showing the microstructures at Cu/Bronze interfaces samples.

7.3.2 Heterogeneity across interfaces

A representative Cu/Bronze interface taken from N5 sample under TEM is presented in Figure 7.2a, which reveals a void-free transition from CG Cu to nanostructured Cu₁₀Zn across the interface. Clearly, the recrystallized CG Cu grains are much cleaner and exhibit less dislocation contrast while Cu₁₀Zn layer is more defective as a deformed microstructure. Figure 7.2b shows the corresponding details of the Cu₁₀Zn side. Retained rolling microstructure featured by elongation grain along rolling direction is still the majority of the Cu₁₀Zn layer after annealing. Transverse grain size of such rolled microstructure is

statistically analyzed by TEM observation and has a mean value of $\sim 100\text{nm}$, as shown in Figure 7.2d. The grain size distribution of Cu layer is examined based on the previous ICCM of all samples and presented in Figure 7.2c. In contrast to Cu10Zn layer, average of Cu grain size is $\sim 5\mu\text{m}$, which is about $50\times$ times in length scale. The feature size difference composes an important discrepancy across the heterogeneous interface.

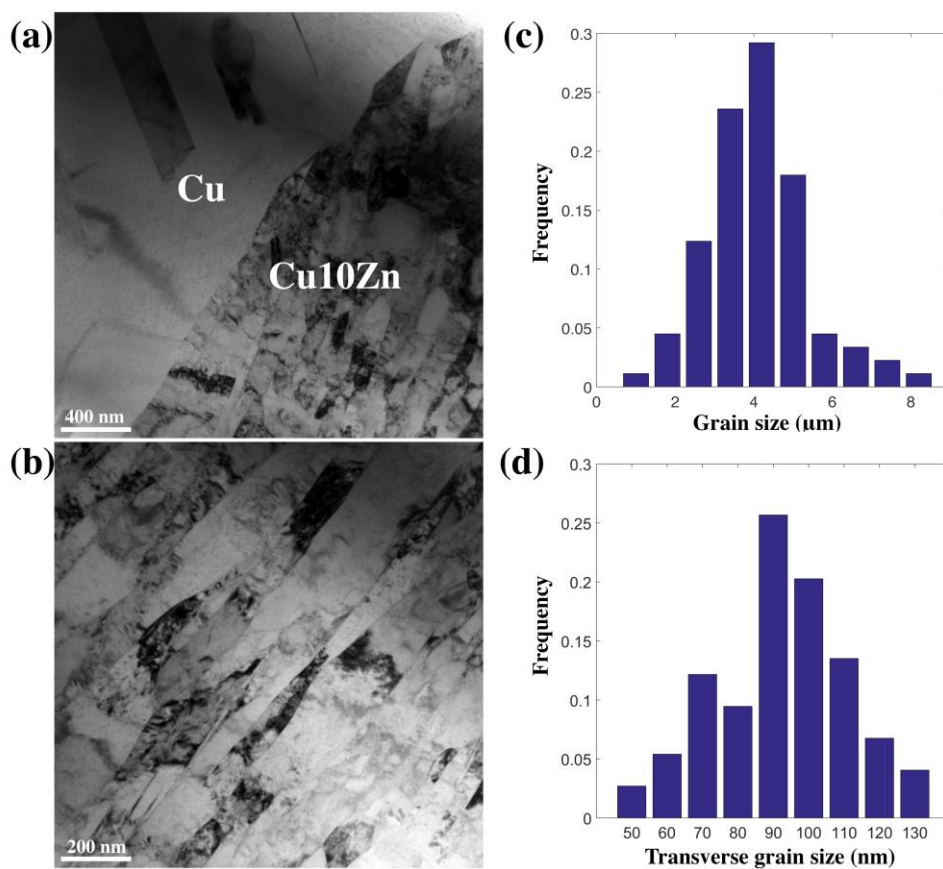


Figure 7.2 (a) TEM observation of Cu/Bronze interface of ARB N5 sample shows the void-free interface and the discrepant grain size across it. (b) Retained rolling microstructure in Cu10Zn layer. (c) Grain size distribution of the Cu layers based on the ICCM above. (d) Transverse grain size right to rolling direction in Cu10Zn layers based on the TEM results.

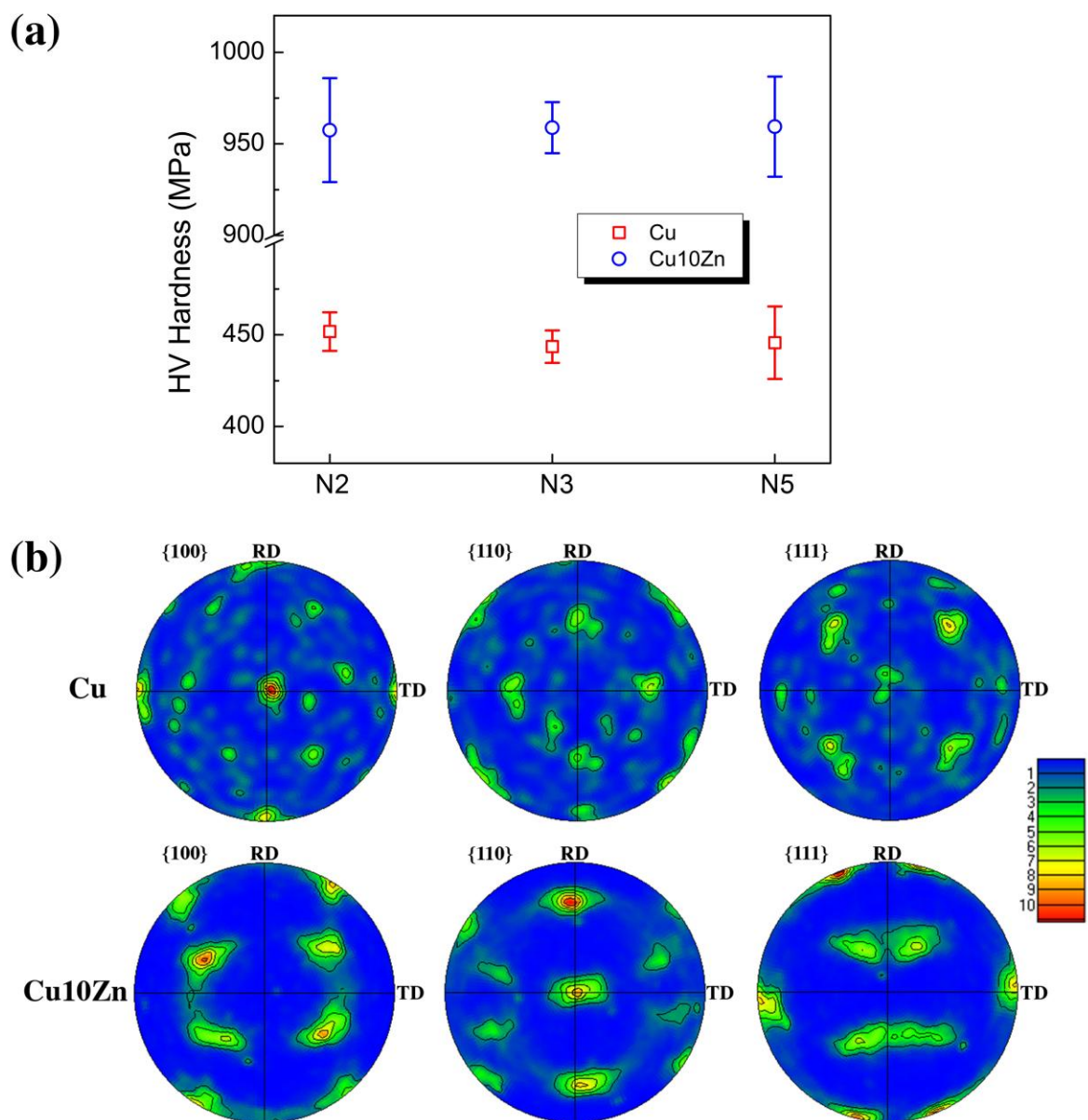


Figure 7.3 (a) Micro-hardness measurement of both Cu and Cu10Zn layers in N2, N3, N5 samples after annealing. (b) $\{100\}$, $\{110\}$, $\{111\}$ Pole figures in both Cu and Cu10Zn layer in N3 sample after annealing, showing the strong cube texture and a derivation of brass-type texture, respectively.

Note that N2 and N5 have similar texture characteristics.

In addition, hardness is expected to have sharp difference across interface as well due to the various chemical composition and grain size. Figure 7.3a is the micro-hardness testing results. Obviously, the nanostructured Cu10Zn (~950MPa) is more than two times harder than the CG Cu (~450MPa). It's noteworthy that the micro-hardness of both Cu and Cu10Zn are pretty much close in all samples given the measurement errors, confirming their similarities regardless of interface spacing. Crystallographic orientation preferences also remarkably vary across the interfaces. As shown in Figure 7.3b, Cu exhibits a strong cube texture component $\{001\}\langle 100\rangle$, which is resulted from both recrystallization and grain growth [273]. Again, this texture feature agrees with the recrystallization microstructure of Cu discussed before. In a stark contrast, Cu10Zn shows a significantly different texture after processing: a derivative of typical brass-type texture $\{110\}\langle 112\rangle$ with slight variation [273,274]. This is consistent with previous reports of brass-type rolling texture observation in FCC alloys with low stacking-fault energy [275]. Post-annealing under current temperature after ARB doesn't affect the rolling feature of Cu10Zn layer much. Note that although the present pole figure is scanned from the N3 sample, results from N2 and N5 also show the common cube and brass-type texture features in Cu and Cu10Zn layer, respectively.

Therefore, by incorporating ARB and appropriate annealing in this study, one can successfully produce heterogeneous interfaces, across which chemical composition, grain size, micro-hardness and texture components are drastically different. In addition, this heterogeneity of interface is similar even if the interface spacing is changed. This paves the way for following characterization and discussion of interface role in mechanical properties.

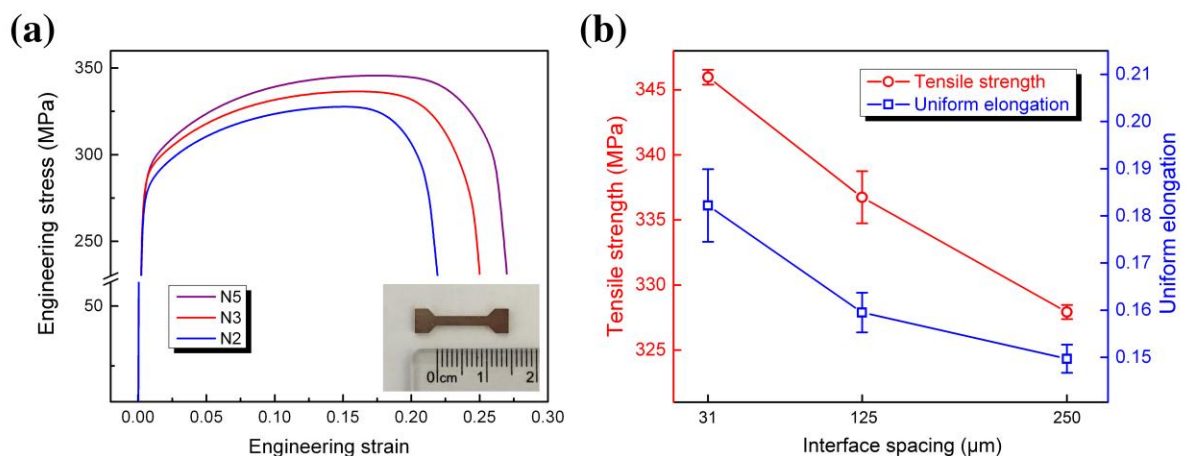


Figure 7.4 (a) Tensile curves of N2, N3 and N5 samples show the simultaneous increase of strength and elongation with increasing number of layers. (b) Summary of tensile results. Error bars represents standard deviation from at least 3 data sets.

7.3.3 Uniaxial tensile tests

Figure 7.4a is the tensile curve results for N2, N3 and N5 sample respectively. Inset is an example of the tested sample dimension. It's clearly found that both the tensile strength and uniform tensile elongation increase with the increase of the layer number/interface density. Repeating tests at least three times for each sample and we summarized the results in Figure 7.4b. The observation of the simultaneous improvement of tensile strength and ductility with decrease of interface spacing is confirmed to be reproductive in this study. Interestingly, the yield strength doesn't increase too much with the change of interface spacing. Implication of relatively stable yield strength and increased ultimate strength is the enhanced strain hardening behavior with decreasing interface spacing. This would be a

central topic to be discussed later. It's worth to note that some earlier ARB studies also reported such simultaneous improvement but most of them have differing microstructures in addition to the change of interface spacing, i.e. they accounted for this by microstructure difference instead of the inter-layer interface [184,186,276]. This is a critical difference from this work.

7.3.4 Semi in-situ EBSD mapping and GND characterization

Figure 7.5 is the overview of EBSD inverse pole figure mappings of Cu layer at zero strain, 3% tensile strain and the uniform elongation strain level of each sample. Note that due to the sight limit, the mappings for N2 and N3 samples are the exact part that is close to the interface (as marked in Figure 7.5). For N5 sample, the whole Cu layer is captured. The grain elongation along the tensile direction is obvious and the mapping indexing rate isn't reduced much with increasing the deformation strain, as shown in Figure 7.5. This facilitates the investigation of the deformation characteristics in regions of interest during the whole tension history. In this study, we picked up the so-called kernel average misorientation (KAM) method to determine the local misorientation directly from the EBSD orientation data [270]. First, we define the onset of the general grain boundary misorientation as 3°. Any misorientation greater than this value will be excluded in local misorientation calculation since it crosses a grain boundary and not count to GND. The local misorientation of every single point (100×100nm²) was then determined by the 24 surroundings.

$$\theta_0 = \frac{\sum_{i=1}^{24} \theta_i \cdot I_{(\theta_{i < \alpha})}}{\sum_{i=1}^{24} I_{(\theta_{i < \alpha})}} \quad (7.1)$$

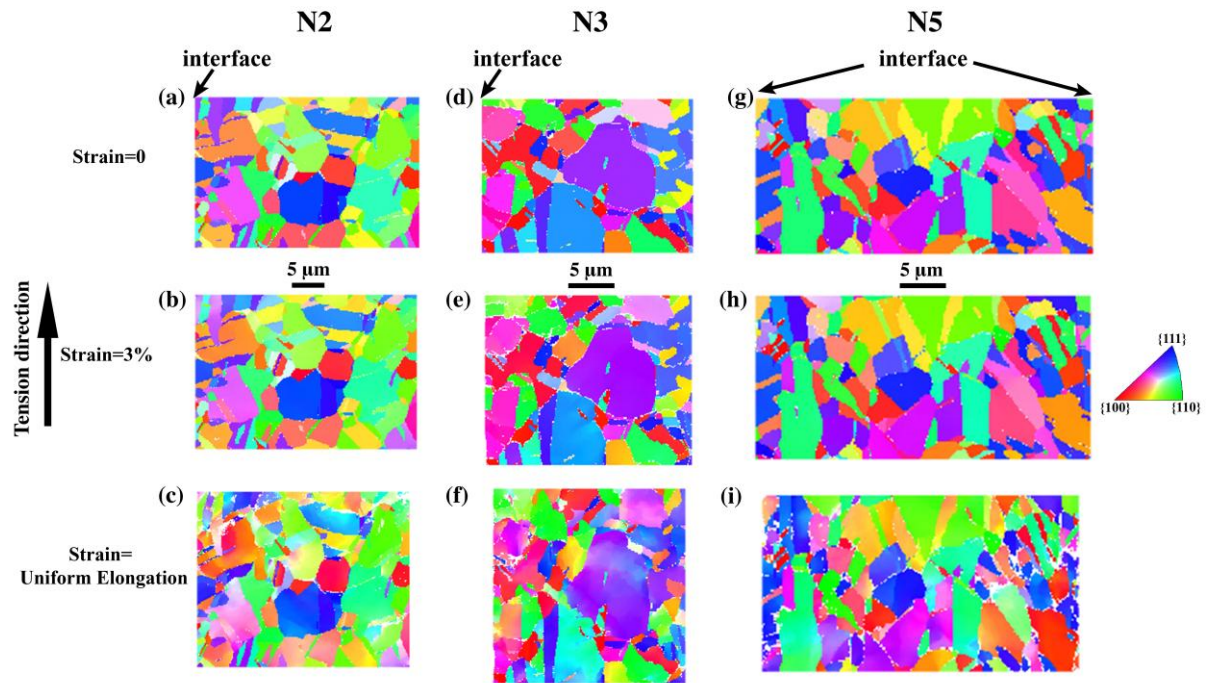


Figure 7.5 Inverse pole figure mapping of regions around interfaces in (a-c) N2, (d-f) N3 and (g-i) N5 samples under different tension strain levels: 0%, 3% and maximum uniform Elongation. Left side of N2 and N3 samples are the Cu/Bronze interfaces and both sides in N5 sample are the Cu/Bronze interfaces

Where θ_0 represents the resulted local misorientation for the corresponding point and θ_i is the misorientation between this point and its neighbor point i . I is indicator function and α is the predefined grain boundary misorientation threshold (here is 3°). To extrapolate the GND density information, we use a simple method from the strain gradient theory by Gao and Kubin [86,87]:

$$\rho^{\text{GND}} = \frac{2\theta}{ub} \quad (7.2)$$

ρ^{GND} is the GND density at points of interest, θ represents the local misorientation, b is the material's Burger's vector and u is the unit length of the point. The resulted GND density maps are shown in Figure 7.6 for all samples of corresponding tensile strains. Clearly, the overall level of local misorientation is elevated with the increase of tensile strain, this is as expected from the deformation in polycrystalline materials, which are non-homogeneous [264,268]. It must be also noted that the GND density is not uniform across the whole mapping region, which is not discussed in conventional theory [264,266]. Figure 7.7 shows the histogram distribution of GND density for each map. The GND distributions of three samples are pretty much similar at each level of tension strain. Here, we need to mention the measurement error in the study. Previous researches on EBSD technique indicated the measurement error might dominate when the misorientation to measure is very small and the error level is negatively correlated to the real misorientation level [272,277]. Taking the extreme case, we attribute all the misorientation measurement under zero strain to the measurement error. The resulted upper limit of measurement error of GND density is less than $1.73 \times 10^{14} \text{m}^{-2}$, which is reasonable compared to the early report [278]. Keep in mind that the error level should be lower for high misorientation measurement like at uniform elongation strain.

An important feature in Figure 7.7 is that the more tension strain the laminates underwent, the more variance is the GND density distribution although the average GND density goes up. This is definitely the truth from deformation phenomenon, rather than measurement error, because the latter has an inverse trend [277].

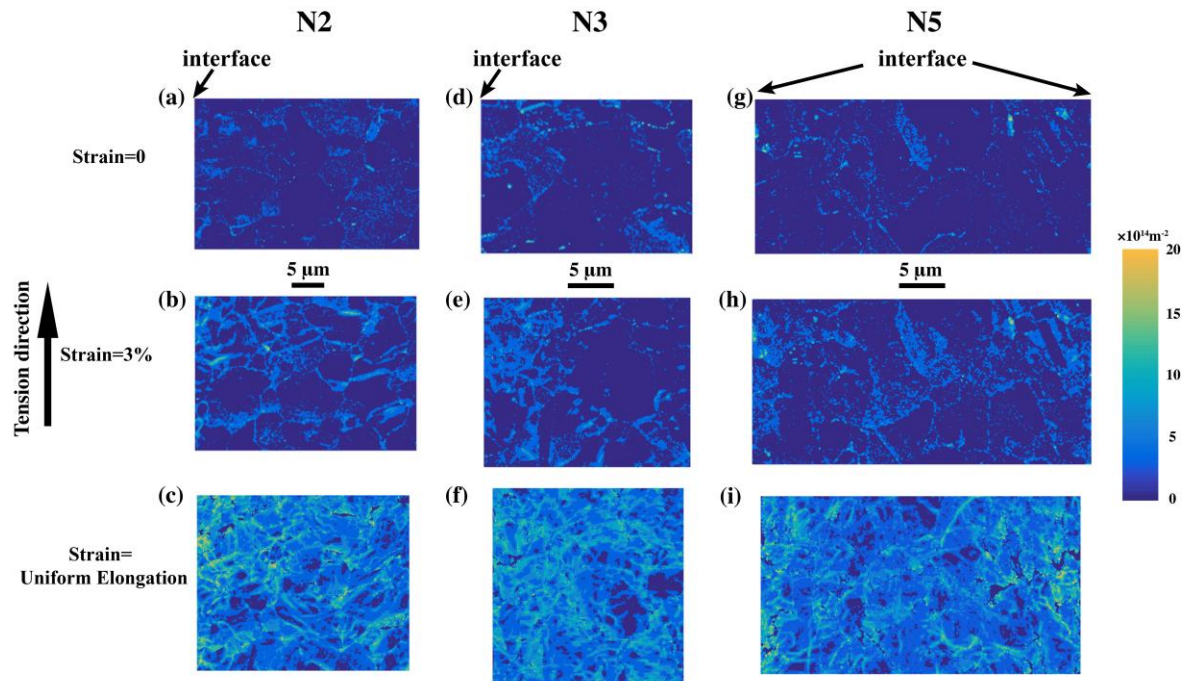


Figure 7.6 GND density mapping based on local misorientation results in (a-c) N2, (d-f) N3 and (g-i) N5 samples under different tension strain levels: 0%, 3% and maximum uniform Elongation. Left side of N2 and N3 samples are the Cu/Bronze interfaces and both sides in N5 sample are the Cu/Bronze interfaces.

GND density is correlated to the strain gradient and therefore these results indicate that the strain gradient is not uniform and it becomes more severe with increasing plastic strain. One source for the non-uniform strain gradient and GND density is expected as the massive and randomly distributed polycrystalline grain boundaries. They serve as roadblocks to dislocation motions and therefore locally generate GNDs with straining [268,270]. The generated GND value is also relevant to the corresponding crystallographic orientation and varies from grain to grain.

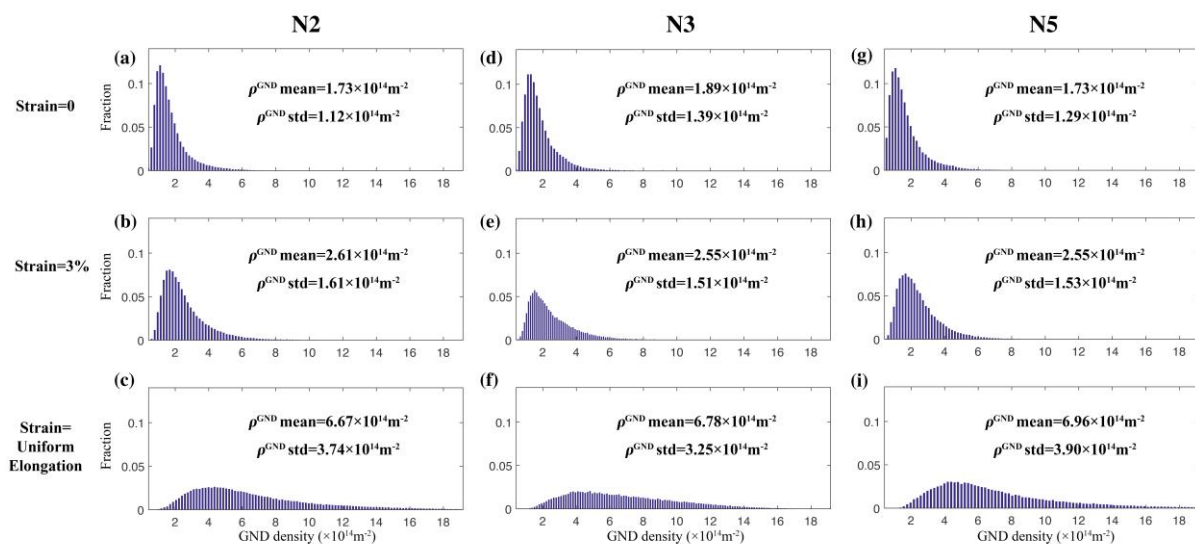


Figure 7.7 Global GND density distribution on the corresponding mapping results in Figure 7.6. The mean value and standard deviation of GND density for the mapping are labeled in each histogram.

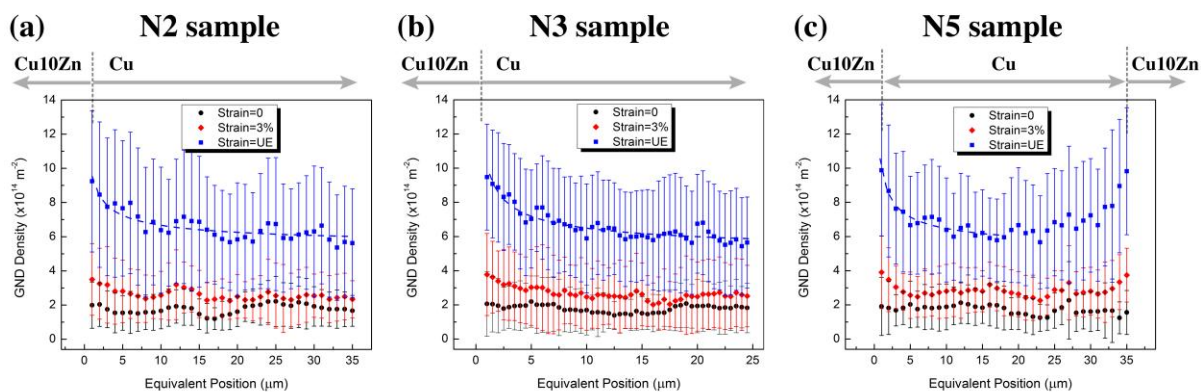


Figure 7.8 Integrated GND density in Cu layer versus the equivalent distance from the interfaces at different strain levels of (a) N2 sample, (b) N3 sample, (c) N5 sample. Dash lines represent pile-up model fitting results.

Another important source would be the macroscopic heterogeneous interfaces. To extract their role from the mask of grain boundaries, crystallographic orientation and other noise, we sliced the mapped region into pieces along the interface direction and took the average of the GND density in each slice. First, the grain boundary effect is reasonably assumed removed. Second, the previously mentioned measurement error of single point is significantly reduced (We have more than 100 data points in each slice would reduce at least an order of the final measurement error according to simple statistics) [272]. The resulted GND densities versus their equivalent distance from interfaces are shown in Figure 7.8. Given the measurement error upper limit of $1.73 \times 10^{13} \text{m}^{-2}$, one needn't worry much about its influence on the present data. Figure 7.8 reveals the gradually extra GND accumulation trend near the interface during deformation. This most affected zone spans only a couple of micrometers from the interface. This is the general phenomenon in all three samples and becomes much obvious when the strain goes to the maximum uniform elongation level. Note the GND level within layer interior is rather smooth across all samples, i.e. the interface effect declined quickly at distanced regions and all other random factors collectively achieve a less waving GND density at layer interior.

7.4 Discussions

7.4.1 Dislocation pile-up model for the GND density close to interfaces

Upon tension, heterogeneity across interfaces play as obstacles to dislocation motions and lead to an incompatible deformation process, which gradually brings about local strain gradient in the vicinity of interfaces. Dislocation pile-up model has been established before to

account for such role of obstacles in the way of deformation path [32,33,279]. The consequent GND distributions are thereby derived. We fit this theory with our GND data to validate the interfaces' role in laminate structures. Datasets from the uniform elongation strain level are focused because they're the least affected by the measurement noise and exhibit the most remarkable trend. Conventional pile-up model reveals that GND density $\rho^{\text{GND}}(x)$ is inversely proportional to $k/\sqrt{x(a-x)}$, where x is the distance from the obstacle, k and a are constants [33]. Given the averaged GNDs stemmed from grain boundary and orientation effects ρ_0^{GND} , the fitting function is modified to

$$\rho^{\text{GND}}(x) = \frac{k}{\sqrt{x(a-x)}} + \rho_0^{\text{GND}} \quad (7.3)$$

The fitting results of GND density are superimposed in Figure 8 and agree well with the observed uniform elongation datasets. This indicates that the dislocation pile-up model captures the major physics of GND accumulation at macroscopic heterogeneous interface in laminate structures during deformation. Fitting results also reveal the estimate of ρ_0^{GND} , which doesn't change much in three samples: $\rho_0^{\text{GND}} = 5.1, 4.8$ and $4.9 \times 10^{14} \text{m}^{-2}$ in N2, N3 and N5 samples, respectively. Subtracting this value to the GND density at positions very close to interfaces, one can envision that about half of GNDs are caused by the interface-induced pile-up. This is a considerable amount that comparable to the collective effects from all the other microstructure factors. The similar estimations of GND density in layer interior also agree well with the micro-hardness measurement of uniform elongated region in three samples after tension, which is shown in Figure 7.9. The implication of these results is that

hardening capacities of layer interior are approximately the same regardless of different interface density in samples. Therefore, the better-off mechanical properties in Figure 7.4 are largely attributed to the effect from the macroscopic heterogeneous interfaces.

The demonstrated pile-up model here is, of course, still a simplified version, which lacks consideration of screw dislocation components and ignores the possible interaction between effects of grain boundary and macroscopic interfaces. The further specification of true distribution of GNDs near such interfaces needs more quantitative works.

7.4.2 Role of interface in deformation of nearby bronze grains

Transverse grain size of bronze layer is about 100nm, which makes it difficult to characterize the deformation history by the same EBSD technique due to the instrument resolution limit. Our recent work on Cu/bronze/Cu sandwich with similar microstructures resolved a roughly symmetric plastic strain gradient distribution across interface by digital imaging correlation. The extra GND accumulation by pile-up is expected applicable to bronze side as well. Although the hardening in bronze layer interior upon tension is not as high as Cu layer (see Figure 7.9), extra hardening by GND accumulation could be generated in nanostructured layer close to interfaces, which has been observed in gradient structures as well [147,261]. This is because the latter hardening stems from the extra strain constraint in order to accommodate the incompatible plasticity during deformation.

In addition, nanostructured materials may have other favored deformation mechanisms like twinning, grain boundary mediated dislocation emission and etc. [2,100], which usually require a higher driving stress than the slips in coarse-grained counterparts.

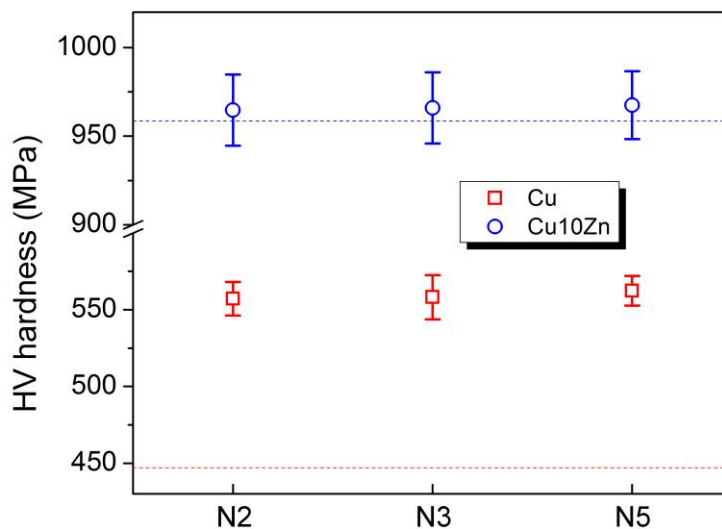


Figure 7.9 Micro-hardness measurement of layer interior at uniformly elongated sample region after tension. Dash lines represent the base level before tension.

Such mechanisms could be even promoted at grains close to heterogeneous interface for following reasons. First, the abovementioned dislocation pile-up will produce a shear stress field across the interface and this stress field is expected higher than that from pile-up at conventional grain boundaries because of higher heterogeneity [32,33]. Second, defective bi-metal interfaces are also dislocation sources and sinks that would assist grain boundary mediate deformation mechanisms in nanostructured layer [280]. Figure 7.10a is a TEM observation, showing a Cu/Bronze interface after tension deformation. Figure 7.10b is the corresponding high-resolution micrograph, showing the interface details. Right to the interface is a large Cu grain with an annealing twin and left is a Cu10Zn grain with only

30nm grain size. A deformation twin in Cu₁₀Zn is nucleated from the exact position where the interface intersects a annealing Cu twin, which strongly supports the role of defective bi-metal interface in promoting deformation of closed nanostructured grains [280,281].

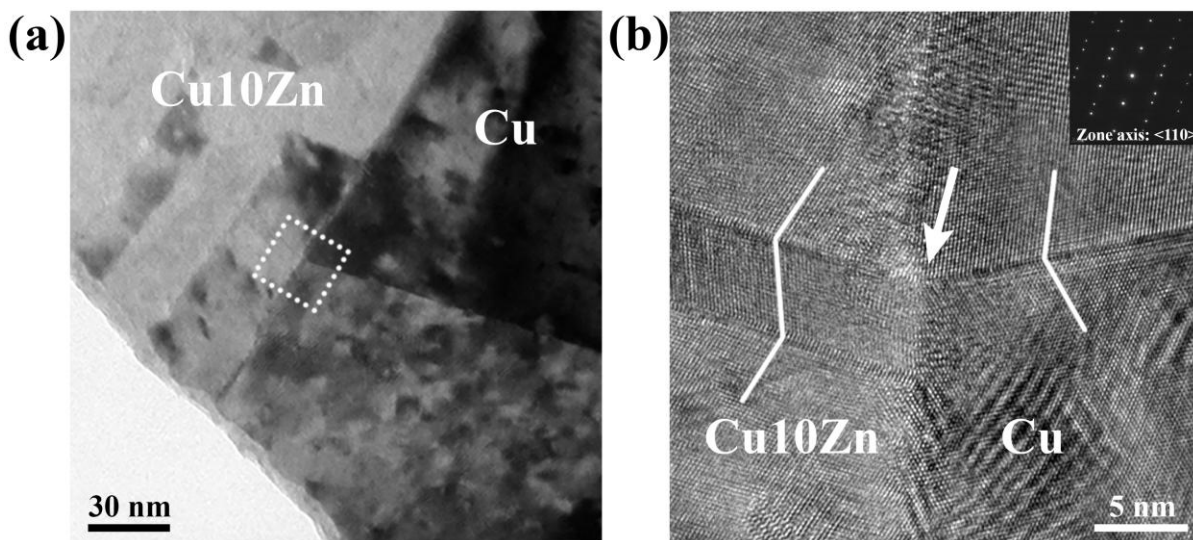


Figure 7.10 (a) A TEM observation of Cu/Bronze interface in N5 sample after tension. (b) The high-resolution microscopy of the marked square in (a). Inset diffraction pattern shows the zone axis of Cu side is $\langle 110 \rangle$. The symmetric diffraction spots reveal the annealing twin in the Cu grain, which is also marked in the image. Another thinner deformation twin in Cu₁₀Zn side is highlighted as well. Nucleation site for the deformation twin is marked by arrow.

Both viewpoints elucidate the role of heterogeneous interfaces in facilitating the extra deformation physics of bronze grains close to the interface, which brings about the improved hardening capacity and tension ductility.

7.4.3 Back stress strengthening via heterogeneous interfaces

Dislocation pile-up would produce back stress, which is a long-range stress field to prohibit the further activation of dislocation source [33,282]. In other words, higher plastic flow stress is needed to overcome this field to sustain further deformation. This mechanism is highlighted in a recent work focusing on Ti lamella microstructures [193]. Macroscopic heterogeneous interfaces here are expected to have something common with respect to this concept. Furthermore, since the interface spacing/density is specified in this work, it's of promise to quantitatively confirm the role of interface in back stress hardening. Results from cyclic tension tests are shown in Figure 7.11a. Based on a recently developed algorithm by Yang et al. [283], the calculated back stresses are shown Figure 7.10b. It's found that N5 sample has the most back stress hardening. Dots lines represent the fitting results of a widely used kinematic hardening rule for back stress: $\sigma^{\text{back}} = m\varepsilon^n$. Back stress has been reported closely related to the pile-ups at obstacles [33,284] and here, for simplicity, we reasonably assume that the back stress hardening could decompose into two components

$$\frac{d\sigma^{\text{back}}}{d\varepsilon} = \Theta^{\text{back}} = \Theta_{\text{C/Binterface}}^{\text{back}} + \Theta_0^{\text{back}} \quad (7.4)$$

$\Theta_{\text{C/Binterface}}^{\text{back}}$ is the back stress hardening component caused by Cu/Bronze heterogeneous interface and Θ_0^{back} is the back stress hardening from other general microstructure factors like grain size, orientation. Θ_0^{back} is not relevant to interface and about the same in because all three samples have similar microstructure, which has been proved by the previous microstructure characterizations, GND fitting and micro-hardness measurements. We wish to

examine whether each heterogeneous interface plays an identical role in hardening behavior and therefore assume that $\Theta_{C/B\text{interface}}^{\text{back}}$ is proportional to the interface density, i.e. inversely proportional to interface spacing d :

$$\Theta_{C/B\text{interface}}^{\text{back}} = k / d \quad (7.5)$$

If this relation holds true, one can anticipate the following equation from back stress data

$$\frac{\Theta_{N5}^{\text{back}} - \Theta_{N3}^{\text{back}}}{\Theta_{N3}^{\text{back}} - \Theta_{N2}^{\text{back}}} = \frac{1/d_{N5} - 1/d_{N3}}{1/d_{N3} - 1/d_{N2}} \quad (7.6)$$

Therefore, we can extract the back stress hardening from the fitting curves in Figure 7.11b and estimate the ratio of the left-hand side of Eq. (7.6) to be 5.44, as shown in Figure 11c. Comparing this to the expected value, 6, from the right-hand side, one can loosely confirm the previous assumption in Eq. (7.5), i.e. all the interfaces play similar roles in generating GND pile-ups and therefore the extra back stress hardening produced by such interface is inversely proportional to the interface spacing at presented length scale.

The above analysis does primarily verify the relationship expressed in Eq. (7.5) but is still loose. The back stress hardening may not be simply decomposable like in Eq. (7.4), which will make quantitative modeling more difficult and need more studies.

7.4.4 Interface spacing vs. mechanical performance

It must be reminded that the previous discussion of back stress hardening and interface spacing didn't take the non-uniform GND distribution into account.

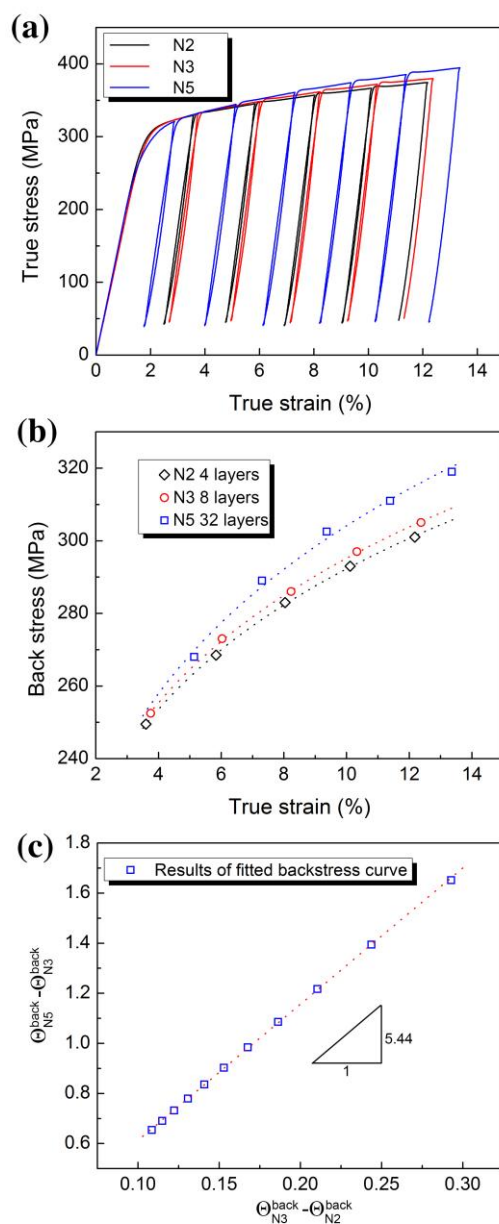


Figure 7.11 (a) Cyclic tensile curves of N2, N3, N5 samples. (b) The calculated back stress at corresponding strain levels. The dot lines are superposition of fitted hardening stage. (c) Derived backstress hardening between N3 & N2 samples and N5 & N3 samples, indicating a linear relationship close to mechanism prediction.

Recall that Figure 7.8 and pile-up model fitting reveals that most affected zone for extra GND generation is about micrometers from the interface. Therefore, relationship in Eq. (7.6) may only be valid when the interface spacing is greater than this critical value. Below this, the extra GND is probably not able to be full generated due to the limit inter-layer space. The overall strength would increase because the micrometer grain size is no longer the feature size to determine the strength and interface-related mechanism may dominate the yielding process. This has been widely observed in nano-layer laminate structures [192,285]. Compared to thicker laminates, nano-layer laminates are also reported to usually exhibit disappointing tensile ductility [286,287], which indicates that the “the thinner, the better” rule is not always applicable to ductility of laminate structures.

Based on this discussion, it’s therefore proposed that there may exist an optimum interface spacing design for the best hardening and ductility performance laminate structures. The ideal interface spacing/layer thickness is probably about a couple of micrometers that allows for the most affected zone for GND accumulation during deformation.

7.5 Chapter Conclusion

In summary, we present a series of Cu/Bronze laminates with similar intra-layer microstructures but different inter-layer thickness, which are fabricated by ARB and appropriate post-annealing. Facilitated by these ideal samples and semi in-situ EBSD technique, the role of heterogeneous interfaces on deformation and resulted mechanical properties are systematically investigated. The main conclusions are

(1) The sharp heterogeneity across interfaces is generated, including chemical composition, grain size, micro-hardness and overall crystallographic orientation (texture). This heterogeneity is of similar level across all laminate samples with different interface spacing, which paves the way to quantitatively probe the interfaces' role in deformation.

(2) It's found that the ultimate strength and tension ductility are both improved with decreasing the interface spacing in uniaxial tension tests. Gradual accumulation of extra GND during tension deformation is observed in the vicinity of heterogeneous interfaces with increasing strain levels. While in layer interior, the GND density is about the same level for all samples, which is consistent with micro-hardness measurement. Collectively, these observations reveal that improved mechanical property is largely attributed to the emergence of heterogeneous interfaces.

(3) Heterogeneous interfaces are observed to play critical roles in deformation physics in both coarse-grained and nanostructured layer sides. Their most affected zones to accumulate GND always spans about a couple of micrometers close to interfaces regardless of interface spacing. This is not discussed in the conventional uniform strain gradient theory in deformation.

(4) The relationship between interface spacing and mechanical property is finally discussed. At present length scale, a simplified hardening decomposition model reveals that the back stress hardening capacity is inversely proportional to the interface spacing. Combining the observation of the most affected zone length, we reasonably propose there's an optimum interface spacing design for the best hardening and ductility performance laminate structures.

Chapter 8

Conclusion and Future Outlook

This dissertation focus efforts on two major fields that are relevant to elevating mechanical properties of metals and alloys, especially nanostructured (NS) materials. One is the deformation twinning. Understanding the conditions that control the stability and macroscopic strain status of deformation twins is much helpful to assist the further microstructure design aimed at superior mechanical performance. The other one is the laminate/gradient structures. The fabrication of metallic laminate structures and the investigation of the effect from their microstructure, especially interfaces, on mechanical properties is an ongoing topic and garners extensive efforts. Our observations and findings in this desertion provide new insights into understanding the fundamental mechanisms and will assist the further microstructure design of metallic materials aimed at superior mechanical performance.

In Chapter 4, we systematically found the optimum grain size for deformation twinning in NS Cu-Zn alloys increases with increasing Zn content. This result agrees with the reported trend but is much weaker than predicted by stacking-fault-energy based models for pure metals. To elucidate the observation, we proposed the qualitative modification of earlier dislocation-based models by taking the different fault energies due to alloying into consideration.

In Chapter 5, it's found that the statistical decrease of zero-strain deformation twinning with decreasing stacking-fault energies by alloying. This is a clear contrast to most

previous literature reports, where most deformation twins in NS face-centered cubic metals do not produce macroscopic strain. Underneath mechanism explanation assisted with detailed microscopy analysis is provided based on one of the two major mechanisms that produce zero-strain twinning: cooperative slip of three partials under external applied stress. Lower SFE weakens this mechanism and statistically reduces the fraction of twins with zero strain.

Further interesting questions pertinent to the deformation twinning in NS materials include the grain size effect on twinning lamella thickness and how does those twins with and without strain influence the plastic deformation behaviors and global mechanical performance of NS materials. All these problems are of both scientific importance and practical significance and therefore desire further investigations.

In Chapter 6, sharp interlayer interfaces with sufficient bonding strength were developed in Cu/Cu10Zn/Cu sandwich laminate. More importantly, mechanical incompatibility between different layers during tensile deformation is expected produced high strain hardening, which led to an observed tensile ductility higher than prediction by the rule-of-mixture.

In Chapter 7, we found the simultaneous improvement of strength and ductility in Cu/Cu10Zn laminates with less interface spacing. It's observed that each interface generates extra geometrically necessary dislocations in the vicinity of itself with a most affected zone spanning a few micrometers, which is not affected by the interface spacing. Meanwhile, back stress hardening capacity is found inversely proportional to interface spacing at presented length scale. Consequently, the collective observations imply an optimum laminate design for best hardening capacity and ductility.

A growing body of investigations are undergoing with respect to laminate and gradient structures. Therefore, many fundamental problems are imperative and need both experimental and theoretical studies. Our findings primarily reveal the heterogeneous interface role in deformation and many other details still remain unsettled. For example, how does the heterogeneity influence the span width of the interface's most affect zone and is there an optimum one? Does dynamic interface behave similar as its counterpart in laminates? What's the best microstructure gradient to achieve the maximum mechanical performance? All these questions require sophisticated experimental design incorporated with theoretical mechanics concerns to arrive a satisfied answer.

REFERENCES

- [1] H. Gleiter, Nanostructured materials: basic concepts and microstructure, *Acta Materialia*. 48 (2000) 1–29. doi:10.1016/S1359-6454(99)00285-2.
- [2] M.A. Meyers, A. Mishra, D.J. Benson, Mechanical properties of nanocrystalline materials, *Progress in Materials Science*. 51 (2006) 427–556. doi:10.1016/j.pmatsci.2005.08.003.
- [3] R.W. Siegel, Nanostructured materials -mind over matter-, *Nanostructured Materials*. 3 (1993) 1–18. doi:10.1016/0965-9773(93)90058-J.
- [4] H. Gleiter, Nanocrystalline materials, *Progress in Materials Science*. 33 (1989) 223–315. doi:10.1016/0079-6425(89)90001-7.
- [5] M.J. Zehetbauer, Y.T. Zhu, eds., *Bulk Nanostructured Materials*, Wiley-VCH Verlag GmbH & Co. KGaA, Weinheim, Germany, 2009. <http://doi.wiley.com/10.1002/9783527626892> (accessed March 1, 2016).
- [6] L. Wang, J. Teng, P. Liu, A. Hirata, E. Ma, Z. Zhang, et al., Grain rotation mediated by grain boundary dislocations in nanocrystalline platinum, *Nature Communications*. 5 (2014). doi:10.1038/ncomms5402.
- [7] P.G. Sanders, J.A. Eastman, J.R. Weertman, Elastic and tensile behavior of nanocrystalline copper and palladium, *Acta Materialia*. 45 (1997) 4019–4025. doi:10.1016/S1359-6454(97)00092-X.
- [8] C.C. Koch, Y.S. Cho, Nanocrystals by high energy ball milling, *Nanostructured Materials*. 1 (1992) 207–212. doi:10.1016/0965-9773(92)90096-G.
- [9] S. Berger, R. Porat, R. Rosen, Nanocrystalline materials: A study of WC-based hard metals, *Progress in Materials Science*. 42 (1997) 311–320. doi:10.1016/S0079-6425(97)00021-2.
- [10] E. Edelberg, S. Bergh, R. Naone, M. Hall, E.S. Aydil, Visible luminescence from nanocrystalline silicon films produced by plasma enhanced chemical vapor deposition, *Applied Physics Letters*. 68 (1996) 1415. doi:10.1063/1.116098.
- [11] X. Ding, X. Liu, Synthesis and microstructure control of nanocrystalline titania powders via a sol—gel process, *Materials Science and Engineering: A*. 224 (1997) 210–215. doi:10.1016/S0921-5093(96)10541-4.

- [12] R. Valiev, Nanostructuring of metals by severe plastic deformation for advanced properties, *Nature Materials*. 3 (2004) 511–516. doi:10.1038/nmat1180.
- [13] R. Valiev, Y. Estrin, Z. Horita, T. Langdon, M. Zechetbauer, Y. Zhu, Producing bulk ultrafine-grained materials by severe plastic deformation, *JOM*. 58 (2006) 33–39. doi:10.1007/s11837-006-0213-7.
- [14] R.Z. Valiev, I.V. Alexandrov, Y.T. Zhu, T.C. Lowe, Paradox of Strength and Ductility in Metals Processed Bysevere Plastic Deformation, *Journal of Materials Research*. 17 (2002) 5–8. doi:10.1557/JMR.2002.0002.
- [15] R.Z. Valiev, T.G. Langdon, Principles of equal-channel angular pressing as a processing tool for grain refinement, *Prog. Mater. Sci.* 51 (2006) 881–981. doi:http://dx.doi.org/10.1016/j.pmatsci.2006.02.003.
- [16] A.P. Zhilyaev, T.G. Langdon, Using high-pressure torsion for metal processing: Fundamentals and applications, *Prog. Mater. Sci.* 53 (2008) 893–979. doi:http://dx.doi.org/10.1016/j.pmatsci.2008.03.002.
- [17] Y. Saito, H. Utsunomiya, N. Tsuji, T. Sakai, Novel ultra-high straining process for bulk materials—development of the accumulative roll-bonding (ARB) process, *Acta Materialia*. 47 (1999) 579–583. doi:10.1016/S1359-6454(98)00365-6.
- [18] C. Koch, Optimization of strength and ductility in nanocrystalline and ultrafine grained metals, *Scripta Materialia*. 49 (2003) 657–662. doi:10.1016/S1359-6462(03)00394-4.
- [19] C.C. Koch, Ductility in Nanostructured and Ultra Fine-Grained Materials: Recent Evidence for Optimism, *Journal of Metastable and Nanocrystalline Materials*. 18 (2003) 9–20. doi:10.4028/www.scientific.net/JMNM.18.9.
- [20] Y. Zhao, Y. Guo, Q. Wei, A. Dangelewicz, C. Xu, Y. Zhu, et al., Influence of specimen dimensions on the tensile behavior of ultrafine-grained Cu, *Scripta Materialia*. 59 (2008) 627–630. doi:10.1016/j.scriptamat.2008.05.031.
- [21] N. Hansen, Hall–Petch relation and boundary strengthening, *Scripta Materialia*. 51 (2004) 801–806. doi:10.1016/j.scriptamat.2004.06.002.
- [22] J.R. Weertman, Hall-Petch strengthening in nanocrystalline metals, *Materials Science and Engineering: A*. 166 (1993) 161–167. doi:10.1016/0921-5093(93)90319-A.

- [23] A.H. Chokshi, A. Rosen, J. Karch, H. Gleiter, On the validity of the hall-petch relationship in nanocrystalline materials, *Scripta Metallurgica*. 23 (1989) 1679–1683. doi:10.1016/0036-9748(89)90342-6.
- [24] G.E. Fougere, J.R. Weertman, R.W. Siegel, S. Kim, Grain-size dependent hardening and softening of nanocrystalline Cu and Pd, *Scripta Metallurgica et Materialia*. 26 (1992) 1879–1883. doi:10.1016/0956-716X(92)90052-G.
- [25] K. Lu, M.L. Sui, An explanation to the abnormal Hall-Petch relation in nanocrystalline materials, *Scripta Metallurgica et Materialia*. 28 (1993) 1465–1470. doi:10.1016/0956-716X(93)90576-E.
- [26] R.W. Hertzberg, R.P. Vinci, J.L. Hertzberg, *Deformation and fracture mechanics of engineering materials*, John Wiley & Sons, Inc., Hoboken, NJ, 2012. <http://public.ebib.com/choice/PublicFullRecord.aspx?p=2064702> (accessed January 28, 2016).
- [27] E. Ma, Instabilities and ductility of nanocrystalline and ultrafine-grained metals, *Scripta Materialia*. 49 (2003) 663–668. doi:10.1016/S1359-6462(03)00396-8.
- [28] J.R. Weertman, D. Farkas, K. Hemker, H. Kung, M. Mayo, R. Mitra, et al., Structure and Mechanical Behavior of Bulk Nanocrystalline Materials, *MRS Bulletin*. 24 (1999) 44–53. doi:10.1557/S088376940005154X.
- [29] K.M. Youssef, R.O. Scattergood, K.L. Murty, J.A. Horton, C.C. Koch, Ultrahigh strength and high ductility of bulk nanocrystalline copper, *Applied Physics Letters*. 87 (2005) 091904. doi:10.1063/1.2034122.
- [30] Y.T. Zhu, X. Liao, Nanostructured metals: Retaining ductility, *Nature Materials*. 3 (2004) 351–352. doi:10.1038/nmat1141.
- [31] P. Kumar, M. Kawasaki, T.G. Langdon, Review: Overcoming the paradox of strength and ductility in ultrafine-grained materials at low temperatures, *Journal of Materials Science*. 51 (2016) 7–18. doi:10.1007/s10853-015-9143-5.
- [32] D. Hull, D.J. Bacon, *Introduction to dislocations*, 5. ed, Elsevier/Butterworth-Heinemann, Amsterdam, 2011.
- [33] J.P. Hirth, J. Lothe, *Theory of dislocations*, Wiley, 1982.
- [34] G.D. Hughes, S.D. Smith, C.S. Pande, H.R. Johnson, R.W. Armstrong, Hall-petch strengthening for the microhardness of twelve nanometer grain diameter

- electrodeposited nickel, *Scripta Metallurgica*. 20 (1986) 93–97. doi:10.1016/0036-9748(86)90219-X.
- [35] C.S. Pande, R.A. Masumura, R.W. Armstrong, Pile-up based hall-petch relation for nanoscale materials, *Nanostructured Materials*. 2 (1993) 323–331. doi:10.1016/0965-9773(93)90159-9.
- [36] J.R. Trelewicz, C.A. Schuh, The Hall–Petch breakdown in nanocrystalline metals: A crossover to glass-like deformation, *Acta Materialia*. 55 (2007) 5948–5958. doi:10.1016/j.actamat.2007.07.020.
- [37] F. Louchet, J. Weiss, T. Richeton, Hall-Petch Law Revisited in Terms of Collective Dislocation Dynamics, *Physical Review Letters*. 97 (2006). doi:10.1103/PhysRevLett.97.075504.
- [38] Y. Harai, Y. Ito, Z. Horita, High-pressure torsion using ring specimens, *Scripta Materialia*. 58 (2008) 469–472. doi:10.1016/j.scriptamat.2007.10.037.
- [39] E. Ma, Eight routes to improve the tensile ductility of bulk nanostructured metals and alloys, *JOM*. 58 (2006) 49–53. doi:10.1007/s11837-006-0215-5.
- [40] E. Ma, Instabilities and ductility of nanocrystalline and ultrafine-grained metals, *Scripta Materialia*. 49 (2003) 663–668. doi:10.1016/S1359-6462(03)00396-8.
- [41] Y.T. Zhu, X.L. Wu, X.Z. Liao, J. Narayan, L.J. Kecskés, S.N. Mathaudhu, Dislocation–twin interactions in nanocrystalline fcc metals, *Acta Materialia*. 59 (2011) 812–821. doi:10.1016/j.actamat.2010.10.028.
- [42] Z. Shan, Grain Boundary-Mediated Plasticity in Nanocrystalline Nickel, *Science*. 305 (2004) 654–657. doi:10.1126/science.1098741.
- [43] Z.X. Wu, Y.W. Zhang, M.H. Jhon, D.J. Srolovitz, Anatomy of nanomaterial deformation: Grain boundary sliding, plasticity and cavitation in nanocrystalline Ni, *Acta Materialia*. 61 (2013) 5807–5820. doi:10.1016/j.actamat.2013.06.026.
- [44] H. Van Swygenhoven, M. Spaczer, A. Caro, D. Farkas, Competing plastic deformation mechanisms in nanophase metals, *Physical Review B*. 60 (1999) 22–25. doi:10.1103/PhysRevB.60.22.
- [45] A. Hasnaoui, H. Van Swygenhoven, P.M. Derlet, Cooperative processes during plastic deformation in nanocrystalline fcc metals: A molecular dynamics simulation, *Physical Review B*. 66 (2002). doi:10.1103/PhysRevB.66.184112.

- [46] V. Yamakov, D. Wolf, S.R. Phillpot, A.K. Mukherjee, H. Gleiter, Deformation-mechanism map for nanocrystalline metals by molecular-dynamics simulation, *Nature Materials*. 3 (2004) 43–47. doi:10.1038/nmat1035.
- [47] H. Van Swygenhoven, P.M. Derlet, Grain-boundary sliding in nanocrystalline fcc metals, *Physical Review B*. 64 (2001). doi:10.1103/PhysRevB.64.224105.
- [48] H. Hahn, P. Mondal, K.A. Padmanabhan, Plastic deformation of nanocrystalline materials, *Nanostructured Materials*. 9 (1997) 603–606. doi:10.1016/S0965-9773(97)00135-9.
- [49] J. Schiotz, F.D. Di Tolla, K.W. Jacobsen, Softening of nanocrystalline metals at very small grain sizes, *Nature*. 391 (1998) 561–563. doi:10.1038/35328.
- [50] Y. Ivanisenko, L. Kurmanaeva, J. Weissmueller, K. Yang, J. Markmann, H. Rösner, et al., Deformation mechanisms in nanocrystalline palladium at large strains, *Acta Materialia*. 57 (2009) 3391–3401. doi:10.1016/j.actamat.2009.03.049.
- [51] N.Q. Chinh, P. Szommer, Z. Horita, T.G. Langdon, Experimental Evidence for Grain-Boundary Sliding in Ultrafine-Grained Aluminum Processed by Severe Plastic Deformation, *Advanced Materials*. 18 (2006) 34–39. doi:10.1002/adma.200501232.
- [52] X. Han, L. Wang, Y. Yue, Z. Zhang, In situ atomic scale mechanical microscopy discovering the atomistic mechanisms of plasticity in nano-single crystals and grain rotation in polycrystalline metals, *Ultramicroscopy*. 151 (2015) 94–100. doi:10.1016/j.ultramic.2014.11.035.
- [53] A.V. Sergueeva, N.A. Mara, N.A. Krasilnikov, R.Z. Valiev, A.K. Mukherjee, Cooperative grain boundary sliding in nanocrystalline materials, *Philosophical Magazine*. 86 (2006) 5797–5804. doi:10.1080/14786430600764906.
- [54] Y.B. Wang, M.L. Sui, E. Ma, *In situ* observation of twin boundary migration in copper with nanoscale twins during tensile deformation, *Philosophical Magazine Letters*. 87 (2007) 935–942. doi:10.1080/09500830701591493.
- [55] H. Van Swygenhoven, P.M. Derlet, A. Hasnaoui, Atomic mechanism for dislocation emission from nanosized grain boundaries, *Physical Review B*. 66 (2002). doi:10.1103/PhysRevB.66.024101.
- [56] P.M. Derlet, H. Van Swygenhoven†, A. Hasnaoui, Atomistic simulation of dislocation emission in nanosized grain boundaries, *Philosophical Magazine*. 83 (2003) 3569–3575. doi:10.1080/14786430310001599397.

- [57] X.Z. Liao, F. Zhou, E.J. Lavernia, S.G. Srinivasan, M.I. Baskes, D.W. He, et al., Deformation mechanism in nanocrystalline Al: Partial dislocation slip, *Applied Physics Letters*. 83 (2003) 632. doi:10.1063/1.1594836.
- [58] X.Z. Liao, Y.H. Zhao, S.G. Srinivasan, Y.T. Zhu, R.Z. Valiev, D.V. Gunderov, Deformation twinning in nanocrystalline copper at room temperature and low strain rate, *Applied Physics Letters*. 84 (2004) 592. doi:10.1063/1.1644051.
- [59] I.A. Ovid'ko, N.V. Skiba, Enhanced dislocation emission from grain boundaries in nanocrystalline materials, *Scripta Materialia*. 67 (2012) 13–16. doi:10.1016/j.scriptamat.2012.03.007.
- [60] V. Yamakov, D. Wolf, S.R. Phillpot, A.K. Mukherjee, H. Gleiter, Dislocation processes in the deformation of nanocrystalline aluminium by molecular-dynamics simulation, *Nature Materials*. 1 (2002) 45–49. doi:10.1038/nmat700.
- [61] L. Wang, X. Han, P. Liu, Y. Yue, Z. Zhang, E. Ma, *In Situ* Observation of Dislocation Behavior in Nanometer Grains, *Physical Review Letters*. 105 (2010). doi:10.1103/PhysRevLett.105.135501.
- [62] Z.W. Shan, J.M.K. Wiezorek, E.A. Stach, D.M. Follstaedt, J.A. Knapp, S.X. Mao, Dislocation Dynamics in Nanocrystalline Nickel, *Physical Review Letters*. 98 (2007). doi:10.1103/PhysRevLett.98.095502.
- [63] Z. Budrovic, Plastic Deformation with Reversible Peak Broadening in Nanocrystalline Nickel, *Science*. 304 (2004) 273–276. doi:10.1126/science.1095071.
- [64] X.L. Wu, Y.T. Zhu, Y.G. Wei, Q. Wei, Strong Strain Hardening in Nanocrystalline Nickel, *Physical Review Letters*. 103 (2009). doi:10.1103/PhysRevLett.103.205504.
- [65] M. Ke, S.A. Hackney, W.W. Milligan, E.C. Aifantis, Observation and measurement of grain rotation and plastic strain in nanostructured metal thin films, *Nanostructured Materials*. 5 (1995) 689–697. doi:10.1016/0965-9773(95)00281-I.
- [66] Z. Shan, J.M.K. Wiezorek, J.A. Knapp, D.M. Follstaedt, E.A. Stach, S.X. Mao, Large lattice strain in individual grains of deformed nanocrystalline Ni, *Applied Physics Letters*. 92 (2008) 091917. doi:10.1063/1.2889936.
- [67] M.Y. Gutkin, I.A. Ovid'ko, N.V. Skiba, Crossover from grain boundary sliding to rotational deformation in nanocrystalline materials, *Acta Materialia*. 51 (2003) 4059–4071. doi:10.1016/S1359-6454(03)00226-X.

- [68] M.Y. Gutkin, I.A. Ovid'ko, Grain boundary migration as rotational deformation mode in nanocrystalline materials, *Applied Physics Letters*. 87 (2005) 251916. doi:10.1063/1.2147721.
- [69] M.G. Zelin, A.K. Mukherjee, Geometrical aspects of superplastic flow, *Materials Science and Engineering: A*. 208 (1996) 210–225. doi:10.1016/0921-5093(95)10080-6.
- [70] F.R.N. Nabarro, Steady-state diffusional creep, *Philosophical Magazine*. 16 (1967) 231–237. doi:10.1080/14786436708229736.
- [71] G.J. Fan, L.F. Fu, Y.D. Wang, Y. Ren, H. Choo, P.K. Liaw, et al., Uniaxial tensile plastic deformation of a bulk nanocrystalline alloy studied by a high-energy x-ray diffraction technique, *Applied Physics Letters*. 89 (2006) 101918. doi:10.1063/1.2348783.
- [72] B. Yang, H. Vehoff, A. Hohenwarter, M. Hafok, R. Pippan, Strain effects on the coarsening and softening of electrodeposited nanocrystalline Ni subjected to high pressure torsion, *Scripta Materialia*. 58 (2008) 790–793. doi:10.1016/j.scriptamat.2007.12.039.
- [73] Y.B. Wang, J.C. Ho, X.Z. Liao, H.Q. Li, S.P. Ringer, Y.T. Zhu, Mechanism of grain growth during severe plastic deformation of a nanocrystalline Ni–Fe alloy, *Applied Physics Letters*. 94 (2009) 011908. doi:10.1063/1.3065025.
- [74] X.Z. Liao, A.R. Kilmametov, R.Z. Valiev, H. Gao, X. Li, A.K. Mukherjee, et al., High-pressure torsion-induced grain growth in electrodeposited nanocrystalline Ni, *Applied Physics Letters*. 88 (2006) 021909. doi:10.1063/1.2159088.
- [75] T.H. Fang, W.L. Li, N.R. Tao, K. Lu, Revealing Extraordinary Intrinsic Tensile Plasticity in Gradient Nano-Grained Copper, *Science*. 331 (2011) 1587–1590. doi:10.1126/science.1200177.
- [76] K. Zhang, J.R. Weertman, J.A. Eastman, The influence of time, temperature, and grain size on indentation creep in high-purity nanocrystalline and ultrafine grain copper, *Applied Physics Letters*. 85 (2004) 5197. doi:10.1063/1.1828213.
- [77] K. Zhang, J.R. Weertman, J.A. Eastman, Rapid stress-driven grain coarsening in nanocrystalline Cu at ambient and cryogenic temperatures, *Applied Physics Letters*. 87 (2005) 061921. doi:10.1063/1.2008377.
- [78] J.C.M. Li, Mechanical Grain Growth in Nanocrystalline Copper, *Physical Review Letters*. 96 (2006). doi:10.1103/PhysRevLett.96.215506.

- [79] A.J. Haslam, D. Moldovan, V. Yamakov, D. Wolf, S.R. Phillpot, H. Gleiter, Stress-enhanced grain growth in a nanocrystalline material by molecular-dynamics simulation, *Acta Materialia*. 51 (2003) 2097–2112. doi:10.1016/S1359-6454(03)00011-9.
- [80] J.W. Christian, S. Mahajan, Deformation twinning, *Prog. Mater. Sci.* 39 (1995) 1–157. doi:http://dx.doi.org/10.1016/0079-6425(94)00007-7.
- [81] L. Capolungo, I.J. Beyerlein, Nucleation and stability of twins in hcp metals, *Physical Review B*. 78 (2008). doi:10.1103/PhysRevB.78.024117.
- [82] J. Wang, R.G. Hoagland, J.P. Hirth, L. Capolungo, I.J. Beyerlein, C.N. Tomé, Nucleation of a $(1\bar{1}0)_{12}$ twin in hexagonal close-packed crystals, *Scripta Materialia*. 61 (2009) 903–906. doi:10.1016/j.scriptamat.2009.07.028.
- [83] Y.T. Zhu, X.Z. Liao, X.L. Wu, Deformation twinning in nanocrystalline materials, *Prog. Mater. Sci.* 57 (2012) 1–62. doi:10.1016/j.pmatsci.2011.05.001.
- [84] B.Q. Li, M.L. Sui, B. Li, E. Ma, S.X. Mao, Reversible Twinning in Pure Aluminum, *Physical Review Letters*. 102 (2009). doi:10.1103/PhysRevLett.102.205504.
- [85] Y. Wang, M. Chen, F. Zhou, E. Ma, High tensile ductility in a nanostructured metal, *Nature*. 419 (2002) 912–915. doi:10.1038/nature01133.
- [86] L. Kubin, A. Mortensen, Geometrically necessary dislocations and strain-gradient plasticity: a few critical issues, *Scripta Materialia*. 48 (2003) 119–125. doi:10.1016/S1359-6462(02)00335-4.
- [87] H. Gao, Mechanism-based strain gradient plasticity? I. Theory, *Journal of the Mechanics and Physics of Solids*. 47 (1999) 1239–1263. doi:10.1016/S0022-5096(98)00103-3.
- [88] B.B. Sun, M.L. Sui, Y.M. Wang, G. He, J. Eckert, E. Ma, Ultrafine composite microstructure in a bulk Ti alloy for high strength, strain hardening and tensile ductility, *Acta Materialia*. 54 (2006) 1349–1357. doi:10.1016/j.actamat.2005.11.011.
- [89] K. Lu, Making strong nanomaterials ductile with gradients, *Science*. 345 (2014) 1455–1456. doi:10.1126/science.1255940.
- [90] Y.H. Zhao, X.Z. Liao, S. Cheng, E. Ma, Y.T. Zhu, Simultaneously Increasing the Ductility and Strength of Nanostructured Alloys, *Advanced Materials*. 18 (2006) 2280–2283. doi:10.1002/adma.200600310.

- [91] R.Z. Valiev, N.A. Enikeev, M.Y. Murashkin, V.U. Kazykhanov, X. Sauvage, On the origin of the extremely high strength of ultrafine-grained Al alloys produced by severe plastic deformation, *Scripta Materialia*. 63 (2010) 949–952. doi:10.1016/j.scriptamat.2010.07.014.
- [92] Y. Zhao, Y. Zhu, E.J. Lavernia, Strategies for Improving Tensile Ductility of Bulk Nanostructured Materials, *Advanced Engineering Materials*. 12 (2010) 769–778. doi:10.1002/adem.200900335.
- [93] R.Z. Valiev, Y. Estrin, Z. Horita, T.G. Langdon, M.J. Zehetbauer, Y.T. Zhu, Fundamentals of Superior Properties in Bulk NanoSPD Materials, *Materials Research Letters*. 4 (2016) 1–21. doi:10.1080/21663831.2015.1060543.
- [94] L. Lu, Ultrahigh Strength and High Electrical Conductivity in Copper, *Science*. 304 (2004) 422–426. doi:10.1126/science.1092905.
- [95] E. Ma, Y.M. Wang, Q.H. Lu, M.L. Sui, L. Lu, K. Lu, Strain hardening and large tensile elongation in ultrahigh-strength nano-twinned copper, *Applied Physics Letters*. 85 (2004) 4932. doi:10.1063/1.1814431.
- [96] Y.H. Zhao, Y.T. Zhu, X.Z. Liao, Z. Horita, T.G. Langdon, Tailoring stacking fault energy for high ductility and high strength in ultrafine grained Cu and its alloy, *Applied Physics Letters*. 89 (2006) 121906. doi:10.1063/1.2356310.
- [97] K. Lu, L. Lu, S. Suresh, Strengthening Materials by Engineering Coherent Internal Boundaries at the Nanoscale, *Science*. 324 (2009) 349–352. doi:10.1126/science.1159610.
- [98] T. Zhu, J. Li, A. Samanta, H.G. Kim, S. Suresh, Interfacial plasticity governs strain rate sensitivity and ductility in nanostructured metals, *Proceedings of the National Academy of Sciences*. 104 (2007) 3031–3036. doi:10.1073/pnas.0611097104.
- [99] M. Dao, L. Lu, Y.F. Shen, S. Suresh, Strength, strain-rate sensitivity and ductility of copper with nanoscale twins, *Acta Materialia*. 54 (2006) 5421–5432. doi:10.1016/j.actamat.2006.06.062.
- [100] Y.T. Zhu, X.Z. Liao, X.L. Wu, Deformation twinning in nanocrystalline materials, *Progress in Materials Science*. 57 (2012) 1–62. doi:10.1016/j.pmatsci.2011.05.001.
- [101] Y.T. Zhu, X.Z. Liao, X.L. Wu, Deformation twinning in bulk nanocrystalline metals: Experimental observations, *JOM*. 60 (2008) 60–64. doi:10.1007/s11837-008-0120-1.

- [102] X.L. Wu, X.Z. Liao, S.G. Srinivasan, F. Zhou, E.J. Lavernia, R.Z. Valiev, et al., New Deformation Twinning Mechanism Generates Zero Macroscopic Strain in Nanocrystalline Metals, *Physical Review Letters*. 100 (2008). doi:10.1103/PhysRevLett.100.095701.
- [103] X. Ma, Y. Zhu, Deformation Twinning in Nanocrystalline Metals, in: Reference Module in Materials Science and Materials Engineering, Elsevier, 2016. <http://linkinghub.elsevier.com/retrieve/pii/B9780128035818039904> (accessed February 9, 2016).
- [104] C.X. Huang, K. Wang, S.D. Wu, Z.F. Zhang, G.Y. Li, S.X. Li, Deformation twinning in polycrystalline copper at room temperature and low strain rate, *Acta Materialia*. 54 (2006) 655–665. doi:10.1016/j.actamat.2005.10.002.
- [105] M.A. Meyers, O. Vöhringer, V.A. Lubarda, The onset of twinning in metals: a constitutive description, *Acta Materialia*. 49 (2001) 4025–4039. doi:10.1016/S1359-6454(01)00300-7.
- [106] X.L. Wu, Y.T. Zhu, Inverse Grain-Size Effect on Twinning in Nanocrystalline Ni, *Physical Review Letters*. 101 (2008). doi:10.1103/PhysRevLett.101.025503.
- [107] J.. Zhang, G. Liu, R.H. Wang, J. Li, J. Sun, E. Ma, Double-inverse grain size dependence of deformation twinning in nanocrystalline Cu, *Physical Review B*. 81 (2010). doi:10.1103/PhysRevB.81.172104.
- [108] K. Youssef, M. Sakaliyska, H. Bahmanpour, R. Scattergood, C. Koch, Effect of stacking fault energy on mechanical behavior of bulk nanocrystalline Cu and Cu alloys, *Acta Materialia*. 59 (2011) 5758–5764. doi:10.1016/j.actamat.2011.05.052.
- [109] H. Bahmanpour, K.M. Youssef, J. Horáky, D. Setman, M.A. Atwater, M.J. Zehetbauer, et al., Deformation twins and related softening behavior in nanocrystalline Cu–30% Zn alloy, *Acta Materialia*. 60 (2012) 3340–3349. doi:10.1016/j.actamat.2012.02.036.
- [110] Y.T. Zhu, X.Z. Liao, X.L. Wu, J. Narayan, Grain size effect on deformation twinning and detwinning, *Journal of Materials Science*. 48 (2013) 4467–4475. doi:10.1007/s10853-013-7140-0.
- [111] Q. Yu, Z. Shan W., J. Li, X. Huang, L. Xiao, J. Sun, et al., Strong crystal size effect on deformation twinning, *Nature*. 463 (2010) 335–338. doi:10.1038/nature08692.
- [112] M. Chen, E. Ma, K.J. Hemker, H.. Sheng, Y.. Wang, X.. Cheng, Deformation Twinning in Nanocrystalline Aluminum, *Science*. 300 (2003) 1275–1277. doi:10.1126/science.1083727.

- [113] X.Z. Liao, J.Y. Huang, Y.T. Zhu, F. Zhou, E.J. Lavernia, Nanostructures and deformation mechanisms in a cryogenically ball-milled Al-Mg alloy, *Philosophical Magazine*. 83 (2003) 3065–3075. doi:10.1080/1478643031000152799.
- [114] H.V. Swygenhoven, P.M. Derlet, A.G. Frøseth, Stacking fault energies and slip in nanocrystalline metals, *Nature Materials*. 3 (2004) 399–403. doi:10.1038/nmat1136.
- [115] V. Yamakov, D. Wolf, S.R. Phillpot, A.K. Mukherjee, H. Gleiter, Deformation-mechanism map for nanocrystalline metals by molecular-dynamics simulation, *Nature Materials*. 3 (2004) 43–47. doi:10.1038/nmat1035.
- [116] X.L. Wu, Y.T. Zhu, Inverse Grain-Size Effect on Twinning in Nanocrystalline Ni, *Physical Review Letters*. 101 (2008). doi:10.1103/PhysRevLett.101.025503.
- [117] S. Cheng, A.D. Stoica, X.L. Wang, Y. Ren, J. Almer, J.A. Horton, et al., Deformation Crossover: From Nano- to Mesoscale, *Physical Review Letters*. 103 (2009). doi:10.1103/PhysRevLett.103.035502.
- [118] R.J. McCabe, I.J. Beyerlein, J.S. Carpenter, N.A. Mara, The critical role of grain orientation and applied stress in nanoscale twinning, *Nature Communications*. 5 (2014). doi:10.1038/ncomms4806.
- [119] L. Li, T. Ungár, Y.D. Wang, J.R. Morris, G. Tichy, J. Lendvai, et al., Microstructure evolution during cold rolling in a nanocrystalline Ni–Fe alloy determined by synchrotron X-ray diffraction, *Acta Materialia*. 57 (2009) 4988–5000. doi:10.1016/j.actamat.2009.07.002.
- [120] V. Yamakov, D. Wolf, S.R. Phillpot, H. Gleiter, Dislocation–dislocation and dislocation–twin reactions in nanocrystalline Al by molecular dynamics simulation, *Acta Materialia*. 51 (2003) 4135–4147. doi:10.1016/S1359-6454(03)00232-5.
- [121] S. Ni, Y.B. Wang, X.Z. Liao, H.Q. Li, R.B. Figueiredo, S.P. Ringer, et al., Effect of grain size on the competition between twinning and detwinning in nanocrystalline metals, *Physical Review B*. 84 (2011). doi:10.1103/PhysRevB.84.235401.
- [122] J.W. Christian, S. Mahajan, Deformation twinning, *Progress in Materials Science*. 39 (1995) 1–157. doi:10.1016/0079-6425(94)00007-7.
- [123] M. Niewczas, G. Saada, Twinning nucleation in Cu-8 at. % Al single crystals, *Philosophical Magazine A*. 82 (2002) 167–191. doi:10.1080/01418610208240003.

- [124] Z.W. Shan, E.A. Stach, J.M. Wiezorek, J.A. Knapp, D.M. Follstaedt, S.X. Mao, Grain Boundary-Mediated Plasticity in Nanocrystalline Nickel, *Science*. 305 (2004) 654–657. doi:10.1126/science.1098741.
- [125] Y.T. Zhu, X.Z. Liao, S.G. Srinivasan, Y.H. Zhao, M.I. Baskes, F. Zhou, et al., Nucleation and growth of deformation twins in nanocrystalline aluminum, *Applied Physics Letters*. 85 (2004) 5049. doi:10.1063/1.1823042.
- [126] Y.T. Zhu, X.Z. Liao, S.G. Srinivasan, E.J. Lavernia, Nucleation of deformation twins in nanocrystalline face-centered-cubic metals processed by severe plastic deformation, *Journal of Applied Physics*. 98 (2005) 034319. doi:10.1063/1.2006974.
- [127] X.L. Wu, Y.T. Zhu, M.W. Chen, E. Ma, Twinning and stacking fault formation during tensile deformation of nanocrystalline Ni, *Scripta Materialia*. 54 (2006) 1685–1690. doi:10.1016/j.scriptamat.2005.12.045.
- [128] H.V. Swygenhoven, *Polycrystalline Materials: Grain Boundaries and Dislocations*, *Science*. 296 (2002) 66–67. doi:10.1126/science.1071040.
- [129] Y.T. Zhu, X.Z. Liao, X.L. Wu, J. Narayan, Grain size effect on deformation twinning and detwinning, *Journal of Materials Science*. 48 (2013) 4467–4475. doi:10.1007/s10853-013-7140-0.
- [130] X.L. Wu, X.Z. Liao, S.G. Srinivasan, F. Zhou, E.J. Lavernia, R.Z. Valiev, et al., New Deformation Twinning Mechanism Generates Zero Macroscopic Strain in Nanocrystalline Metals, *Physical Review Letters*. 100 (2008). doi:10.1103/PhysRevLett.100.095701.
- [131] X.H. An, M. Song, Y. Huang, X.Z. Liao, S.P. Ringer, T.G. Langdon, et al., Twinning via the motion of incoherent twin boundaries nucleated at grain boundaries in a nanocrystalline Cu alloy, *Scripta Materialia*. 72-73 (2014) 35–38. doi:10.1016/j.scriptamat.2013.10.014.
- [132] J.Y. Zhang, P. Zhang, R.H. Wang, G. Liu, G.J. Zhang, J. Sun, Grain-size-dependent zero-strain mechanism for twinning in copper, *Physical Review B*. 86 (2012). doi:10.1103/PhysRevB.86.064110.
- [133] Wu, S.G. Srinivasan, F. Zhou, E.J. Lavernia, R.Z. Valiev, Y.T. Zhu, New Deformation Twinning Mechanism Generates Zero Macroscopic Strain in Nanocrystalline Metals, *Physical Review Letters*. 100 (2008). doi:10.1103/PhysRevLett.100.095701.

- [134] X. Li, Y. Wei, L. Lu, K. Lu, H. Gao, Dislocation nucleation governed softening and maximum strength in nano-twinned metals, *Nature*. 464 (2010) 877–880. doi:10.1038/nature08929.
- [135] I.J. Beyerlein, X. Zhang, A. Misra, Growth Twins and Deformation Twins in Metals, *Annual Review of Materials Research*. 44 (2014) 329–363. doi:10.1146/annurev-matsci-070813-113304.
- [136] J. Wang, H. Huang, Shockley partial dislocations to twin: Another formation mechanism and generic driving force, *Applied Physics Letters*. 85 (2004) 5983. doi:10.1063/1.1835549.
- [137] M.A. Meyers, A. Mishra, D.J. Benson, Mechanical properties of nanocrystalline materials, *Progress in Materials Science*. 51 (2006) 427–556. doi:10.1016/j.pmatsci.2005.08.003.
- [138] J. Wang, N. Li, O. Anderoglu, X. Zhang, A. Misra, J.Y. Huang, et al., Detwinning mechanisms for growth twins in face-centered cubic metals, *Acta Materialia*. 58 (2010) 2262–2270. doi:10.1016/j.actamat.2009.12.013.
- [139] J. Wang, A. Misra, J.P. Hirth, Shear response of $\Sigma 3 \{112\}$ twin boundaries in face-centered-cubic metals, *Physical Review B*. 83 (2011). doi:10.1103/PhysRevB.83.064106.
- [140] L. Liu, J. Wang, S.K. Gong, S.X. Mao, High Resolution Transmission Electron Microscope Observation of Zero-Strain Deformation Twinning Mechanisms in Ag, *Physical Review Letters*. 106 (2011). doi:10.1103/PhysRevLett.106.175504.
- [141] B.Q. Li, B. Li, Y.B. Wang, M.L. Sui, E. Ma, Twinning mechanism via synchronized activation of partial dislocations in face-centered-cubic materials, *Scripta Materialia*. 64 (2011) 852–855. doi:10.1016/j.scriptamat.2011.01.016.
- [142] F. Wu, Y.T. Zhu, J. Narayan, Macroscopic Twinning Strain in Nanocrystalline Cu, *Materials Research Letters*. 2 (2014) 63–69. doi:10.1080/21663831.2013.862874.
- [143] M.A. Meyers, P.-Y. Chen, A.Y.-M. Lin, Y. Seki, Biological materials: Structure and mechanical properties, *Progress in Materials Science*. 53 (2008) 1–206. doi:10.1016/j.pmatsci.2007.05.002.
- [144] M.A. Meyers, J. McKittrick, P.-Y. Chen, Structural Biological Materials: Critical Mechanics-Materials Connections, *Science*. 339 (2013) 773–779. doi:10.1126/science.1220854.

- [145] L. Li, C. Ortiz, Pervasive nanoscale deformation twinning as a catalyst for efficient energy dissipation in a bioceramic armour, *Nature Materials*. 13 (2014) 501–507. doi:10.1038/nmat3920.
- [146] B.J.F. Bruet, J. Song, M.C. Boyce, C. Ortiz, Materials design principles of ancient fish armour, *Nature Materials*. 7 (2008) 748–756. doi:10.1038/nmat2231.
- [147] X. Wu, P. Jiang, L. Chen, F. Yuan, Y.T. Zhu, Extraordinary strain hardening by gradient structure, *Proceedings of the National Academy of Sciences*. 111 (2014) 7197–7201. doi:10.1073/pnas.1324069111.
- [148] S. Suresh, Graded Materials for Resistance to Contact Deformation and Damage, *Science*. 292 (2001) 2447–2451. doi:10.1126/science.1059716.
- [149] T.S. Hussey, M.J. Koczak, R.W. Smith, S.R. Kalidindi, Synthesis of nickel aluminides by vacuum plasma spraying and exothermic in-situ reactions, *Materials Science and Engineering: A*. 229 (1997) 137–146. doi:10.1016/S0921-5093(97)80109-8.
- [150] Z. Xia, J. Liu, S. Zhu, Y. Zhao, Fabrication of laminated metal–intermetallic composites by interlayer in-situ reaction, *Journal of Materials Science*. 34 (n.d.) 3731–3735. doi:10.1023/A:1004624012683.
- [151] B.P. Bewlay, M.R. Jackson, H.A. Lipsitt, The balance of mechanical and environmental properties of a multielement niobium-niobium silicide-based In Situ composite, *Metallurgical and Materials Transactions A*. 27 (1996) 3801–3808. doi:10.1007/BF02595629.
- [152] F. Ding, L. Jia, S. Yuan, L. Su, J. Weng, H. Zhang, Microstructure evolution of a hypereutectic Nb–Ti–Si–Cr–Al–Hf alloy processed by directional solidification, *Chinese Journal of Aeronautics*. 27 (2014) 438–444. doi:10.1016/j.cja.2013.07.032.
- [153] W.A. Zinsser, J.J. Lewandowski, Effects of R-ratio on the fatigue crack growth of Nb–Si(ss) and Nb–10Si In Situ composites, *Metallurgical and Materials Transactions A*. 29 (1998) 1749–1757. doi:10.1007/s11661-998-0098-x.
- [154] Y. Chen, Y. Liu, E.G. Fu, C. Sun, K.Y. Yu, M. Song, et al., Unusual size-dependent strengthening mechanisms in helium ion-irradiated immiscible coherent Cu/Co nanolayers, *Acta Materialia*. 84 (2015) 393–404. doi:10.1016/j.actamat.2014.10.061.
- [155] Y. Chen, E. Fu, K. Yu, M. Song, Y. Liu, Y. Wang, et al., Enhanced radiation tolerance in immiscible Cu/Fe multilayers with coherent and incoherent layer interfaces, *Journal of Materials Research*. 30 (2015) 1300–1309. doi:10.1557/jmr.2015.24.

- [156] D.J. Lee, D.-H. Ahn, E.Y. Yoon, S.I. Hong, S. Lee, H.S. Kim, Estimating interface bonding strength in clad metals using digital image correlation, *Scripta Materialia*. 68 (2013) 893–896. doi:10.1016/j.scriptamat.2013.02.021.
- [157] J.S. Ha, S.I. Hong, Design of high strength Cu alloy interlayer for mechanical bonding Ti to steel and characterization of their tri-layered clad, *Materials & Design*. 51 (2013) 293–299. doi:10.1016/j.matdes.2013.04.068.
- [158] S. Mueller, L.M. Volpone, Friction stir welding of steel/aluminium sandwich panels, *Welding International*. 23 (2009) 699–705. doi:10.1080/09507110902843222.
- [159] X.L. Ma, C.X. Huang, W.Z. Xu, H. Zhou, X.L. Wu, Y.T. Zhu, Strain hardening and ductility in a coarse-grain/nanostructure laminate material, *Scripta Materialia*. 103 (2015) 57–60. doi:10.1016/j.scriptamat.2015.03.006.
- [160] I.J. Beyerlein, J.R. Mayeur, S. Zheng, N.A. Mara, J. Wang, A. Misra, Emergence of stable interfaces under extreme plastic deformation, *Proceedings of the National Academy of Sciences*. 111 (2014) 4386–4390. doi:10.1073/pnas.1319436111.
- [161] N. Tsuji, Y. Saito, S.-H. Lee, Y. Minamino, ARB (Accumulative Roll-Bonding) and other new Techniques to Produce Bulk Ultrafine Grained Materials, *Advanced Engineering Materials*. 5 (2003) 338–344. doi:10.1002/adem.200310077.
- [162] S. Ohsaki, S. Kato, N. Tsuji, T. Ohkubo, K. Hono, Bulk mechanical alloying of Cu–Ag and Cu/Zr two-phase microstructures by accumulative roll-bonding process, *Acta Materialia*. 55 (2007) 2885–2895. doi:10.1016/j.actamat.2006.12.027.
- [163] M.T. Pérez-Prado, del Valle, O.A. Ruano, Grain refinement of Mg–Al–Zn alloys via accumulative roll bonding, *Scripta Materialia*. 51 (2004) 1093–1097. doi:10.1016/j.scriptamat.2004.07.028.
- [164] S.. Lee, Y. Saito, T. Sakai, H. Utsunomiya, Microstructures and mechanical properties of 6061 aluminum alloy processed by accumulative roll-bonding, *Materials Science and Engineering: A*. 325 (2002) 228–235. doi:10.1016/S0921-5093(01)01416-2.
- [165] N. Takata, K. Yamada, K. Ikeda, F. Yoshida, H. Nakashima, N. Tsuji, Change in Microstructure and Texture during Annealing of Pure Copper Heavily Deformed by Accumulative Roll Bonding, *MATERIALS TRANSACTIONS*. 48 (2007) 2043–2048. doi:10.2320/matertrans.MA200701.
- [166] M. Kobayashi, T. Matsui, Y. Murakami, Mechanism of creation of compressive residual stress by shot peening, *International Journal of Fatigue*. 20 (1998) 351–357. doi:10.1016/S0142-1123(98)00002-4.

- [167] N.. Tao, M.. Sui, J. Lu, K. Lua, Surface nanocrystallization of iron induced by ultrasonic shot peening, *Nanostructured Materials*. 11 (1999) 433–440. doi:10.1016/S0965-9773(99)00324-4.
- [168] J.L. Ke LU, Surface Nanocrystallization (SNC) of Metallic Materials-Presentation of the Concept behind a New Approach, *Journal of Materials Sciences and Technology*. 15 (1999) 193.
- [169] H.L. Chan, H.H. Ruan, A.Y. Chen, J. Lu, Optimization of the strain rate to achieve exceptional mechanical properties of 304 stainless steel using high speed ultrasonic surface mechanical attrition treatment, *Acta Materialia*. 58 (2010) 5086–5096. doi:10.1016/j.actamat.2010.05.044.
- [170] S. Bagheri, M. Guagliano, Review of shot peening processes to obtain nanocrystalline surfaces in metal alloys, *Surface Engineering*. 25 (2009) 3–14. doi:10.1179/026708408X334087.
- [171] Y. Todaka, M. Umemoto, K. Tsuchiya, Comparison of nanocrystalline surface layer in steels formed by air blast and ultrasonic shot peening, *Materials Transactions*. 45 (2004) 376–379.
- [172] T. Balusamy, S. Kumar, T.S.N. Sankara Narayanan, Effect of surface nanocrystallization on the corrosion behaviour of AISI 409 stainless steel, *Corrosion Science*. 52 (2010) 3826–3834. doi:10.1016/j.corsci.2010.07.004.
- [173] B. Arifvianto, Suyitno, M. Mahardika, P. Dewo, P.T. Iswanto, U.A. Salim, Effect of surface mechanical attrition treatment (SMAT) on microhardness, surface roughness and wettability of AISI 316L, *Materials Chemistry and Physics*. 125 (2011) 418–426. doi:10.1016/j.matchemphys.2010.10.038.
- [174] W.L. Li, N.R. Tao, K. Lu, Fabrication of a gradient nano-micro-structured surface layer on bulk copper by means of a surface mechanical grinding treatment, *Scripta Materialia*. 59 (2008) 546–549. doi:10.1016/j.scriptamat.2008.05.003.
- [175] X.C. Liu, H.W. Zhang, K. Lu, Strain-Induced Ultrahard and Ultrastable Nanolaminated Structure in Nickel, *Science*. 342 (2013) 337–340. doi:10.1126/science.1242578.
- [176] H.W. Huang, Z.B. Wang, X.P. Yong, K. Lu, Enhancing torsion fatigue behaviour of a martensitic stainless steel by generating gradient nanograined layer via surface mechanical grinding treatment, *Materials Science and Technology*. 29 (2013) 1200–1205. doi:10.1179/1743284712Y.0000000192.

- [177] X.C. Liu, H.W. Zhang, K. Lu, Formation of nanolaminated structure in an interstitial-free steel, *Scripta Materialia*. 95 (2015) 54–57. doi:10.1016/j.scriptamat.2014.10.003.
- [178] D.A. Hughes, N. Hansen, Graded Nanostructures Produced by Sliding and Exhibiting Universal Behavior, *Physical Review Letters*. 87 (2001). doi:10.1103/PhysRevLett.87.135503.
- [179] M. Sato, T. Tsugita, T. Oshima, S. Sakata, K. Iwasaki, T. Matsuda, et al., Development of workstation-based CAMAC data acquisition system for JT-60 data processing system, *Fusion Engineering and Design*. 71 (2004) 145–149. doi:10.1016/j.fusengdes.2004.04.026.
- [180] R.S. Mishra, Z.Y. Ma, Friction stir welding and processing, *Materials Science and Engineering: R: Reports*. 50 (2005) 1–78. doi:10.1016/j.mser.2005.07.001.
- [181] N.A. Mara, I.J. Beyerlein, Review: effect of bimetal interface structure on the mechanical behavior of Cu–Nb fcc–bcc nanolayered composites, *Journal of Materials Science*. 49 (2014) 6497–6516. doi:10.1007/s10853-014-8342-9.
- [182] J.S. Carpenter, R.J. McCabe, S.J. Zheng, T.A. Wynn, N.A. Mara, I.J. Beyerlein, Processing Parameter Influence on Texture and Microstructural Evolution in Cu-Nb Multilayer Composites Fabricated via Accumulative Roll Bonding, *Metallurgical and Materials Transactions A*. 45 (2014) 2192–2208. doi:10.1007/s11661-013-2162-4.
- [183] M. Eizadjou, A. Kazemitalachi, H. Daneshmanesh, H. Shakurshahabi, K. Janghorban, Investigation of structure and mechanical properties of multi-layered Al/Cu composite produced by accumulative roll bonding (ARB) process, *Composites Science and Technology*. 68 (2008) 2003–2009. doi:10.1016/j.compscitech.2008.02.029.
- [184] M. Ruppert, C. Schunk, D. Hausmann, H.W. Höppel, M. Göken, Global and local strain rate sensitivity of bimodal Al-laminates produced by accumulative roll bonding, *Acta Materialia*. 103 (2016) 643–650. doi:10.1016/j.actamat.2015.11.009.
- [185] N.E. Mahallawy, A. Fathy, W. Abdelaziem, M. Hassan, Microstructure evolution and mechanical properties of Al/Al–12%Si multilayer processed by accumulative roll bonding (ARB), *Materials Science and Engineering: A*. 647 (2015) 127–135. doi:10.1016/j.msea.2015.08.064.
- [186] A. Mozaffari, H. Danesh Manesh, K. Janghorban, Evaluation of mechanical properties and structure of multilayered Al/Ni composites produced by accumulative roll bonding (ARB) process, *Journal of Alloys and Compounds*. 489 (2010) 103–109. doi:10.1016/j.jallcom.2009.09.022.

- [187] M. Alizadeh, M. Samiei, Fabrication of nanostructured Al/Cu/Mn metallic multilayer composites by accumulative roll bonding process and investigation of their mechanical properties, *Materials & Design*. 56 (2014) 680–684. doi:10.1016/j.matdes.2013.11.067.
- [188] H. Chang, M.Y. Zheng, C. Xu, G.D. Fan, H.G. Brokmeier, K. Wu, Microstructure and mechanical properties of the Mg/Al multilayer fabricated by accumulative roll bonding (ARB) at ambient temperature, *Materials Science and Engineering: A*. 543 (2012) 249–256. doi:10.1016/j.msea.2012.02.083.
- [189] K.X. Wei, W. Wei, Q.B. Du, J. Hu, Microstructure and tensile properties of Al–Mn alloy processed by accumulative roll bonding, *Materials Science and Engineering: A*. 525 (2009) 55–59. doi:10.1016/j.msea.2009.06.028.
- [190] H.W. Huang, Z.B. Wang, J. Lu, K. Lu, Fatigue behaviors of AISI 316L stainless steel with a gradient nanostructured surface layer, *Acta Materialia*. 87 (2015) 150–160. doi:10.1016/j.actamat.2014.12.057.
- [191] Y.S. Zhang, Z. Han, K. Wang, K. Lu, Friction and wear behaviors of nanocrystalline surface layer of pure copper, *Wear*. 260 (2006) 942–948. doi:10.1016/j.wear.2005.06.010.
- [192] A. Misra, J.P. Hirth, R.G. Hoagland, Length-scale-dependent deformation mechanisms in incoherent metallic multilayered composites, *Acta Materialia*. 53 (2005) 4817–4824. doi:10.1016/j.actamat.2005.06.025.
- [193] X. Wu, M. Yang, F. Yuan, G. Wu, Y. Wei, X. Huang, et al., Heterogeneous lamella structure unites ultrafine-grain strength with coarse-grain ductility, *Proceedings of the National Academy of Sciences*. (2015) 201517193. doi:10.1073/pnas.1517193112.
- [194] Y. Wei, Y. Li, L. Zhu, Y. Liu, X. Lei, G. Wang, et al., Evading the strength–ductility trade-off dilemma in steel through gradient hierarchical nanotwins, *Nat. Commun*. 5 (2014). doi:10.1038/ncomms4580.
- [195] H. Kou, J. Lu, Y. Li, High-Strength and High-Ductility Nanostructured and Amorphous Metallic Materials, *Advanced Materials*. 26 (2014) 5518–5524. doi:10.1002/adma.201401595.
- [196] D.K. Yang, P. Cizek, D. Fabijanic, J.T. Wang, P.D. Hodgson, Work hardening in ultrafine-grained titanium: Multilayering and grading, *Acta Mater*. 61 (2013) 2840–2852. doi:http://dx.doi.org/10.1016/j.actamat.2013.01.018.

- [197] B. Cai, X. Ma, J. Moering, H. Zhou, X. Yang, X. Zhu, Enhanced mechanical properties in Cu–Zn alloys with a gradient structure by surface mechanical attrition treatment at cryogenic temperature, *Materials Science and Engineering: A*. 626 (2015) 144–149. doi:10.1016/j.msea.2014.12.070.
- [198] X.L. Wu, P. Jiang, L. Chen, J.F. Zhang, F.P. Yuan, Y.T. Zhu, Synergetic Strengthening by Gradient Structure, *Mater. Res. Lett.* (2014) 1–7. doi:10.1080/21663831.2014.935821.
- [199] ASM International, J.R. Davis, ASM International, eds., *Properties and selection: nonferrous alloys and special-purpose materials*, [10. ed.], 6. print, ASM International, Materials Park, Ohio, 2000.
- [200] C.W. Schmidt, M. Ruppert, H.W. Höppel, F. Nachtrab, A. Dietrich, R. Hanke, et al., Design of Graded Materials by Particle Reinforcement During Accumulative Roll Bonding: Design of Graded Materials by Particle Reinforcement During ARB, *Advanced Engineering Materials*. 14 (2012) 1009–1017. doi:10.1002/adem.201200046.
- [201] H.P. Ng, T. Przybilla, C. Schmidt, R. Lapovok, D. Orlov, H.-W. Höppel, et al., Asymmetric accumulative roll bonding of aluminium–titanium composite sheets, *Materials Science and Engineering: A*. 576 (2013) 306–315. doi:10.1016/j.msea.2013.04.027.
- [202] F. Wu, Y.T. Zhu, J. Narayan, Macroscopic Twinning Strain in Nanocrystalline Cu, *Materials Research Letters*. 2 (2014) 63–69. doi:10.1080/21663831.2013.862874.
- [203] L. Lu, X. Chen, X. Huang, K. Lu, Revealing the Maximum Strength in Nanotwinned Copper, *Science*. 323 (2009) 607–610. doi:10.1126/science.1167641.
- [204] P. Gu, M. Dao, Y. Zhu, Strengthening at nanoscaled coherent twin boundary in f.c.c. metals, *Philos. Mag.* 94 (2014) 1249–1262. doi:10.1080/14786435.2014.885138.
- [205] L. Lu, R. Schwaiger, Z.W. Shan, M. Dao, K. Lu, S. Suresh, Nano-sized twins induce high rate sensitivity of flow stress in pure copper, *Acta Mater.* 53 (2005) 2169–2179. doi:http://dx.doi.org/10.1016/j.actamat.2005.01.031.
- [206] Y.F. Shen, L. Lu, Q.H. Lu, Z.H. Jin, K. Lu, Tensile properties of copper with nano-scale twins, *Scripta Mater.* 52 (2005) 989–994. doi:http://dx.doi.org/10.1016/j.scriptamat.2005.01.033.
- [207] Y.M. Wang, F. Sansoz, T. LaGrange, R.T. Ott, J. Marian, T.W. Barbee Jr, et al., Defective twin boundaries in nanotwinned metals, *Nat. Mater.* 12 (2013) 697–702.

doi:10.1038/nmat3646

<http://www.nature.com/nmat/journal/v12/n8/abs/nmat3646.html#supplementary-information>.

- [208] G.T. Gray Iii, Deformation twinning in Al-4.8 wt% Mg, *Acta Metallurgica*. 36 (1988) 1745–1754. doi:[http://dx.doi.org/10.1016/0001-6160\(88\)90242-8](http://dx.doi.org/10.1016/0001-6160(88)90242-8).
- [209] Y. Cao, Y.B. Wang, X.Z. Liao, M. Kawasaki, S.P. Ringer, T.G. Langdon, et al., Applied stress controls the production of nano-twins in coarse-grained metals, *Appl. Phys. Lett.* 101 (2012) 231903. doi:<http://dx.doi.org/10.1063/1.4769216>.
- [210] W.S. Zhao, N.R. Tao, J.Y. Guo, Q.H. Lu, K. Lu, High density nano-scale twins in Cu induced by dynamic plastic deformation, *Scripta Mater.* 53 (2005) 745–749. doi:<http://dx.doi.org/10.1016/j.scriptamat.2005.05.022>.
- [211] G.H. Xiao, N.R. Tao, K. Lu, Effects of strain, strain rate and temperature on deformation twinning in a Cu–Zn alloy, *Scripta Mater.* 59 (2008) 975–978. doi:<http://dx.doi.org/10.1016/j.scriptamat.2008.06.060>.
- [212] H. Van Swygenhoven, P.M. Derlet, A.G. Froseth, Stacking fault energies and slip in nanocrystalline metals, *Nat. Mater.* 3 (2004) 399–403. doi:10.1038/nmat1136.
- [213] Z.W. Wang, Y.B. Wang, X.Z. Liao, Y.H. Zhao, E.J. Lavernia, Y.T. Zhu, et al., Influence of stacking fault energy on deformation mechanism and dislocation storage capacity in ultrafine-grained materials, *Scripta Mater.* 60 (2009) 52–55. doi:<http://dx.doi.org/10.1016/j.scriptamat.2008.08.032>.
- [214] X.L. Wu, K.M. Youssef, C.C. Koch, S.N. Mathaudhu, L.J. Kecskés, Y.T. Zhu, Deformation twinning in a nanocrystalline hcp Mg alloy, *Scripta Materialia*. 64 (2011) 213–216. doi:10.1016/j.scriptamat.2010.10.024.
- [215] F. Wu, Y.T. Zhu, J. Narayan, Grain size effect on twin density in as-deposited nanocrystalline Cu film, *Philos. Mag.* 93 (2013) 4355–4363. doi:10.1080/14786435.2013.829251.
- [216] V.S. Boyko, R.Y. Kezerashvili, Twinning propensity in nanocrystalline face-centered cubic, body-centered cubic, and hexagonal close-packed metals, *J. Phys. Chem. Solids*. 75 (2014) 1119–1123. doi:<http://dx.doi.org/10.1016/j.jpcs.2014.05.012>.
- [217] D. Finkenstadt, D.D. Johnson, Solute/defect-mediated pathway for rapid nanoprecipitation in solid solutions: $\langle \text{span class="aps-inline-formula"} \rangle \langle \text{math xmlns="http://www.w3.org/1998/Math/MathML"} \rangle$

display="inline">γ surface analysis in fcc Al-Ag, Phys. Rev. B. 73 (2006) 024101.

- [218] Y.F. Wen, J. Sun, Generalized planar fault energies and mechanical twinning in gamma TiAl alloys, *Scripta Mater.* 68 (2013) 759–762. doi:<http://dx.doi.org/10.1016/j.scriptamat.2012.12.032>.
- [219] S. Kibey, J.B. Liu, D.D. Johnson, H. Sehitoglu, Generalized planar fault energies and twinning in Cu–Al alloys, *Applied Physics Letters*. 89 (2006) 191911. doi:10.1063/1.2387133.
- [220] T. Hebesberger, H.P. Stüwe, A. Vorhauer, F. Wetscher, R. Pippan, Structure of Cu deformed by high pressure torsion, *Acta Mater.* 53 (2005) 393–402. doi:<http://dx.doi.org/10.1016/j.actamat.2004.09.043>.
- [221] Y.H. Zhao, X.Z. Liao, Y.T. Zhu, Z. Horita, T.G. Langdon, Influence of stacking fault energy on nanostructure formation under high pressure torsion, *Mater. Sci. Eng., A*. 410–411 (2005) 188–193. doi:<http://dx.doi.org/10.1016/j.msea.2005.08.074>.
- [222] Y.B. Wang, X.Z. Liao, Y.H. Zhao, E.J. Lavernia, S.P. Ringer, Z. Horita, et al., The role of stacking faults and twin boundaries in grain refinement of a Cu–Zn alloy processed by high-pressure torsion, *Mater. Sci. Eng., A*. 527 (2010) 4959–4966. doi:<http://dx.doi.org/10.1016/j.msea.2010.04.036>.
- [223] C.X. Huang, W. Hu, G. Yang, Z.F. Zhang, S.D. Wu, Q.Y. Wang, et al., The effect of stacking fault energy on equilibrium grain size and tensile properties of nanostructured copper and copper–aluminum alloys processed by equal channel angular pressing, *Mater. Sci. Eng., A*. 556 (2012) 638–647. doi:<http://dx.doi.org/10.1016/j.msea.2012.07.041>.
- [224] Y.H. Zhao, Y.T. Zhu, X.Z. Liao, Z. Horita, T.G. Langdon, Influence of stacking fault energy on the minimum grain size achieved in severe plastic deformation, *Mater. Sci. Eng., A*. 463 (2007) 22–26. doi:<http://dx.doi.org/10.1016/j.msea.2006.08.119>.
- [225] L. Balogh, T. Ungár, Y. Zhao, Y.T. Zhu, Z. Horita, C. Xu, et al., Influence of stacking-fault energy on microstructural characteristics of ultrafine-grain copper and copper–zinc alloys, *Acta Mater.* 56 (2008) 809–820. doi:<http://dx.doi.org/10.1016/j.actamat.2007.10.053>.
- [226] J.Y. Huang, Y.T. Zhu, H. Jiang, T.C. Lowe, Microstructures and dislocation configurations in nanostructured Cu processed by repetitive corrugation and straightening, *Acta Materialia*. 49 (2001) 1497–1505. doi:10.1016/S1359-6454(01)00069-6.

- [227] X.L. Wu, Y.T. Zhu, E. Ma, Predictions for partial-dislocation-mediated processes in nanocrystalline Ni by generalized planar fault energy curves: An experimental evaluation, *Appl. Phys. Lett.* 88 (2006) 121905. doi:doi:http://dx.doi.org/10.1063/1.2186968.
- [228] Y.T. Zhu, X.L. Wu, X.Z. Liao, J. Narayan, S.N. Mathaudhu, L.J. Kecskés, Twinning partial multiplication at grain boundary in nanocrystalline fcc metals, *Appl. Phys. Lett.* 95 (2009) 031909. doi:doi:http://dx.doi.org/10.1063/1.3187539.
- [229] S. Kibey, J.B. Liu, D.D. Johnson, H. Sehitoglu, Energy pathways and directionality in deformation twinning, *Appl. Phys. Lett.* 91 (2007) 181916. doi:doi:http://dx.doi.org/10.1063/1.2800806.
- [230] Gallaghe. Pc, Influence of alloying, temperature, and related effects on stacking fault energy, *Metall. Trans.* 1 (1970) 2429.
- [231] ASM International, J.R. Davis, ASM International, eds., *Properties and selection: nonferrous alloys and special-purpose materials*, [10. ed.], 6. print, ASM International, Materials Park, Ohio, 2000.
- [232] N. Bernstein, E.B. Tadmor, Tight-binding calculations of stacking energies and twinnability in fcc metals, *Phys. Rev. B.* 69 (2004) 094116.
- [233] L. Wei, L. Song, H. Qing-Miao, K. Se Kyun, J. Börje, V. Levente, Generalized stacking fault energies of alloys, *J. Phys.: Condens. Matter.* 26 (2014) 265005.
- [234] Z.H. Jin, S.T. Dunham, H. Gleiter, H. Hahn, P. Gumbsch, A universal scaling of planar fault energy barriers in face-centered cubic metals, *Scripta Mater.* 64 (2011) 605–608. doi:http://dx.doi.org/10.1016/j.scriptamat.2010.11.033.
- [235] H. Suzuki, Segregation of Solute Atoms to Stacking Faults, *Journal of the Physical Society of Japan.* 17 (1962) 322–325. doi:10.1143/JPSJ.17.322.
- [236] S. Kibey, L.L. Wang, J.B. Liu, H.T. Johnson, H. Sehitoglu, D.D. Johnson, Quantitative prediction of twinning stress in fcc alloys: Application to Cu-Al, *Physical Review B.* 79 (2009). doi:10.1103/PhysRevB.79.214202.
- [237] L.E. Murr, *Interfacial phenomena in metals and alloys*, Addison-Wesley Pub. Co., Advanced Book Program, 1975.
- [238] M.L. Rudee, R.A. Huggins, Some aspects of solute segregation to stacking faults, *Philos. Mag.* 11 (1965) 539–547. doi:10.1080/14786436508224240.

- [239] A. Ookawa, On the Mechanism of Deformation Twin in fcc Crystal, *J. Phys. Soc. Jpn.* 12 (1957) 825–825. doi:10.1143/JPSJ.12.825.
- [240] J.A. Venables, Deformation twinning in face-centred cubic metals, *Philos. Mag.* 6 (1961) 379–396. doi:10.1080/14786436108235892.
- [241] Y.J. Xu, K. Du, C.Y. Cui, H.Q. Ye, Deformation twinning with zero macroscopic strain in a coarse-grained Ni–Co-based superalloy, *Scripta Mater.* 77 (2014) 71–74. doi:http://dx.doi.org/10.1016/j.scriptamat.2014.01.030.
- [242] J. Wang, O. Anderoglu, J.P. Hirth, A. Misra, X. Zhang, Dislocation structures of $\Sigma 3$ {112} twin boundaries in face centered cubic metals, *Appl. Phys. Lett.* 95 (2009) 021908. doi:http://dx.doi.org/10.1063/1.3176979.
- [243] P.C.J. Gallagher, The influence of alloying, temperature, and related effects on the stacking fault energy, *Metallurgical Transactions.* 1 (1970) 2429–2461. doi:10.1007/BF03038370.
- [244] X.L. Ma, W.Z. Xu, H. Zhou, J.A. Moering, J. Narayan, Y.T. Zhu, Alloying effect on grain-size dependent deformation twinning in nanocrystalline Cu–Zn alloys, *Philosophical Magazine.* 95 (2015) 301–310. doi:10.1080/14786435.2014.1000418.
- [245] Y. Liu, J. Jian, Y. Chen, H. Wang, X. Zhang, Plasticity and ultra-low stress induced twin boundary migration in nanotwinned Cu by in situ nanoindentation studies, *Appl. Phys. Lett.* 104 (2014) 231910. doi:doi:http://dx.doi.org/10.1063/1.4882242.
- [246] G. Sundararajan, Y. Tirupataiah, The hardness-flow stress correlation in metallic materials, *Bull. Mater. Sci.* 17 (1994) 747–770. doi:10.1007/BF02757555.
- [247] X.L. Lu, Q.H. Lu, Y. Li, L. Lu, Gradient Confinement Induced Uniform Tensile Ductility in Metallic Glass, *Sci. Rep.* 3 (2013). doi:10.1038/srep03319
http://www.nature.com/srep/2013/131125/srep03319/abs/srep03319.html#supplementary-information.
- [248] A. Jérusalem, W. Dickson, M.J. Pérez-Martín, M. Dao, J. Lu, F. Gálvez, Grain size gradient length scale in ballistic properties optimization of functionally graded nanocrystalline steel plates, *Scripta Mater.* 69 (2013) 773–776. doi:http://dx.doi.org/10.1016/j.scriptamat.2013.08.025.
- [249] A.-Y. Chen, D.-F. Li, J.-B. Zhang, H.-W. Song, J. Lu, Make nanostructured metal exceptionally tough by introducing non-localized fracture behaviors, *Scripta Mater.* 59 (2008) 579–582. doi:http://dx.doi.org/10.1016/j.scriptamat.2008.04.048.

- [250] K. Barmak, A. Gungor, C. Cabral, J.M.E. Harper, Annealing behavior of Cu and dilute Cu-alloy films: Precipitation, grain growth, and resistivity, *J. Appl. Phys.* 94 (2003) 1605–1616. doi:<http://dx.doi.org/10.1063/1.1589593>.
- [251] X.H. An, S.D. Wu, Z.F. Zhang, R.B. Figueiredo, N. Gao, T.G. Langdon, Evolution of microstructural homogeneity in copper processed by high-pressure torsion, *Scripta Mater.* 63 (2010) 560–563. doi:<http://dx.doi.org/10.1016/j.scriptamat.2010.05.030>.
- [252] S.L. Semiatin, H.R. Piehler, Deformation of sandwich sheet materials in uniaxial tension, *MTA.* 10 (1979) 85–96. doi:10.1007/BF02686411.
- [253] D. Jia, Y.M. Wang, K.T. Ramesh, E. Ma, Y.T. Zhu, R.Z. Valiev, Deformation behavior and plastic instabilities of ultrafine-grained titanium, *Appl. Phys. Lett.* 79 (2001) 611–613. doi:<http://dx.doi.org/10.1063/1.1384000>.
- [254] Y.M. Wang, J.Y. Huang, T. Jiao, Y.T. Zhu, A.V. Hamza, Abnormal strain hardening in nanostructured titanium at high strain rates and large strains, *J. Mater. Sci.* 42 (2007) 1751–1756. doi:10.1007/s10853-006-0822-0.
- [255] L. Jianjun, A. K. Soh, Enhanced ductility of surface nano-crystallized materials by modulating grain size gradient, *Model. Simul. Mater. Sci. Eng.* 20 (2012) 085002.
- [256] S. Zheng, I.J. Beyerlein, J.S. Carpenter, K. Kang, J. Wang, W. Han, et al., High-strength and thermally stable bulk nanolayered composites due to twin-induced interfaces, *Nature Communications.* 4 (2013) 1696. doi:10.1038/ncomms2651.
- [257] J. Lu, H.L. Chan, A.Y. Chen, H.N. Kou, Mechanics of High Strength and High Ductility Materials, *Procedia Eng.* 10 (2011) 2202–2207. doi:<http://dx.doi.org/10.1016/j.proeng.2011.04.364>.
- [258] S.-B. Lee, J.E. LeDonne, S.C.V. Lim, I.J. Beyerlein, A.D. Rollett, The heterophase interface character distribution of physical vapor-deposited and accumulative roll-bonded Cu–Nb multilayer composites, *Acta Materialia.* 60 (2012) 1747–1761. doi:10.1016/j.actamat.2011.12.007.
- [259] X.C. Liu, H.W. Zhang, K. Lu, Formation of nano-laminated structure in nickel by means of surface mechanical grinding treatment, *Acta Materialia.* 96 (2015) 24–36. doi:10.1016/j.actamat.2015.06.014.
- [260] Y. Mishin, M. Asta, J. Li, Atomistic modeling of interfaces and their impact on microstructure and properties, *Acta Materialia.* 58 (2010) 1117–1151. doi:10.1016/j.actamat.2009.10.049.

- [261] J. Li, S. Chen, X. Wu, A.K. Soh, A physical model revealing strong strain hardening in nano-grained metals induced by grain size gradient structure, *Materials Science and Engineering: A*. 620 (2015) 16–21. doi:10.1016/j.msea.2014.09.117.
- [262] H.F. Tan, B. Zhang, X.M. Luo, X.D. Sun, G.P. Zhang, Strain rate dependent tensile plasticity of ultrafine-grained Cu/Ni laminated composites, *Materials Science and Engineering: A*. 609 (2014) 318–322. doi:10.1016/j.msea.2014.04.111.
- [263] Z. Zeng, X. Li, D. Xu, L. Lu, H. Gao, T. Zhu, Gradient plasticity in gradient nano-grained metals, *Extreme Mechanics Letters*. (2015). doi:10.1016/j.eml.2015.12.005.
- [264] M.F. Ashby, The deformation of plastically non-homogeneous materials, *Philos. Mag.* 21 (1970) 399–424. doi:10.1080/14786437008238426.
- [265] N.A. Fleck, G.M. Muller, M.F. Ashby, J.W. Hutchinson, Strain gradient plasticity: Theory and experiment, *Acta Metallurgica et Materialia*. 42 (1994) 475–487. doi:10.1016/0956-7151(94)90502-9.
- [266] W.D. Nix, H. Gao, Indentation size effects in crystalline materials: A law for strain gradient plasticity, *Journal of the Mechanics and Physics of Solids*. 46 (1998) 411–425. doi:10.1016/S0022-5096(97)00086-0.
- [267] K. Tanaka, K. Shibata, K. Kurumatani, S. Ikeuchi, S. Kikuchi, R. Kondo, et al., Formation mechanism of micro/nano-structures through competitive reactions in Mg/Cu super-laminate composites during initial hydrogenation, *Journal of Alloys and Compounds*. 645 (2015) S72–S75. doi:10.1016/j.jallcom.2015.01.196.
- [268] J. Jiang, T.B. Britton, A.J. Wilkinson, Evolution of dislocation density distributions in copper during tensile deformation, *Acta Materialia*. 61 (2013) 7227–7239. doi:10.1016/j.actamat.2013.08.027.
- [269] P.D. Littlewood, A.J. Wilkinson, Geometrically necessary dislocation density distributions in cyclically deformed Ti–6Al–4V, *Acta Materialia*. 60 (2012) 5516–5525. doi:10.1016/j.actamat.2012.07.003.
- [270] M. Calcagnotto, D. Ponge, E. Demir, D. Raabe, Orientation gradients and geometrically necessary dislocations in ultrafine grained dual-phase steels studied by 2D and 3D EBSD, *Materials Science and Engineering: A*. 527 (2010) 2738–2746. doi:10.1016/j.msea.2010.01.004.
- [271] J. Jiang, T.B. Britton, A.J. Wilkinson, Measurement of geometrically necessary dislocation density with high resolution electron backscatter diffraction: Effects of

- detector binning and step size, *Ultramicroscopy*. 125 (2013) 1–9.
doi:10.1016/j.ultramic.2012.11.003.
- [272] I. Brough, P.S. Bate, F.J. Humphreys, Optimising the angular resolution of EBSD, *Materials Science and Technology*. 22 (2006) 1279–1286.
doi:10.1179/174328406X130902.
- [273] T. Leffers, R.K. Ray, The brass-type texture and its deviation from the copper-type texture, *Progress in Materials Science*. 54 (2009) 351–396.
doi:10.1016/j.pmatsci.2008.09.002.
- [274] J. Hirsch, K. Lücke, Overview no. 76, *Acta Metallurgica*. 36 (1988) 2863–2882.
doi:10.1016/0001-6160(88)90172-1.
- [275] C. Donadille, R. Valle, P. Dervin, R. Penelle, Development of texture and microstructure during cold-rolling and annealing of F.C.C. alloys: Example of an austenitic stainless steel, *Acta Metallurgica*. 37 (1989) 1547–1571. doi:10.1016/0001-6160(89)90123-5.
- [276] H.-W. Kim, S.-B. Kang, N. Tsuji, Y. Minamino, Elongation increase in ultra-fine grained Al–Fe–Si alloy sheets, *Acta Materialia*. 53 (2005) 1737–1749.
doi:10.1016/j.actamat.2004.12.022.
- [277] A.J. Wilkinson, A new method for determining small misorientations from electron back scatter diffraction patterns, *Scripta Materialia*. 44 (2001) 2379–2385.
doi:10.1016/S1359-6462(01)00943-5.
- [278] A.J. Wilkinson, D. Randman, Determination of elastic strain fields and geometrically necessary dislocation distributions near nanoindentations using electron back scatter diffraction, *Philosophical Magazine*. 90 (2010) 1159–1177.
doi:10.1080/14786430903304145.
- [279] J.D. Eshelby, F.C. Frank, F.R.N. Nabarro, XLI. The equilibrium of linear arrays of dislocations., *The London, Edinburgh, and Dublin Philosophical Magazine and Journal of Science*. 42 (1951) 351–364. doi:10.1080/14786445108561060.
- [280] N.A. Mara, I.J. Beyerlein, Review: effect of bimetal interface structure on the mechanical behavior of Cu–Nb fcc–bcc nanolayered composites, *Journal of Materials Science*. 49 (2014) 6497–6516. doi:10.1007/s10853-014-8342-9.
- [281] W.Z. Han, A. Misra, N.A. Mara, T.C. Germann, J.K. Baldwin, T. Shimada, et al., Role of interfaces in shock-induced plasticity in Cu/Nb nanolaminates, *Philosophical Magazine*. 91 (2011) 4172–4185. doi:10.1080/14786435.2011.603706.

- [282] X. Feaugas, On the origin of the tensile flow stress in the stainless steel AISI 316L at 300 K: back stress and effective stress, *Acta Materialia*. 47 (1999) 3617–3632. doi:10.1016/S1359-6454(99)00222-0.
- [283] M. Yang, Y. Pan, F. Yuan, Y. Zhu, X. Wu, Back stress strengthening and strain hardening in gradient structure, *Materials Research Letters*. (2016) 1–7. doi:10.1080/21663831.2016.1153004.
- [284] O. Bouaziz, S. Allain, C. Scott, Effect of grain and twin boundaries on the hardening mechanisms of twinning-induced plasticity steels, *Scripta Materialia*. 58 (2008) 484–487. doi:10.1016/j.scriptamat.2007.10.050.
- [285] A. Misra, R.G. Hoagland, Plastic flow stability of metallic nanolaminate composites, *Journal of Materials Science*. 42 (2007) 1765–1771. doi:10.1007/s10853-006-0895-9.
- [286] T.. Nieh, T.. Barbee, J. Wadsworth, Tensile properties of a free-standing Cu/Zr nanolaminate (or compositionally-modulated thin film), *Scripta Materialia*. 41 (1999) 929–935. doi:10.1016/S1359-6462(99)00240-7.
- [287] H.S. Shahabi, M. Eizadjou, H.D. Manesh, Evolution of mechanical properties in SPD processed Cu/Nb nano-layered composites, *Materials Science and Engineering: A*. 527 (2010) 5790–5795. doi:10.1016/j.msea.2010.05.087.

APPENDICES

A1. Matlab codes to determine uniform elongation

```
function [ unielong ] = unielong( strain, stress, modulus )
%calculations of tensile strength, uniform elongation and 2% yield strength
%inputs are corrected tensile curve and the known modulus for the material
unifin=max(find(stress==max(stress), length(stress)));
unielong(1)=max(stress);
unielong(2)=strain(unifin)-max(stress)/modulus;
plot(strain, stress)

%calculate yield strength by interpolation
strainmax=max(stress)/modulus;
for i=1:1000
    inter(i)=strainmax/1000*i+0.002;
    interstress(i)=strainmax/1000*i*modulus;
end
newstress=interp1([0, average(strain,10)], [0, average(stress,10)], inter);
flag=1; i=1;
while flag>0
    flag=newstress(i)-interstress(i);
    i=i+1;
end
unielong(3)=newstress(i);
end
```

A2. Matlab codes to determine local misorientation

```
function [ angle] = localmis( x, y, euler )
% position is a 2 elements vector, standing for the position of interest
% euler is the orientation dataset connected to position
% return is the local misorientation by averaging the misorientated
% angles of surrounding 24 grids.

phi_0=posi_orien([x, y], euler);
phi(1, :)=posi_orien([x-1, y-1], euler);
phi(2, :)=posi_orien([x-1, y], euler);
phi(3, :)=posi_orien([x-1, y+1], euler);
phi(4, :)=posi_orien([x, y+1], euler);
phi(5, :)=posi_orien([x+1, y+1], euler);
phi(6, :)=posi_orien([x+1, y], euler);
phi(7, :)=posi_orien([x+1, y-1], euler);
phi(8, :)=posi_orien([x, y-1], euler);

phi(9, :)=posi_orien([x-2, y-2], euler);
phi(10, :)=posi_orien([x-2, y-1], euler);
phi(11, :)=posi_orien([x-2, y], euler);
phi(12, :)=posi_orien([x-2, y+1], euler);
phi(13, :)=posi_orien([x-2, y+2], euler);
phi(14, :)=posi_orien([x-1, y-2], euler);
phi(15, :)=posi_orien([x-1, y+2], euler);
phi(16, :)=posi_orien([x, y-2], euler);
phi(17, :)=posi_orien([x, y+2], euler);
```

```

phi(18,:)=posi_orien([x+1,y-2],euler);
phi(19,:)=posi_orien([x+1,y+2],euler);
phi(20,:)=posi_orien([x+2,y-2],euler);
phi(21,:)=posi_orien([x+2,y-1],euler);
phi(22,:)=posi_orien([x+2,y],euler);
phi(23,:)=posi_orien([x+2,y+1],euler);
phi(24,:)=posi_orien([x+2,y+2],euler);

```

```

for i=1:8
    if sum(phi(i,:)==0)==3;
        misangle(i)=20;
    else
        misangle(i)=misor(phi_0,phi(i,:));
    end
end
% angle=misangle(1);
if sum(misangle>3)>0;
angle=0;
else angle=mean(misangle);
end
end

```

```

function [ phi ] = posi_orien( posi, euler )
% position is a 2 elements vector, standing for the position of interest
% euler is the orientation dataset connected to position
% return is the specific orientation angle data for this coordinates.

```

```

phi1=euler(posi(1),posi(2),1);
phi2=euler(posi(1),posi(2),2);
phi3=euler(posi(1),posi(2),3);
phi=[phi1,phi2,phi3];
end

```

```

function [ angle ] = misor( a,b )
%MISOR Summary of this function goes here
% Detailed explanation goes here
temp=trace(orientation(a)*inv(orientation(b)));
angle=acos((temp-1)/2)*180/pi;
end

```

```

function [ orient ] = orientation( a )
%ORIENTATION1 Summary of this function goes here
% Detailed explanation goes here
a=a/180*pi;
orient=[cos(a(1))*cos(a(3))-
sin(a(1))*sin(a(3))*cos(a(2)),sin(a(1))*cos(a(3))+cos(a(1))*sin(a(3))*cos(a
(2)),sin(a(3))*sin(a(2));-cos(a(1))*sin(a(3))-
sin(a(1))*cos(a(3))*cos(a(2)),-
sin(a(1))*sin(a(3))+cos(a(1))*cos(a(3))*cos(a(2)),cos(a(3))*sin(a(2));sin(a
(1))*sin(a(2)),cos(a(1))*sin(a(2)),cos(a(2))];
end

```